

August 2017

# Design for Safety: Characterization of Structural Impact on Lithium-ion Batteries

Mehdi Gilaki

*University of Wisconsin-Milwaukee*

Follow this and additional works at: <https://dc.uwm.edu/etd>



Part of the [Mechanical Engineering Commons](#)

---

## Recommended Citation

Gilaki, Mehdi, "Design for Safety: Characterization of Structural Impact on Lithium-ion Batteries" (2017). *Theses and Dissertations*. 1623.

<https://dc.uwm.edu/etd/1623>

This Dissertation is brought to you for free and open access by UWM Digital Commons. It has been accepted for inclusion in Theses and Dissertations by an authorized administrator of UWM Digital Commons. For more information, please contact [open-access@uwm.edu](mailto:open-access@uwm.edu).



# DESIGN FOR SAFETY: CHARACTERIZATION OF STRUCTURAL IMPACT ON LITHIUM-ION BATTERIES

by

Mehdi Gilaki

A Dissertation Submitted in  
Partial Fulfillment of the  
Requirements for the Degree of

DOCTOR OF PHILOSOPHY  
IN ENGINEERING

at

The University of Wisconsin–Milwaukee

August 2017

## ABSTRACT

# DESIGN FOR SAFETY: CHARACTERIZATION OF STRUCTURAL IMPACT ON LITHIUM-ION BATTERIES

by

Mehdi Gilaki

The University of Wisconsin–Milwaukee, 2017  
Under the Supervision of Professor Ilya Avdeev

The goal of this research is to develop a framework for design for safety of battery modules used in EV/HEV applications. Such a framework can enhance the crash safety of lithium-ion batteries by investigating prevailing failure mechanisms such as thermal runaway. The problem involves different scales from module level to laminate level. The multi-scale nature of the problem makes the analysis computationally complex and expensive. Furthermore, because of the risk of explosion, a battery testing apparatus needs special safety provisions making it difficult to test charged and ready-to-use battery cells. In this study, we have numerically investigated feasibility of using commercial explicit finite element code LS-DYNA for accurate modeling of impact on one cell so it can be used for an entire battery module. A jellyroll, the main component of a cylindrical cell, is a layered spiral structure which consists of thin layers of anode, cathode and separator. Because modeling hundreds of individual layers would be computationally expensive for a multi-cell model, two homogenization methods have been developed for the jellyroll in the lateral direction. Various types of experiments have been conducted on jellyroll layers to characterize their mechanical properties under dry and saturated conditions as well as their strain-rate dependence. For the cell level impact tests, cells without electrolyte have been used to eliminate the risk of fire. Two types of impact tests have been conducted on cylindrical cells using a drop cart in a custom-built drop test apparatus: lateral impact between flat plate and rod impact based on the UN DOT 38.3 requirements. Quasi-static indentation tests using a rigid rod was also performed on

batteries with horizontal and vertical terminals orientations to characterize their behavior under steady loads. Mechanical deformations of the cells were studied experimentally using computed tomography scans and optical microscopy. Two homogeneous and heterogeneous finite element models were developed in LS-DYNA to simulate impact and indentation experiments. Simulations were validated by experimental results. A multi-scale framework was also proposed to simulate impact on PM12-JCI battery modules. The multi-scale process involved an initial impact simulation on battery module containing twelve homogeneous 6P-JCI cells and a subsequent simulation on a heterogeneous jellyroll model. The proposed multi-scale process can be developed further to simulate impacts on an entire battery pack.

© Copyright by Mehdi Gilaki, 2017  
All Rights Reserved

Dedicated to my mother  
who has been a constant source of love, motivation, inspiration and support  
throughout my life.

# TABLE OF CONTENTS

<b>1</b>	<b>Introduction</b>	<b>1</b>
1.1	Motivation . . . . .	1
1.1.1	Multiscale Nature of the problem . . . . .	4
1.1.2	Multiphysics Nature of the problem . . . . .	4
1.1.3	Prohibitive Cost of Experiments . . . . .	5
1.1.4	Computational Complexities . . . . .	6
1.2	Background . . . . .	6
1.3	Approach . . . . .	10
<b>2</b>	<b>Cell Level: Jellyroll Characterization/Homogenization</b>	<b>16</b>
2.1	Jellyroll Homogenization . . . . .	16
2.1.1	Direct Homogenization Using Flattened Jellyroll . . . . .	16
2.1.2	Indirect Homogenization Using Virtual Work Principle . . . . .	19
2.1.3	Homogenization of Wet Samples . . . . .	25
2.2	Characterization of Individual Jellyroll Layers . . . . .	26
2.2.1	Characterization of Anode and Cathode Layers . . . . .	27
2.2.2	Characterization of Separator's Mechanical Response . . . . .	27
2.3	Jellyroll Characterization Using LVDT Deflection Sensor . . . . .	32
2.3.1	Effects of Clamps and Sample Thickness . . . . .	34
2.3.2	Jellyroll Wet/Dry Compression Tests . . . . .	35
2.3.3	Strain-Rate Dependence . . . . .	36
2.3.4	Characterization of Individual Jellyroll layers (Wet/Dry) . . . . .	39
2.4	Study of Separator Pore Size under Compression . . . . .	45
<b>3</b>	<b>Cell Level: Experiments</b>	<b>49</b>
3.1	Drop Tests . . . . .	49
3.1.1	Experimental Procedure and Setup . . . . .	49
3.1.2	Lateral Impact Between Two Flat Plates . . . . .	51
3.1.3	Lateral Impact Using a Rigid Bar . . . . .	53
3.2	Quasi-Static Compression Experiments . . . . .	57
3.3	Post Processing of Crushed Cells . . . . .	64
3.3.1	Computed Tomography Scanning of Battery Cells . . . . .	64
3.3.2	Microscopy of Crushed Jellyrolls . . . . .	65
<b>4</b>	<b>Cell Level: Explicit Finite Element Analysis</b>	<b>71</b>
4.1	Lateral Impact between Two Flat Plates . . . . .	71
4.1.1	Homogeneous Jellyroll Model . . . . .	71
4.1.2	Heterogeneous Jellyroll Model . . . . .	78
4.1.3	Updated Simulations using LVDT Characterizations . . . . .	81
4.2	Rod Impact Simulations . . . . .	86
4.3	Rod Indentation Simulations . . . . .	90

<b>5</b>	<b>Module Level: Multi-Scale Finite Element Simulation</b>	<b>93</b>
5.1	Finite Element Model of PM12 Module . . . . .	93
5.2	Multiscale Simulation Scheme . . . . .	95
<b>6</b>	<b>Conclusions</b>	<b>101</b>
6.1	Jellyroll Characterization/Homogenization . . . . .	101
6.2	Cell Level: Impact and Indentation Experiments . . . . .	103
6.3	Module Level: Multi-Scale Simulation . . . . .	105
6.4	Future Work . . . . .	106
	<b>Bibliography</b>	<b>107</b>
	<b>Curriculum Vitae</b>	<b>121</b>

# LIST OF FIGURES

1.1	A Chevrolet Volt car before and after fire incident. . . . .	2
1.2	Third Tesla Model S catches fire after hitting road debris. . . . .	2
1.3	An exploded Samsung Galaxy Note7 smartphone (Credit:Crushader/reddit). . . . .	3
1.4	Extremely small battery clearances for Samsung Galaxy Note7. . . . .	3
1.5	Various levels in safety analysis of lithium-ion batteries: (a) pack, (b) module, (c) cell and (d) laminate levels (scales in $m$ ). . . . .	5
1.6	Battery pack design aspects. . . . .	12
1.7	Multiscale simulation framework. . . . .	13
1.8	(a) 6P cylindrical cell and (b) PM12 power module made by Johnson Controls Inc. (Source: johnsoncontrols, 2015). . . . .	13
1.9	Cylindrical cell components: (a) casing, (b) jellyroll and inner tube, (c) spacer. . . . .	14
1.10	Two impact modes: (1) axial direction and (2) lateral direction. . . . .	14
2.1	Jellyroll layers: coated copper, coated aluminum and separator layers. . . . .	17
2.2	(a) A jellyroll sample with the metal core and (b) a jellyroll after being cut in a radial direction. . . . .	17
2.3	Flattened jellyroll sample under uniaxial compression. . . . .	18
2.4	Load-displacement of flattened jellyroll under compression ( $n = 3$ , relative $SD = 1.2\%$ ). . . . .	18
2.5	Stress-strain curves for flattened jellyroll samples. . . . .	19
2.6	Schematics of crushed jellyroll; force and displacement. . . . .	21
2.7	Equivalent cross section for homogenized stress-strain calculations. . . . .	21
2.8	Dimensions of crushed jellyroll. . . . .	22
2.9	Load-displacement relation and its third order interpolation. . . . .	23
2.10	Stress-strain curves found from the two homogenization methods. . . . .	24
2.11	(a) Jellyroll samples being soaked in electrolyte, (b) Wet jellyroll sample under compression, (c) Load-displacement curve for wet jellyroll samples under compression ( $n = 3$ , relative $SD = 4.5\%$ ) and (d) Stress-strain curve comparison for dry/wet jellyroll samples. . . . .	26
2.12	(a) Coated aluminum layers, (b) Coated copper layers, (c) Compression test of coated aluminum sample, (d) Compression test of coated copper samples, (e) Measured load- displacement curves and (f) Calculated stress-strain curves for aluminum and copper layers. . . . .	28
2.13	(a) Stack of 224 Separator layers, (b) Sample before being compressed, (c) Load-displacement curves for separator samples and (d) Stress-strain relation comparison for individual jellyroll layers. . . . .	30
2.14	Scanning electron micrographs (SEM) of separator layers: (a) Surface SEM before compression, (b) Surface SEM after compression, (c) Cross-sectional SEM before compression and (d) Cross-sectional SEM after compression. . . . .	31
2.15	(a) Instron LVDT deflection sensor, model 2601-043 and (b) LVDT sensor installed on an Instron 5985 testing machine. . . . .	33



2.16	(a) Deflection comparison for crosshead and LVDT sensors and (b) Force caused by LVDT deflection. . . . .	34
2.17	(a) Stack of 50 layers of coated copper layers taped on a steel plate and (b) Stack of 100 coated copper layers clamped on both ends. . . . .	35
2.18	(a) A stack of coated copper layers being tested and (b) Stress-strain curves for coated copper samples with various number of layers. . . . .	35
2.19	(a) The DMC solvent used for jellyroll saturation and (b) Jellyroll samples being soaked in the solvent. . . . .	37
2.20	(a) A jellyroll sample being tested under compression and (b) Crushed jellyroll sample. . . . .	37
2.21	Stress-strain curves for flattened jellyroll samples under dry and saturated conditions. . . . .	38
2.22	(a) A jellyroll sample being tested under compression and (b) Stress-strain curves for jellyroll compression tests at various displacement rates. . . . .	39
2.23	Stacks of coated aluminum (top), coated copper (middle) and separator layers (bottom) clamped at both ends. . . . .	40
2.24	(a) A stack of 50 coated aluminum layers being tested under compression and (b) Deformed coated aluminum sample. . . . .	41
2.25	Stress-strain curves for coated aluminum samples under dry and saturated conditions. . . . .	41
2.26	(a) A stack of 50 coated copper layers being tested under compression and (b) Deformed coated copper sample. . . . .	42
2.27	Stress-strain curves for coated copper samples under dry and saturated conditions. . . . .	42
2.28	(a) A stack of 100 separator layers being tested under compression and (b) Deformed separator sample. . . . .	43
2.29	Stress-strain curves for separator samples under dry and saturated conditions. . . . .	44
2.30	Stress-strain curves for jellyroll components under dry and saturated conditions. . . . .	44
2.31	(a) Stack of 100 separator layers before compression and (b) Compression test of separator sample. . . . .	45
2.32	Stress-strain curve found from compression test of separator samples. . . . .	46
2.33	SEM images of separator layers: (a) Separator layer before compression, (b)-(e) Separator after compression tests with a crush load of 15 <i>kN</i> , 30 <i>kN</i> , 45 <i>kN</i> and 56 <i>kN</i> , respectively. . . . .	47
2.34	Variation of separator pore size with compressive load magnitude. . . . .	48
3.1	Custom-designed drop test apparatus: (a) CAD model and (b) actual drop test. . . . .	50
3.2	Lateral impact test (high-speed camera footage). . . . .	52
3.3	Cylindrical cell before/and after impact, 11.34 <i>kg</i> drop weight, horizontal orientation. . . . .	52
3.4	Cylindrical cell before/and after impact, 11.34 <i>kg</i> drop weight, vertical orientation. . . . .	53
3.5	Steel rod placed across the center of a cell based on UN DOT 38.3 standard. . . . .	54
3.6	(a) A Vibra-Metrics 1018 sensor (Credit: <a href="http://mistrasgroup.com">mistrasgroup.com</a> ), (b) Accelerometers installed on the drop cart. . . . .	54

3.7	Deformed cells after impact by a rigid bar. . . . .	55
3.8	A deformed cell after impact by a rigid bar. . . . .	56
3.9	Recorded acceleration data for sample A. . . . .	56
3.10	Sample D, quasi-static compression test by a steel rod. . . . .	58
3.11	Resistance measurement for sample D using a digital multimeter. . . . .	58
3.12	Schematic of the circuit used for steady compression tests with live resistance measurements. . . . .	60
3.13	An Instron 5985 universal testing machine and a Hewlett Packard 34970A data acquisition system being used for steady compression tests. . . . .	60
3.14	Cylindrical cell with horizontal and vertical terminal orientations being compressed using a steel rod. . . . .	61
3.15	(a) Recorded load-displacement curves for steady compression tests and (b) Recorded voltage change over the 1 $M\Omega$ resistor. . . . .	62
3.16	Load and voltage changes for steady indentation tests. . . . .	63
3.17	CT scan of a crushed cell after steady compression test (sample D) showing highly distorted layers. . . . .	65
3.18	CT scan of a crushed cell after steady compression test (sample D) showing a crack in an electrode near the aluminum core. . . . .	66
3.19	CT scan of a crushed cell after mechanical collapse showing cracks in the jellyroll and the aluminum core. . . . .	67
3.20	A crushed cell before cutting the middle section for microscopy of jellyroll layers. . . . .	67
3.21	Deformed jellyrolls after resin casting. . . . .	68
3.22	(a) Resin molded sample after being cut at the highest deformed cross section and (b) Polished cross section (1200 grit size). . . . .	68
3.23	Microscopic images of a deformed jellyroll (6.5x magnification) (a) Highly distorted layers and (b) Layers/separator failure near the casing. . . . .	69
3.24	Separator failure near the casing (200x magnification). . . . .	70
3.25	Copper layer failure adjacent to the aluminum core (100x magnification). . .	70
4.1	Main components of a cell's finite element model: (a) case, (b) spacer, (c) homogenized jellyroll and (d) inner tube. . . . .	72
4.2	Cross section of a cell's finite element model: (1) jellyroll, (2) aluminum core, (3) case and (4) spacer. . . . .	72
4.3	Cell impact configurations: (a) vertical and (b) horizontal. . . . .	73
4.4	Deformation comparison locations (horizontal orientation, 11.34 $kg$ weight)..	74
4.5	Impact load for various load cases and cell orientations. . . . .	75
4.6	Impact velocity for various load cases and cell orientations. . . . .	76
4.7	Comparison of the cell's deformed shape after impact; CT-scan vs. finite element results (11.34 $kg$ drop mass, horizontal orientation). . . . .	77
4.8	Jellyroll and inner tube's Von-Mises stress for the cell with horizontal orientation of terminals (11.34 $kg$ drop weight). . . . .	78
4.9	(a) Finite element model of jellyroll layers, (b) Comparison of homogeneous and heterogeneous jellyroll models and (c) Comparison of homogeneous and heterogeneous cell models. . . . .	80

4.10	(a) Jellyroll's deformed shape found from the homogeneous model, (b) deformed shape for heterogeneous model, (c) CT-scan of the crushed jellyroll, (d) Velocity change during impact and (e) Impact load for homogeneous and heterogeneous models. . . . .	82
4.11	Strain values of separator layers under maximum impact load and after unloading. . . . .	83
4.12	Jellyroll's Von-Mises stress contour (before unloading) for the homogeneous model. . . . .	84
4.13	Von-Mises stress contour for separator layers in the heterogeneous model (before unloading). . . . .	85
4.14	(a) Change of velocity and (b) Impact force over time for the updated homogeneous and heterogeneous models. . . . .	85
4.15	Rod impact model based on the UN DOT 38.3 requirements. . . . .	86
4.16	Homogeneous and heterogeneous models for rod impact simulations. . . . .	87
4.17	Deformed jellyrolls and Von-Mises stress contours found from homogeneous and heterogeneous simulations. . . . .	89
4.18	(a) Change of velocity and (b) Impact force over time for rod impact simulations. . . . .	89
4.19	Heterogeneous model for rod indentation simulation. . . . .	90
4.20	Load-displacement curves found from rod indentation experiments and finite element simulation. . . . .	91
4.21	Cross section of jellyroll found from rod indentation simulation. . . . .	92
4.22	Von-Mises stress contour for the cell casing found from rod indentation simulation. . . . .	92
5.1	The process of developing battery module finite element model. . . . .	94
5.2	(a) Homogeneous cell model and (b) Heterogeneous cell model. . . . .	94
5.3	PM12 module containing 12 6P cylindrical cells. . . . .	95
5.4	Finite element model of a PM12 module including homogeneous cells. . . . .	96
5.5	The process of multiscale simulation of impact on battery module. . . . .	97
5.6	Cell boundary segments used for storing displacements data for submodeling. . . . .	98
5.7	Deformed shape of the module including 12 homogenized cells. . . . .	99
5.8	(a) Deformed shape of a homogeneous jellyroll after impact on the module and (b) Deformed shape of the equivalent heterogeneous model. . . . .	100

## LIST OF TABLES

3.1	Lateral impact test configurations: cell orientation and drop mass. . . . .	51
3.2	Test configurations for lateral impact by a rigid bar. . . . .	54
3.3	Cell indentation for various impact configurations. . . . .	56
3.4	Drop time measured by accelerometers and corresponding average accelerations.	57
3.5	Resistance values for crushed cells after impact and steady compression tests.	58
3.6	Estimation of drop mass leading to short circuit. . . . .	64
4.1	Deformed thickness comparison for the cells with horizontal (h) and vertical (v) terminals. . . . .	74
4.2	Average impact force estimation. . . . .	76
4.3	Deformed shape thickness comparison of internal components. . . . .	77
4.4	Cell's deformed thickness under 11.34 <i>kg</i> impact load. . . . .	81
4.5	Updated cell's deformed thickness using LVDT characterizations (11.34 <i>kg</i> impact weight). . . . .	83
4.6	Simulation data for rod impact analysis models. . . . .	88
4.7	Cell's deformed thickness after impact by a rigid rod. . . . .	89

## LIST OF ABBREVIATIONS

<b>2-D</b>	Two-dimensional
<b>3-D</b>	Three-dimensional
<b>APDL</b>	ANSYS Parametric Design Language
<b>ARC</b>	Accelerating Rate Calorimetry
<b>BMS</b>	Battery Management Systems
<b>CID</b>	Current Interrupt Device
<b>CSBC</b>	Copper Slug Battery Calorimetry
<b>CT</b>	Computed Tomography
<b>DMA</b>	Dynamic Mechanical Analysis
<b>DMC</b>	Dimethyl Carbonate
<b>DSC</b>	Differential Scanning Calorimetry
<b>EV</b>	Electric vehicle
<b>FEA</b>	Finite Element Analysis
<b>HEV</b>	Hybrid Electric Vehicle
<b>HPC</b>	High Performance Computing
<b>LIB</b>	Lithium-Ion Battery
<b>LVDT</b>	Linear Variable Differential Transformer
<b>MPP</b>	Massively Parallel Processing
<b>NHTSA</b>	National Highway Traffic Safety Administration
<b>PE</b>	Polyethylene
<b>PP</b>	Polypropylene
<b>PTC</b>	Positive Thermal Coefficient
<b>SEM</b>	Scanning Electron Microscope
<b>TR</b>	Thermal Runaway

## ACKNOWLEDGEMENTS

I would like to express my sincere gratitude to my advisor, Dr. Ilya Avdeev for the continuous support of my Ph.D study and research, for his guidance, patience, understanding and motivation.

My sincere thanks also goes to Alex Francis, for his continuous assistance with experiments, CT-scan reconstruction and his help with publications and presentations throughout this project. I would also like to thank current and past members of the Advanced Manufacturing and Design Lab., Bryan Cera, Daniel Bautista, Douglas Wicker and Molly Pinnekamp for their support and wonderful collaborations.

I must also acknowledge Dr. Benjamin Church for his assistance with LVDT and testing machine trainings, his help with sample molding and for providing us with the DMC solvent. Appreciation also goes out to Seyedmohammad Sadegh Shams and Rahim Reshadi for their assistance with compression experiments. Thanks are also due to Dr. Steven Hardcastle and Afsaneh Dorri for their help with the SEMs, Hamid Erfanian for Microscopy and David Raschke for his help with accelerometers.

I would also like to thank my parents, sisters, friends and my wife for their precious support and encouragement through my entire life.

This research was sponsored by Johnson Controls Inc. I would like to acknowledge Mr. Steve Cash for directing this project and Mr. Paul Frank for CT-scanning battery cells.

---

# Chapter 1

## Introduction

### 1.1 Motivation

Lithium-ion batteries are used in variety of applications from small electronic devices, cell phones and laptops to electric vehicles [1] and even energy storage systems [2]. Increased usage of lithium-ion batteries in automotive applications makes it necessary to understand their mechanical behavior under extreme loading conditions, such as mechanical impact. Although various safety mechanisms have been implemented in individual lithium-ion cells as well as entire battery packs based on the thermal state of the battery [1, 3], there is still a need for better understanding of battery response to extreme loading, which increases the risk of short circuit and subsequent thermal runaway or fire. In 2011 the National Highway Traffic Safety Administration (NHTSA) crash tested a Chevrolet Volt electric vehicle. Three weeks later the car caught fire in a storage lot [4]. NHTSA investigated the incident and believed that intrusion of the transverse stiffener into the battery compartment and leakage of coolant solution onto the energized battery components initiated the short circuit and fire (Fig. 1.1) [5]. In 2013, three Tesla Model S sedans caught fire after being in high-speed accidents (Figure 1.2) [6]. Even though the risk of catching fire is much higher for gasoline vehicles, a fire in a battery powered vehicle gets a lot of attention for various reasons such as fear to a new technology [7]. The concerns regarding lithium-ion batteries catching fire are not limited to electric vehicles. There were many reports of Samsung Galaxy Note7 explosions in the news in 2016 (see Fig. 1.3). A teardown of a Note7 revealed that the phone was designed so that the lithium-polymer battery was tightly packed inside the case to maximize battery capacity (Fig. 1.4). Pressures due to normal battery swelling or high

stresses during normal use would squeeze battery electrodes, causing a short circuit followed by a thermal runaway [8].



**Figure 1.1:** A Chevrolet Volt car before and after fire incident [5].



**Figure 1.2:** Third Tesla Model S catches fire after hitting road debris [6].





**Figure 1.3:** An exploded Samsung Galaxy Note7 smartphone (Credit:Crushader/reddit).



**Figure 1.4:** Extremely tight battery clearances for Samsung Galaxy Note7 [8].

The goal of this study is to develop a framework for battery pack design-for-safety. Such a framework can improve the crash safety of lithium-ion battery packs by investigating prevailing mechanisms of failure as well as identifying existing design parameters and new design concepts that lead to predictable battery response to catastrophic events. In order to design batteries considering safety issues there are several problems that need to be addressed:

- Multiscale nature of the problem
- Multiphysics nature of the problem
- Prohibitive cost of experiments
- Computational complexities

### **1.1.1 Multiscale Nature of the problem**

Prediction of the behavior of lithium-ion battery packs under abnormal conditions is a multiscale problem; that is, as Fig. 1.5 illustrates, it should be studied in different levels from pack level to laminate level because for example, a crushed battery pack or cell can lead to thinning of separator layers inside a cell which in turn can cause an internal short circuit followed by a thermal runaway that propagates to the whole battery pack.

### **1.1.2 Multiphysics Nature of the problem**

In addition to being a multiscale problem, lithium-ion battery failure is known to be a multi-physics phenomenon as it involves electrochemical, thermal and mechanical processes and events. Thermal runaway, the most critical failure mode associated with lithium-ion batteries, may be caused by severe mechanical damage, internal cell faults or it can be a result of problems involving charge, discharge and battery protection devices.

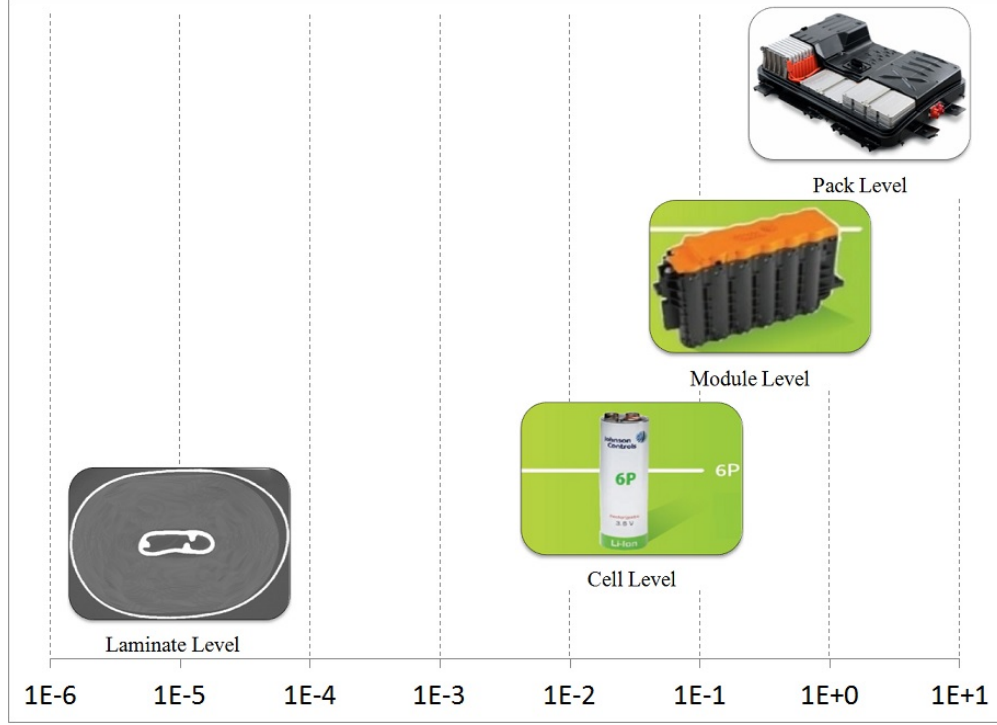


**Figure 1.5:** Various levels in safety analysis of lithium-ion batteries: (a) pack, (b) module, (c) cell and (d) laminate levels (scales in  $m$ ).

### 1.1.3 Prohibitive Cost of Experiments

Considering the complexity and all of the various parameters that affect the safety of lithium-ion batteries, one of the most reliable methods to investigate the behavior of batteries is to perform experiments. However, conducting experiments such as impact tests on battery packs is not applicable because each pack consists of hundreds of cells which make the experiments very costly. Furthermore, because of the risk of explosion, the testing apparatus needs special safety provisions. Thus, generating a battery pack model that simulates the behavior of batteries under various conditions is desirable. Such a model would help to study the effects of different parameters influencing the problem while minimizing the cost.

### 1.1.4 Computational Complexities

Because of the complexity of the battery model, the analysis will be computationally expensive in terms of solution time and CPU resources. That is because individual layers forming the jellyroll are very thin ( $< 75 \mu m$ ) and incorporating these layers in the model increases the total number of elements and decreases the time step size. Even if we neglect modeling individual layers and consider a homogenized material for the jellyroll, the pack model will be very complex as it includes hundreds of cells. Also, we need to define contact between all adjacent cells. Therefore, high-performance computing techniques need to be used for the simulation to achieve the desired results.

## 1.2 Background

Prior studies on lithium-ion batteries can be categorized based on various criteria such as battery safety, scale (layers, cell, module or pack), domains of the problem (structural, thermal, electro-chemistry, multi-physics) and etc.

Safety is one of the most popular research topics on lithium-ion batteries. These batteries combine highly energetic materials with a flammable electrolyte - a system that under thermal, electrical or physical abuse conditions can trigger heat-evolving reactions and gas release that can subsequently cause fire or explosion. Recent reviews of safety mechanisms on the cell level adopted in commercial LIBs [3]. Doughty and Pesaran [9] identified several techniques that improve battery safety, such as safety vents, shutdown separators, less flammable electrolytes, PTC elements and redox shuttle mechanisms. However, pushing the boundaries of current technology to higher energy densities and new active materials will require reevaluation of battery safety [9]. Considerable research efforts had been aimed at experimental measurements of thermal runaway (TR) onset temperatures and energetics of thermally induced failures of lithium-ion batteries, such as differential scanning calorimetry (DSC), accelerating rate calorimetry (ARC), VSP2 adiabatic calorimetry, C80 calorimetry,

oxygen consumption calorimetry and copper slug battery calorimetry (CSBC) [10]. Various experimental and numerical studies of thermal runaway propagation from cell to cell showed that the thermal abuse tolerance of a pack is extremely sensitive to the exothermic cell behavior [11, 12]. The thermal runaway mechanisms are also sensitive to the cell shape and configuration [13]. Penetration induced thermal runaway in a battery pack under various heating conditions showed that it happens when the TR onset temperature is reached at any point in the pack and it also leads to large maximum temperature difference of 593-792C [14]. Overheating induced thermal runaway studies showed unpredictability in thermal runaway propagation and energy/gas release [15]. Thermal runaway is a result of complex electrochemical, materials activity and interactions, discharging rate, packaging and so on. Recent comprehensive review of modeling methods [16] found that thermal runaway mechanisms and prevention measures, including BMS (comprehensive review of state-of-the-art can be found in [17–20]) need to be understood and developed further, especially for the EV and HEV applications. Comprehensive experimental evaluation and review of various separator materials from a safety point of view can be found in [21]. Numerical characterization has evolved from thermal [22] to thermoelectrochemical [23] abuse models to coupling with internal short circuit macro models [24]. Recent experimental (compression, impact, CT-characterization) and numerical (FEA) studies of mechanical response of separators [25–27] and cells [28–31] advanced our understanding of failure initiation mechanisms, but more work has to be done to couple these results with thermoelectrochemical models both on the cell and the pack levels.

There have been studies focusing purely on electrical aspects of lithium-ion batteries. Lu et al. [17] studied the composition of the battery management system (BMS) and its key issues such as battery fault diagnosis and etc. Lam et al. [32] developed a circuit based model for electric vehicle applications and were able to predict the behaviour of a cell under various conditions. Many researchers studied the chemistry of electrodes, anodes, cathodes and electrolyte solutions [33, 34]. Various aspects of heat transfer and thermal

modeling of lithium-ion batteries have also been investigated in the literature [35–39]. These studies include a broad area from thermal characterization and measurements [40–43] to heat management and cooling systems [44–48] and thermal runaway [16, 49, 50] in lithium-ion cells and packs. Numerous analytical and numerical thermal models have been proposed for lithium-ion batteries [23, 51–63]. In order to predict the onset of short-circuit under mechanical abuse conditions, there have been studies combining mechanical, electrical and thermal domains using a multiphysics modeling approach [64–67]. Multiphysics modeling can also provide valuable information regarding heat generation inside battery cells using both analytical [68–70] and numerical approaches [71–74].

Previous research on structural analysis of lithium-ion batteries can be categorized in three groups: laminate level, cell level and pack/module level. In the laminate level, studies have been conducted on characterization of various types of separators, because of their important role in safety and durability of lithium-ion batteries. Roth et al. [75] investigated abuse response of lithium-ion cells consisting of two commercially available single-layer and three-layer separators and showed that the separator plays a significant role in the overall abuse tolerance of these cells. Sheidaei et al. [26] characterized a single-layer polypropylene separator under tension in machine and transverse directions. They conducted tensile, creep and frequency sweep experiments and showed that the mechanical properties are lower in the case of wet separator. A similar study was reported by Avdeev et al. [27] on a tri-layered polymer separator. They conducted Dynamic Mechanical Analysis (DMA) experiments on both dry and saturated membranes in two perpendicular directions and observed that temperature significantly decreases strength and Dimethyl Carbonate (DMC) electrolyte induces greater compliance. Even though they experience repetitive compressive loads during charge and discharge expansion of anode and cathode electrodes, very few studies have been reported on compressive properties of separator membranes. Cannarella et al. [76] used a universal tensile/compression testing machine to find the mechanical properties of a single-layer microporous polypropylene separator over a range of strain rates. They found out that the

softening effects due to DMC solvent are less significant in compression than in tension. To study the role of separator compression due to swelling of electrodes on battery performance, Gennady et al. [77] developed a model for predicting the elastic response of a commercial separator at various strain rates. They showed that by combining viscoelastic behavior of the polymer skeleton and poroelastic behavior resulting from the flow of fluid in the pores, the response of the separator can be determined. A comprehensive study to characterize mechanical properties of two types of separators was performed by Zhang et al. [78, 79]. They identified separators' failure modes and also proposed a criterion for onset of soft short caused by a separator layer. Kalnaus et al. [80] also investigated failure mechanisms and mechanical behavior of three types of separators under tensile loads. In addition to separator layers, lithium-ion battery electrodes have also been characterized in the literature[81]. On the cell level, finding an accurate constitutive model for the jellyroll has always been a concern. Despite the nonlinear behavior of the jellyroll, various homogenization methods have been proposed in the literature to find its average mechanical properties. Greve and Fehrenbach [82] developed a finite element model using pressure dependent isotropic Raghava yield criterion as the constitutive model of the jellyroll and applied Mohr-Coulomb criterion to predict fracture inside the jellyroll. Compression experiments were also used to find average mechanical properties of the jellyroll as well as individual layers for pouch cells [83, 84]. Sahraei et al. [85] used the aforementioned mechanical properties for cylindrical cells of similar chemistry. Classical laminated shell theory was used by authors to find the homogenized material response of the jellyroll using a multilinear interpolation of the strain-stress curve [86]. Wierzbicki and Sahraei reported a hybrid experimental-analytical approach to find the average stress-strain properties of the jellyroll in a radial direction with the assumption that the load was carried by a central rectangular part of the jellyroll under the punch [87]. In a previous paper, the authors carried out a set of experiments on flattened jellyroll samples to find an average stress-strain relation for the jellyroll [28]. Wang et al. [88] also characterized jellyroll's mechanical properties for a cylindrical cell. There have also

been simulations where all the individual electrode/separator layers have been included in the model [29, 89]. Chatiri et al. [90] used the LS-DYNA layered thick shell formulation to model the thin layers of the jellyroll. However, this formulation does not seem to be suitable for elements with high aspect ratios and models including soft materials such as a polymer separator. A 2-D layered model was also analyzed by Kim et al. [91] to simulate the expansion of jellyroll during charging. Although transverse loads on battery cells seems to be the focus on most of the published research, axial compression on cylindrical batteries have also been studied [92]. Marcicki et al. [93] proposed a simulation framework for impact modeling of battery cells using LS-DYNA. Effects of road-induced vibrations on durability of lithium-ion batteries were also investigated by Hooper et al. [94–96]. Luo et al. [97] studied pouch cells under indentation loads and indentified internal short circuit mechanisms. Pouch and elliptical cells were also impact tested by [98]. Their results indicated that test speed and presence of electrolyte significantly changes the critical force. Tsutsui et al. [99] realized battery’s state-of-charge and deformation rate affect cell’s stiffness. In the pack level, because of the complexity of the problem, homogenized mechanical properties of the jellyroll must be implemented in the model. Xia et al. [100] developed a methodology for analyzing damage of cells and battery packs due to ground impact.

## 1.3 Approach

Despite the valuable studies that were mentioned on lithium-ion batteries, no published research was found on 3-D simulation of impact on larger lithium-ion cells that accounts for individual jellyroll layers using solid elements. Such a simulation will help find the potential locations where separator thinning can lead to short circuit and thermal runaway.

Dealing with energy storage devices and especially lithium-ion batteries, various aspects need to be considered in a design process (see Fig. 1.6). First of all, suitable design variables need to be considered to satisfy all the governing constraints including manufacturing



processes. Also, one of the factors that play a big role in energy storage devices is sustainability and how environmentally friendly they are. Finally, a key aspect of any energy storage device including batteries is safety which is the topic of this study. Safety needs to be addressed at the cell, module and pack levels. Failure at one level can quickly spread to more severe failures at a higher level. Safety cannot be evaluated by one criterion or parameter. Qualitatively, we can improve safety by: (a) reducing probability of an event and (b) lessening the severity of outcome, should an event occur [101]. There have been studies on failure modes, safety and reliability of lithium based batteries. Levy [102] has proposed some approaches to study and improve the reliability and safety of lithium batteries and also some considerations about handling and disposal of the batteries. Manuel and Maurer [103] performed a fault tree analysis on a large spacecraft battery. They found the reliability of the battery module for a single spacecraft mission and also for one-month storage of the battery. Fouchard and Lechner [104] have described a number of failure modes for secondary lithium batteries and have formed fault tree diagrams with venting incident as the top event. Eom et al. [105] conducted different safety abuse tests and performed a life prediction on lithium batteries using a Weibull distribution. For the case of lithium-ion batteries, thermal stability is probably the most important parameter that affects safety in cells, modules and battery packs. Typical failure modes of lithium-ion batteries are [9]:

- Thermal abuse
- Physical damage
- Charge and discharge failures
- Short circuit

Various safety devices such as current interrupt device (CID), positive temperature coefficient (PTC) and etc are incorporated into cells, modules and battery packs to protect against abnormal conditions. These safety devices are one of the reasons for the safe operation of cells and battery packs in the field [9]. However, even with all of these safety

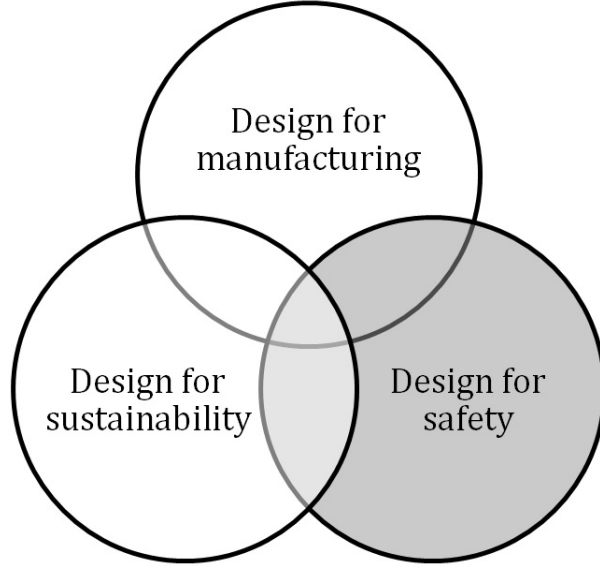


**Figure 1.6:** Battery pack design aspects.

provisions, many failure mechanisms can lead to thermal runaway and fire. Most of these failure modes include some kind of internal or external short circuit especially for the case of crash or impact. In order to find the potential failure regions of a lithium-ion battery, a multiscale framework is developed for explicit finite element simulation of battery packs (Fig. 1.7). In this framework, using highperformance computing techniques, a battery module is first analyzed to find the critical cell or cells. The analysis is then continued in a lower level with a higher accuracy. In the final stage, the behavior of the jellyroll can be studied in the laminate level in order to find the critical regions with a high probability of separator failure or internal short circuit.

This study is an attempt to investigate impact on 6P cylindrical lithium-ion cells (3.6 V/6.8 Ah, NCA/Graphite, 140×40 mm) and PM12 modules manufactured by Johnson Controls Inc. (see Fig. 1.8). A 6P cell consists of four major mechanical components (Fig. 1.9): (1) a roll of active battery materials (anode, cathode and separator sheets) or a jellyroll, (2) a center hollow aluminum tube, (3) an aluminum casing and (4) a polyetherimide spacer. The cathode is made of aluminum foil coated with LiNiCoAlO<sub>2</sub> active material on both sides. The anode is made of graphite-coated copper foil, and a thin trilayer (PP/PE/PP)

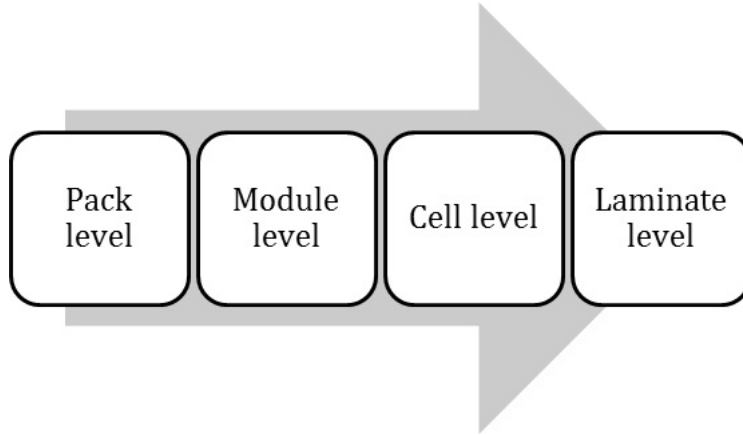


**Figure 1.7:** Multiscale simulation framework.

separator sheet was used to keep them apart.

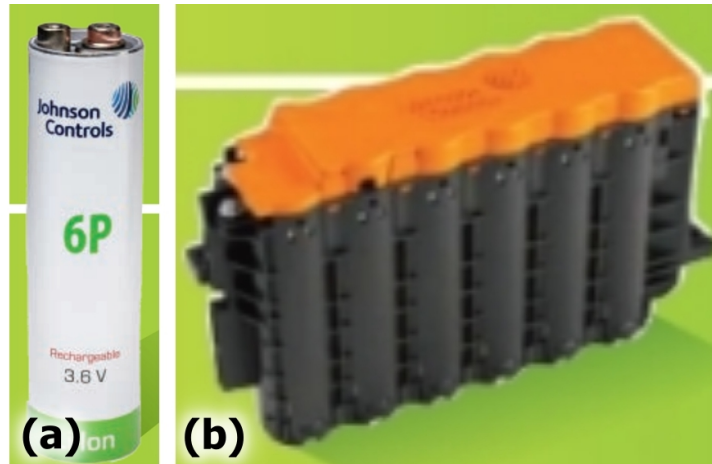


**Figure 1.8:** (a) 6P cylindrical cell and (b) PM12 power module made by Johnson Controls Inc. (Source: johnsoncontrols, 2015).

In a battery pack, the two prevailing impact modes on an individual cell are in: (1) lateral and (2) lateral directions (Fig. 1.10). Considering the layered structure of the jellyroll, in the lateral impact mode, jellyroll stresses will be mostly compressive and in the lateral direction (normal to individual layers). Similarly, axial impact causes high compressive stresses in axial direction and small stresses in other directions because of very small Poisson's ratio of the jellyroll.

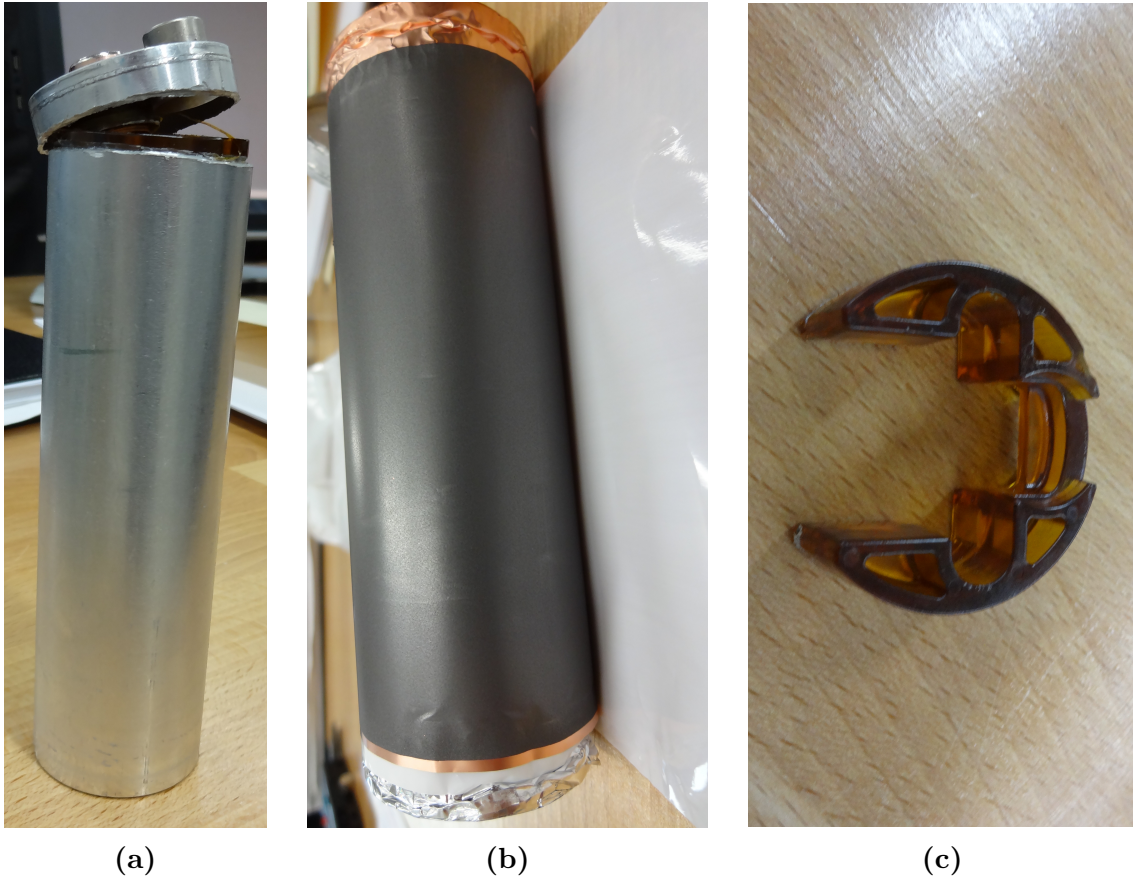


**Figure 1.9:** Cylindrical cell components: (a) casing, (b) jellyroll and inner tube, (c) spacer.

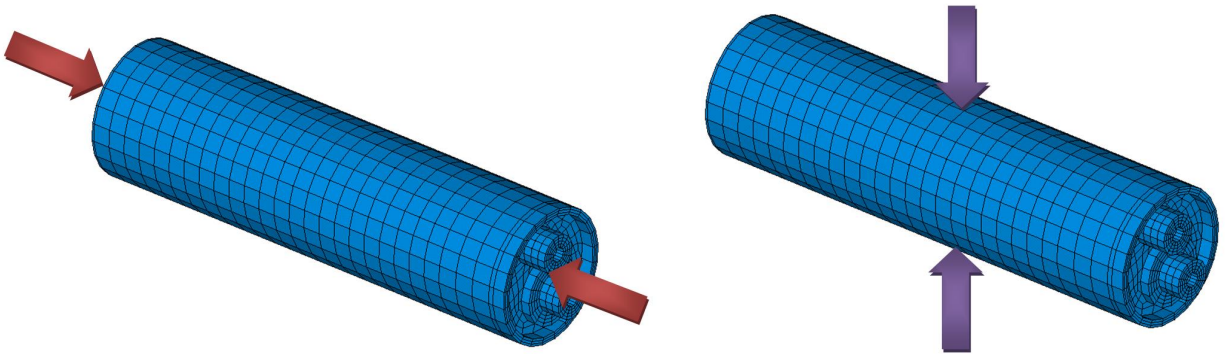


**Figure 1.10:** Two impact modes: (1) axial direction and (2) lateral direction.

This research provides a framework for multiscale simulation of lithium-ion battery modules under impact loads. The focus of the present work will be on lateral impact mode and also lateral impact by a rigid rod. To properly carry out this simulation, first jellyroll will be characterized and homogenized using several different methods in Chapter 2. Stress-strain curves for individual jellyroll layers will also be characterized under dry and saturated conditions. Chapter 3 will cover the conducted experiments in the cell level using a custom designed drop test apparatus. Results from impact between rigid plates, impact using a rigid rod and rod indentation experiments will be discussed. Post-processing the tested samples using CT-scanning and microscopy will also be explained. Because impact testing live cells (i.e. cells with electrolyte) needs serious safety provisions, dry cells will be impact tested throughout this study and all of the simulations consider dry cells. However, the method can be also applied to live cells. Cell level impact simulation process will be explained in Chapter 4. Results from jellyroll characterization and homogenization will be incorporated in 3-D homogeneous and heterogeneous/layered finite element models to simulate cell's impact and indentation scenarios using commercial software LS-DYNA. Chapter 5 will discuss the multiscale simulation process for PM12 module utilizing the developed homogeneous and heterogeneous 6P cell models. Assembly of the module containing homogeneous cell models will be solved to characterize their impact response. The most critical battery cell will be chosen to be solved using the heterogeneous model which incorporates individual jellyroll layers. Using this approach, thickness change of individual layers can be studied. Summary of findings will be provided in Chapter 6.

---

## Chapter 2

### Cell Level: Jellyroll Characterization/Homogenization

Because of the thinness of jellyroll layers (in the order of 25-70  $\mu m$ , see Fig. 2.1), computationally, modeling each individual layer in the jellyroll during an impact is expensive even for one cell, not to mention an entire pack. Thus, our objective was to replace the heterogeneous jellyroll with an equivalent (mechanically) homogeneous material. In order to determine an accurate homogenized material model for the jellyroll, two experimental approaches were considered: (1) a direct compressive uniaxial test of flattened jellyroll samples and (2) homogenization using the principle of virtual work applied to cylindrical samples. The jellyroll material behavior is nonlinear due to the fact that all individual layers forming the jellyroll, i.e. anode, cathode and separator, exhibit nonlinear material behavior under large strains[26, 87, 106]. Therefore, for finite element simulation purposes, a material model has to be derived that accommodates nonlinear stress-strain curves in both radial and axial directions. An isotropic material model of the jellyroll was considered. The stress strain relation found from the homogenization of the jellyroll will be incorporated in jellyroll's material model in Chapter 4 and 5.

## 2.1 Jellyroll Homogenization

### 2.1.1 Direct Homogenization Using Flattened Jellyroll

Jellyroll samples were prepared by removing an original full length jellyroll from a dry 6P cell and cutting it into one-inch long cylindrical pieces (see Figure 2.2a). The samples were then cut in radial direction and flattened after the inner aluminum tube was removed (see Figure 2.2b). Figure 2.3 depicts a flattened sample under compression between two flat



**Figure 2.1:** Jellyroll layers: coated copper, coated aluminum and separator layers.

rigid plates. Three samples were tested using an Instron 3369 universal testing machine, and load-displacement curves were recorded for loads starting from 0  $kN$  and reaching 52  $kN$  (see Figure 2.4). It was assumed that only the rectangular area under the plates carried the compressive load. Therefore, stress-strain curve could be calculated assuming a constant cross sectional area. Figure 2.5 shows the stress-strain curves derived for the flattened jellyroll samples. The concave-upward shape of the stress-strain curve suggests that there is no visible yield strength and that the stress is considerably small for the lower strain values. This can be attributed to the porosity of jellyroll layers that causes the material to be very compressible with a small value of the Poisson's ratio.

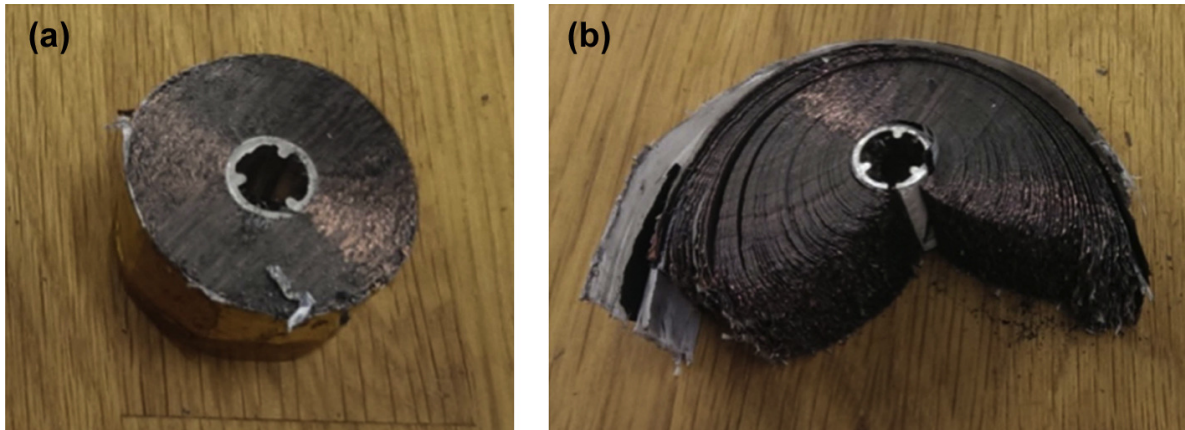


**Figure 2.2:** (a) A jellyroll sample with the metal core and (b) a jellyroll after being cut in a radial direction.



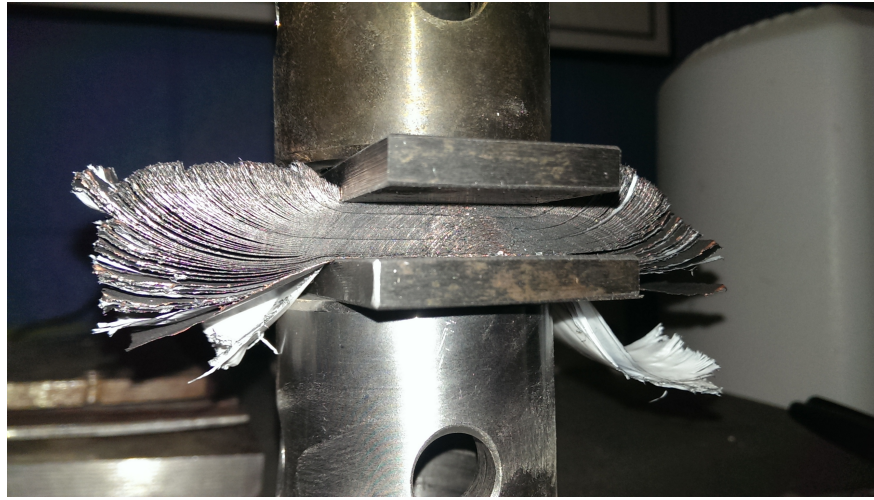


**Figure 2.3:** Flattened jellyroll sample under uniaxial compression.

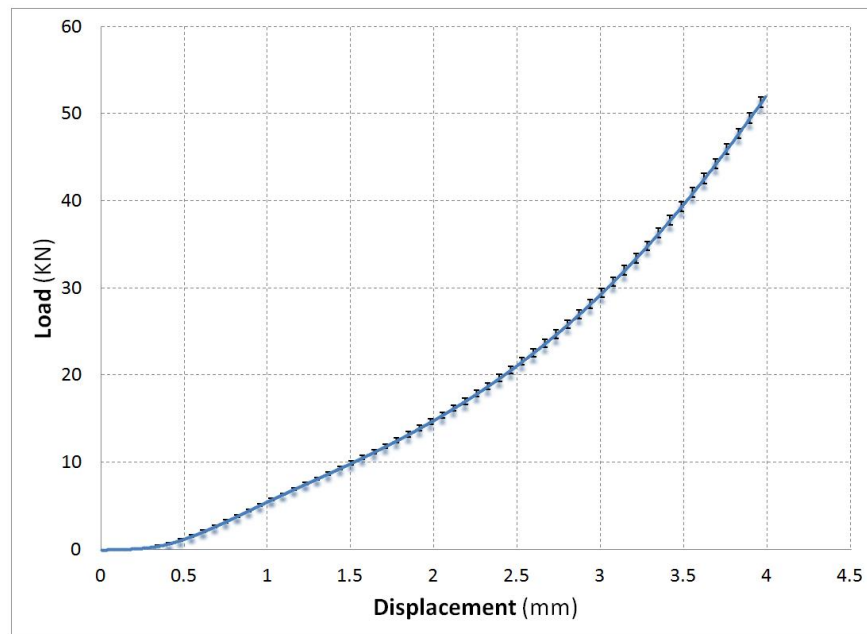


**Figure 2.4:** Load-displacement of flattened jellyroll under compression ( $n = 3$ , relative  $SD = 1.2\%$ ).



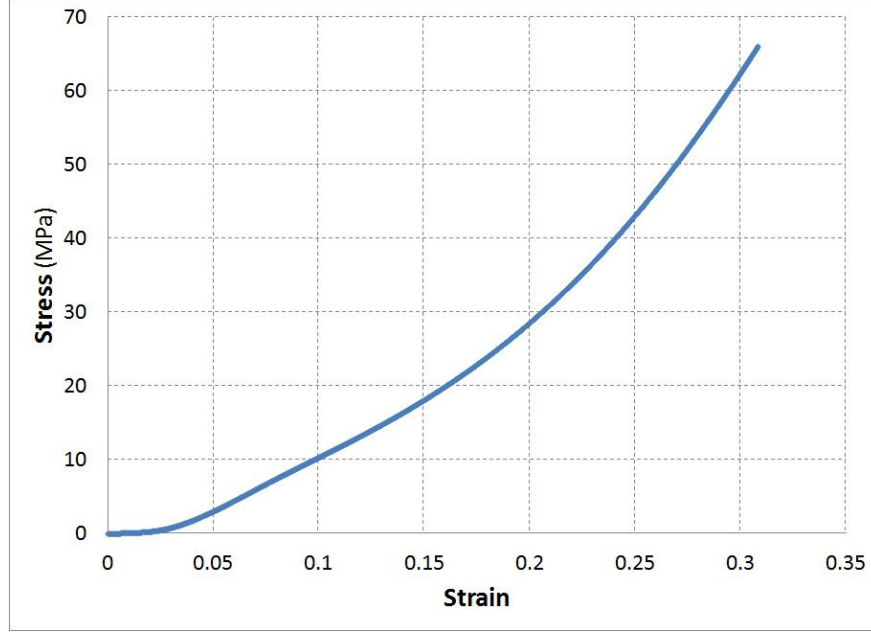


**Figure 2.5:** Stress-strain curves for flattened jellyroll samples.

### 2.1.2 Indirect Homogenization Using Virtual Work Principle

The direct homogenization method, presented earlier, requires extensive cell manipulations, which might not be feasible in many lab environments, especially when dealing with live cells. An alternative homogenization method, based on virtual work principle, was first proposed by Wierzbicki and Sahraei for commercial 18,650 cells [87]. In this chapter, we report on extending this method to be applied to larger cells. The virtual work results are then compared to data obtained from the direct method.

In this hybrid experimental/analytical approach, we find the stress-strain relation of the jellyroll using cylindrical samples rather than flattened ones. It is assumed that during crushing tests, the compressive load is mainly carried by the central rectangular area of the jellyroll [87]. Load-displacement relation is obtained from compression tests of jellyroll pieces in the lateral direction. The virtual work principle is then used to calculate an average stress and strain in terms of the crush distance. Average stress and strain values can be calculated as:

$$\sigma_{av} = \frac{2P(w)}{\pi Lw} \quad (2.1)$$

$$\varepsilon_{av} = \frac{w}{2R} \quad (2.2)$$

where  $P(w)$  is the crush load as a function of crush distance,  $w$  is the vertical displacement of the plates,  $L$  is the sample length in axial direction, and  $R$  is the outer radius of the sample (Fig. 2.6).

In order to be able to accurately calculate average stresses and strains in the jellyroll samples, we had to enhance the formulation proposed in Ref. [87]. In this investigation, the outer diameter of the 6P-JCI cell is about twice the size of an 18,650 cell. Consequently, the inner diameter of the aluminum core is also larger. Furthermore, during lateral compression tests of the jellyroll, it was observed that the load remains very small during the first stage of the test until the inner hole closes. At this point, load starts to increase significantly as the jellyroll carries the compressive load. In order to increase the accuracy of calculations, the flat section of the load-displacement can be discarded. This means that the starting point of the calculations changes accordingly, i.e. the initial geometry will be a smaller cylinder with diameter equal to the distance between the flat plates when the load starts to increase significantly (see Fig. 2.7).

In the original virtual work homogenization method for smaller cells, the cross sectional area of the cylindrical sample that carried the compressive load,  $S$ , was assumed to depend only on radius,  $R$ , and punch size,  $b$  [87]. However, for larger cells, the cross-sectional area that takes the load is also a function of  $r$ , instantaneous radius of the semi circles in the deformed jellyroll (see Fig. 2.8). This assumption significantly affects the results, especially for larger strain values. Therefore, in this study the cross sectional area,  $S$ , is calculated as:

$$S = rb \quad (2.3)$$

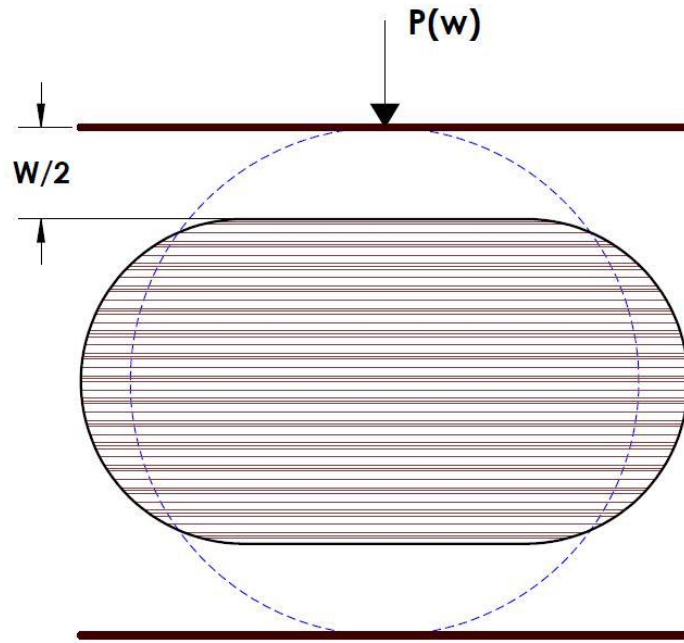


**Figure 2.6:** Schematics of crushed jellyroll; force and displacement.

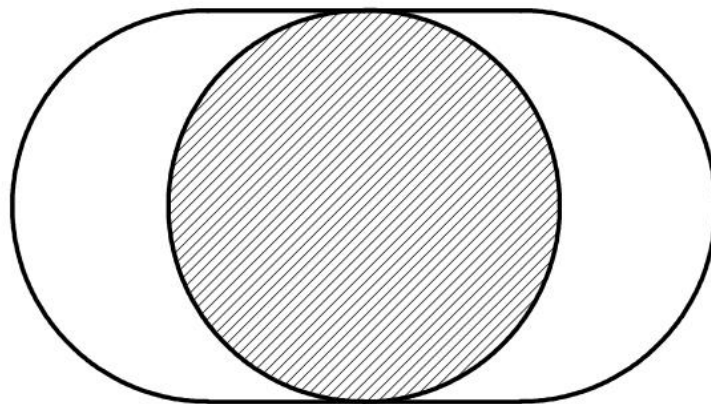


**Figure 2.7:** Equivalent cross section for homogenized stress-strain calculations.

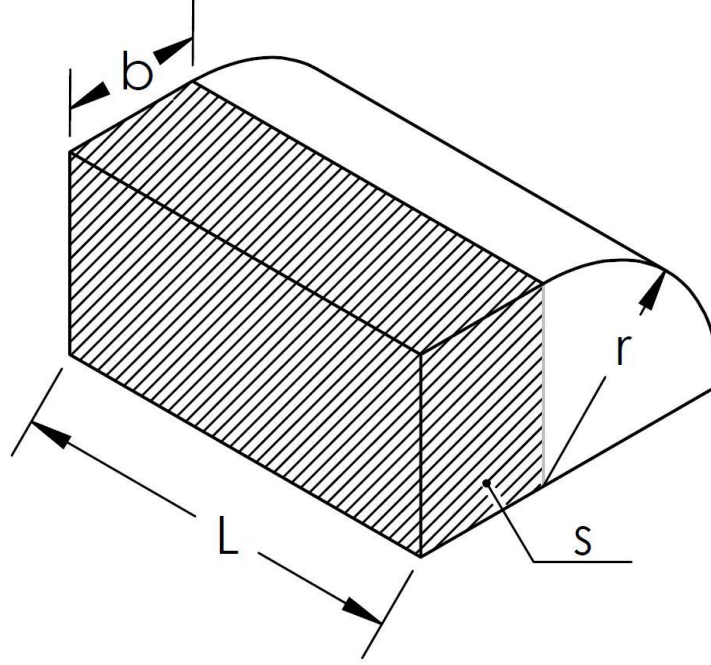


**Figure 2.8:** Dimensions of crushed jellyroll.

The effective punch width can be calculated as:

$$b = \frac{\pi}{4}w \quad (2.4)$$

Therefore:

$$r = R - \frac{2b}{\pi} \quad (2.5)$$

The effective loaded cross-section,  $S$ , can be found in terms of crush distance,  $w$  as:

$$S = rb = \frac{\pi}{4}Rw - \frac{\pi}{8}w^2 \quad (2.6)$$

Average strain is calculated using the following integration over time [87]:

$$\varepsilon_{av} = \int_0^t \dot{\varepsilon}_{av} dt = \int_0^t \frac{\pi}{4} \frac{w\dot{w}}{S} dt \quad (2.7)$$

By substituting  $S$  from Eq. 2.6 into Eq. 2.7 and performing a change of variable, the

simplified average strain formula is given by:

$$\varepsilon_{av} = \int_0^w \frac{dw}{2R - w} = \ln\left(\frac{2R}{2R - w}\right) \quad (2.8)$$

By eliminating the crush distance from stress and strain equations, stress-strain relation can be determined. Solving Eq. 2.8 for  $w$ , we obtain:

$$w = 2R(1 - e^{-\varepsilon}) \quad (2.9)$$

In order to use the above calculations to estimate the homogenized mechanical properties, a set of transverse compression tests on the jellyroll pieces was performed. The casing and the aluminum core were carefully removed after the cell was cut into inch-long (in axial direction) samples. The samples were compressed between two flat steel plates at a rate of  $1 \text{ mm/min}$ . Applied load and plate displacement were recorded during the experiments.

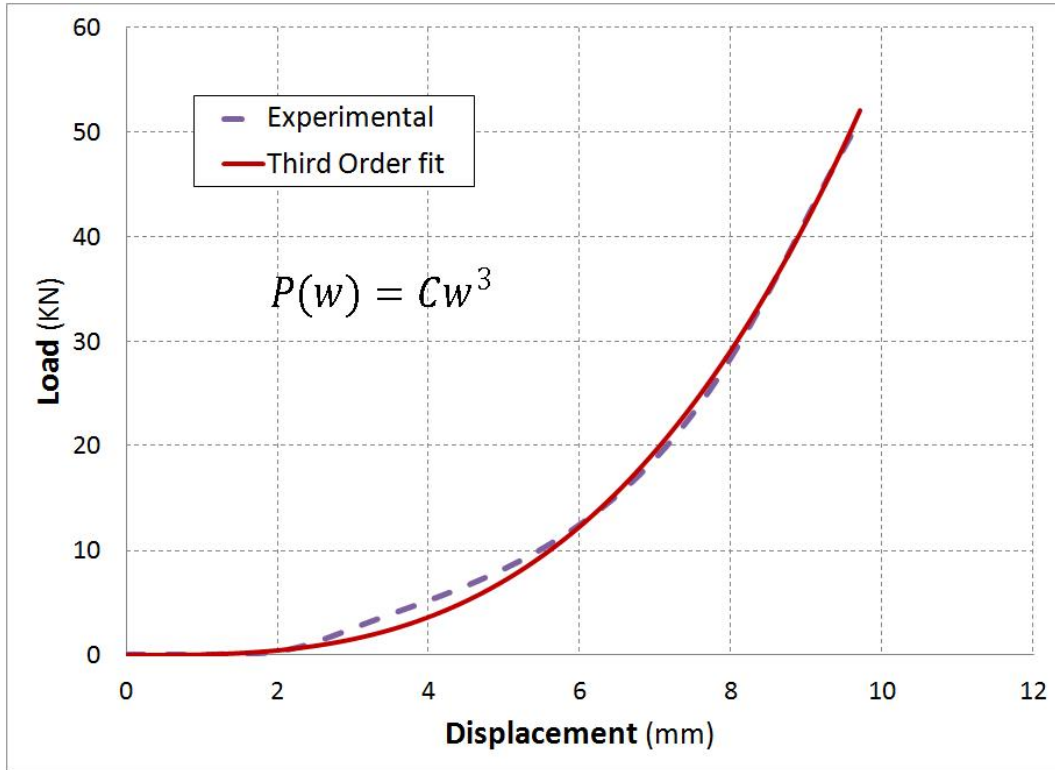


**Figure 2.9:** Load-displacement relation and its third order interpolation.

The obtained load-displacement curve can be interpolated fairly accurately with a third-order polynomial function as shown in Fig. 2.9:

$$P(w) = Cw^3 \quad (2.10)$$

where constant  $C$  equals to  $57 \text{ N.mm}^3$ . By substituting Eqs. 2.9 and 2.10 into Eq. 2.1, the average stress can be found in terms of average strain, which is depicted in Fig. 2.10.

$$\sigma_{av} = \frac{2C}{\pi L} \{2R(1 - e^{-\varepsilon_{av}})\}^2 \quad (2.11)$$

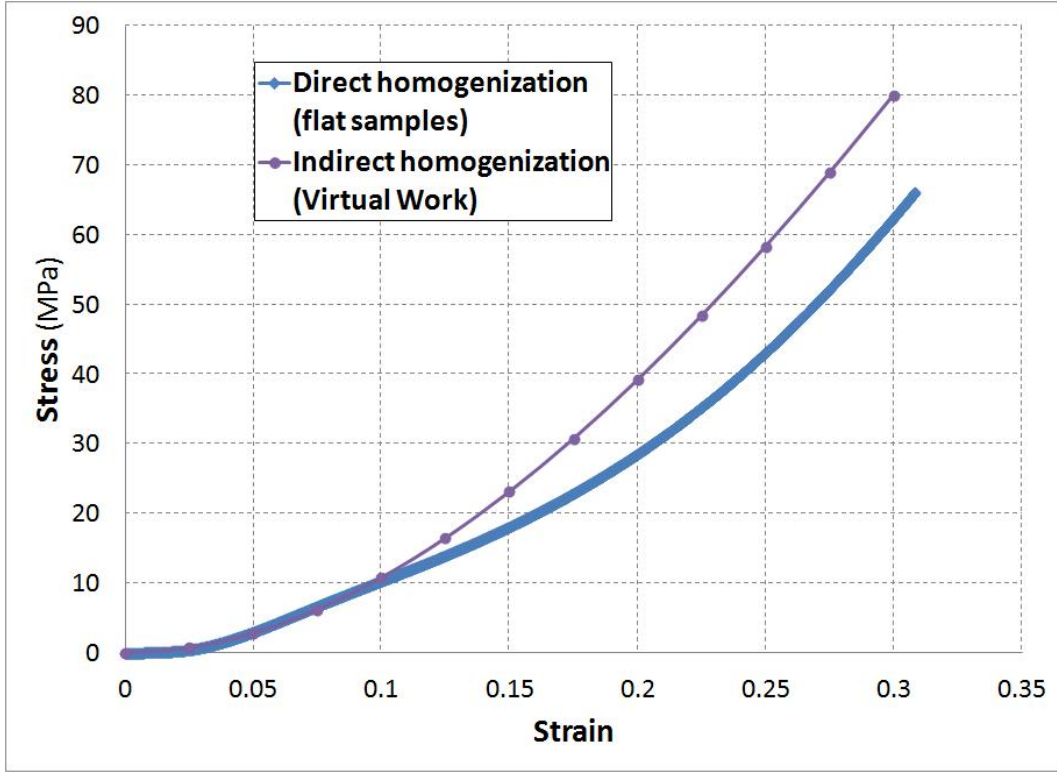


**Figure 2.10:** Stress-strain curves found from the two homogenization methods.

When comparing the results of the two homogenization methods in terms of the stress-strain curve of the jellyroll material, it can be observed that curves diverge at strains exceeding 0.1, with the difference in stress being as large as 22% for strains equal to 0.3 (see Fig. 2.10). The difference can be attributed to the fact that in the virtual work method

uniaxial state of stress is probably not a very accurate assumption, and there will be stresses in both axial and radial directions because of the integrity of jellyroll layers. The presence of an inner core also affects the accuracy of results. On the other hand, the stress-strain relation found from the flattened tests is directly derived from the experiments. Besides, the issues such as biaxial state of stress and inner hole will not be available in the case of direct method. Therefore, it is believed that, direct homogenization is more accurate than the virtual work approach.

### 2.1.3 Homogenization of Wet Samples

Because battery cells are filled with electrolyte, the stress- strain relation found from dry jellyroll samples cannot be used to model live battery cells. Therefore, a second set of experiments was conducted to determine how compressive strength of the jellyroll changes while saturated in a common lithium-ion solvent.

The organic solvent, dimethyl carbonate (DMC), was selected because it is non-volatile and is commonly used in lithium-ion batteries [27]. Using the same procedure as the dry cell, three samples were prepared by cutting the jellyroll into one-inch long pieces. They were also cut in the radial direction before being saturated in DMC electrolyte for 24 hours (see Fig. 2.11a). The testing procedure was identical to dry samples. Fig. 2.11b shows one of the wet samples being compressed. The measured load-displacement curves for the three samples are plotted in Fig. 2.11c. The mean value is very close to the curve extracted for dry samples, however being more scattered, the standard deviation of saturated samples is larger (4.5% compared to 1.2%) which can be due to the sliding of layers on each other that changes the effective cross sectional area. The stress-strain relation is calculated for saturated samples and is compared to the one found for dry jellyroll in Fig. 2.11d. Negligible difference between the stress-strain relations of wet and dry jellyroll suggests that the presence of solvent does not significantly affect the compressive mechanical properties of the jellyroll in the lateral direction. Assuming the majority of load during impact is carried by the jellyroll [87], we can

conclude that instead of live cells, dry cells can be tested to achieve a reasonable estimate of how they will structurally deform under impact loads.

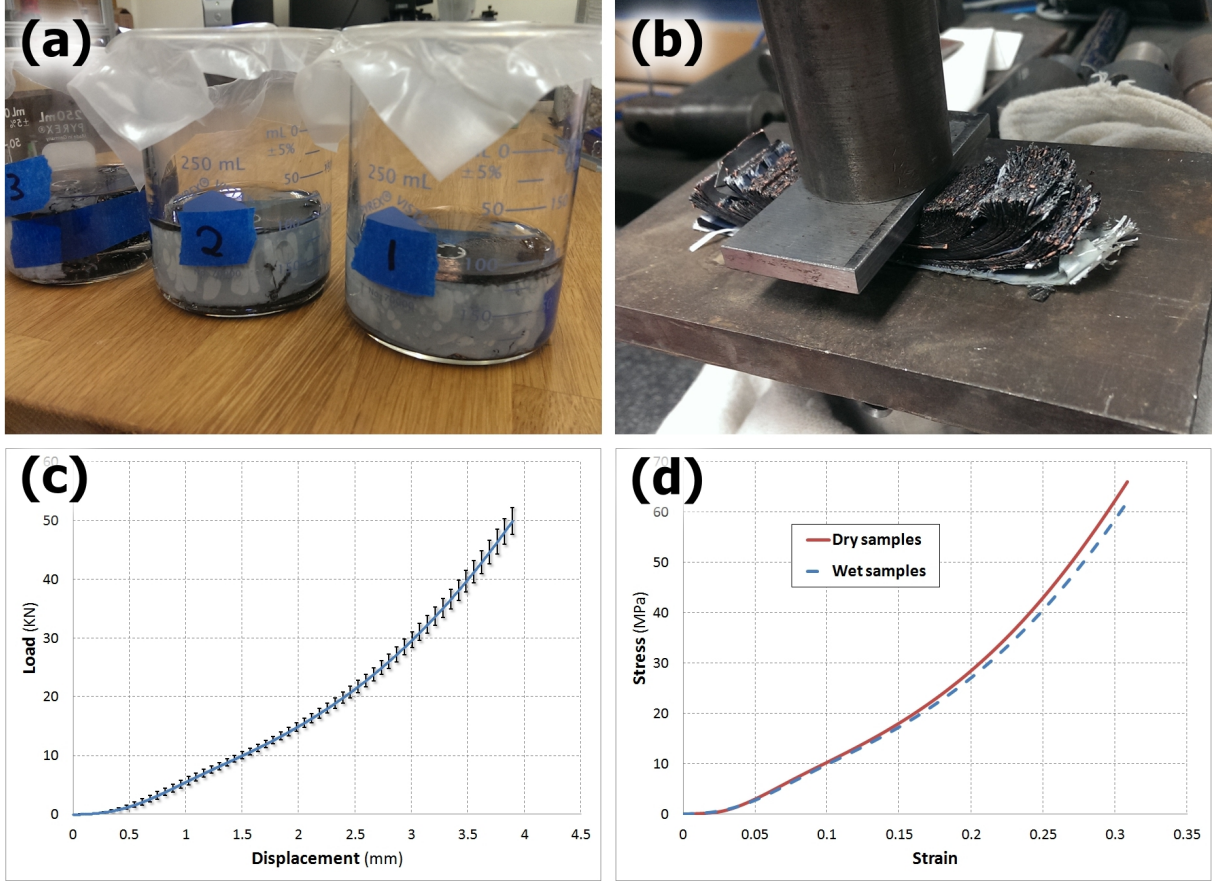


**Figure 2.11:** (a) Jellyroll samples being soaked in electrolyte, (b) Wet jellyroll sample under compression, (c) Load-displacement curve for wet jellyroll samples under compression ( $n = 3$ , relative  $SD = 4.5\%$ ) and (d) Stress-strain curve comparison for dry/wet jellyroll samples.

## 2.2 Characterization of Individual Jellyroll Layers

In addition to homogenized radial properties of the jellyroll, the strength of individual components was measured by performing lateral compression tests on stacks of coated aluminum, coated copper and separator layers individually.



### 2.2.1 Characterization of Anode and Cathode Layers

The samples were prepared by unrolling the jellyroll after being taken out of the cell casing. Then, in order to assure a constant geometry among the samples, layers of anode and cathode current collectors were cut along the perimeter of an aluminum template with an X-ACTO knife. Each strip was 41 *mm* long and 26 *mm* wide. For each sample, 150 layers of identical materials were stacked carefully using a clamp, shown in Fig. 2.12a and 2.12b. Similar to jellyroll experiments, four anode/cathode samples were tested between two steel plates using an Instron 3369 machine (see Fig. 2.12c and 2.12d). The samples were compressed at a rate of 1 *mm/min* and the cross-sectional area under the punch was 607 *mm*<sup>2</sup>. The measured load-displacement curves (Fig. 2.12e) were converted into stress-strain curves of the individual components, shown in Fig. 2.12f. Comparison of the stress-strain relations of coated Al and Cu electrodes shows that coated aluminum layers are almost twice as stiff as coated copper layers. Considering the fact that copper's bulk modulus of elasticity is about 67% higher than that of aluminum, these results show that anode/cathode coatings have a more important role in compressive strength of the jellyroll compared to the current collectors.

### 2.2.2 Characterization of Separator's Mechanical Response

The main function of a separator layer is to prevent physical contact and short circuit between the positive and negative electrodes while promoting the movement of ions from one electrode to the other during battery charge and discharge. In order to increase the safety, most commercial lithium-ion batteries utilize a shut-down mechanism by using polyethylene (PE), polypropylene (PP) or laminates of both materials as a separator. In case of a short circuit inside a cell, when the polyethylene membrane reaches a temperature of about 130°C, the shut-down function is obtained by closing the pores due to high temperature, stopping the transport of ions and shutting the cell down. In many larger industrial batteries, a

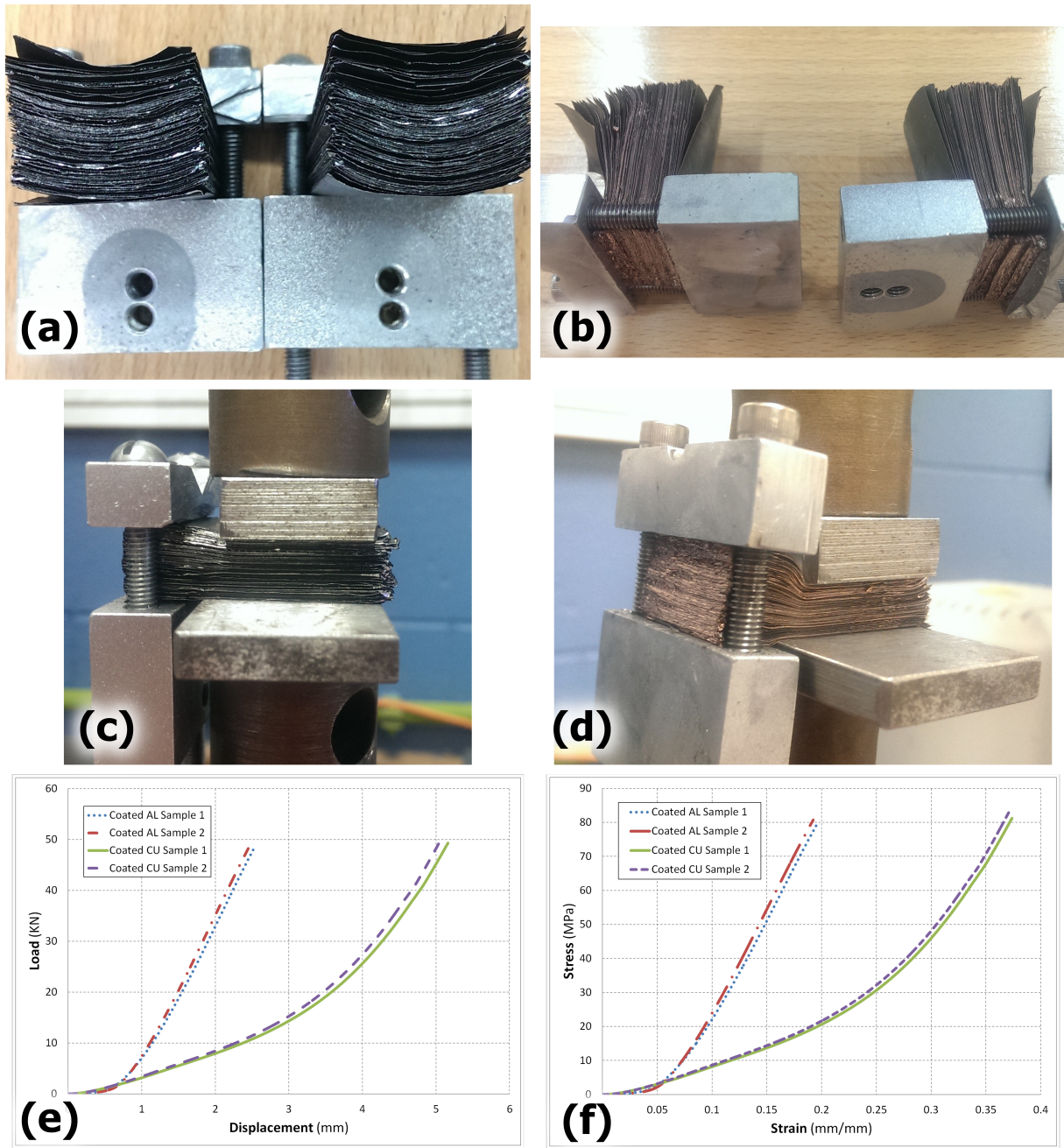


**Figure 2.12:** (a) Coated aluminum layers, (b) Coated copper layers, (c) Compression test of coated aluminum sample, (d) Compression test of coated copper samples, (e) Measured load- displacement curves and (f) Calculated stress-strain curves for aluminum and copper layers.

trilayer separator is used where a polyethylene is sandwiched between two polypropylene layers. Because the melting temperature of PP layers are higher, they will stay intact within the shut-down temperature while PE layers will melt, closing the pores.

Because of the important role of separators on battery safety, it is crucial to understand how they react to compressive loads that arise during crush accidents. Similar to aluminum and copper compressive samples, stacks of separator layers were tested under lateral compression to obtain the stress strain relation and to observe how the separator's microstructure is changing under lateral load. Each sample consisted of 224 layers where each layer was cut along the perimeter of an aluminum template with an X-ACTO knife fitted with a #2 blade. The total thickness of the stack was  $5.69\text{ mm}$  (see Fig. 2.13a) and a Steel plate with dimensions  $24.6 \times 23.9\text{ mm}$  was used to apply the compressive load as shown in Fig. 2.13b. Two samples were tested using a TestResources universal testing machine with a clamp speed of  $0.3\text{ mm/min}$ .

The recorded load-displacement relation is plotted in Fig. 2.13c. The load drop in the curve is probably a sign of failure in one of the PP or PE layers, while the other layer can still carry more load. The calculated stress-strain curve is compared to the results for coated copper and aluminum in Fig. 2.13d. As expected, separator layers are significantly softer than electrodes, hence will deform much more under compression. This means when the battery is crushed in the lateral direction, there is a considerable chance of occurrence of separator thinning which can lead to local failure and short circuit.

In order to see how the separator's microstructure has changed after being compressed, scanning electron microscope (SEM) images were used to look at the surface and cross section of a separator layer. Fig. 2.14a and 2.14b compare a single layer's surface SEM before and after compression test. The surface SEM only shows the PP pores and it is clear from the images that the pores have become significantly smaller when the PP layer is collapsed due to compression. This can slow down or stop transfer of ions when the battery is crushed which can in turn prevent occurrence of thermal instabilities. The three layers of a single separator

membrane, i.e. PP/PE/PP can be seen in Fig. 2.14c. Comparing the original separator layer to the one after the compression (Fig. 2.14d), illustrates how the total thickness of the membrane is decreased from  $20\text{ }\mu\text{m}$  to about  $10\text{ }\mu\text{m}$ , although the relative thickness of PP and PE layers seems to remain constant.

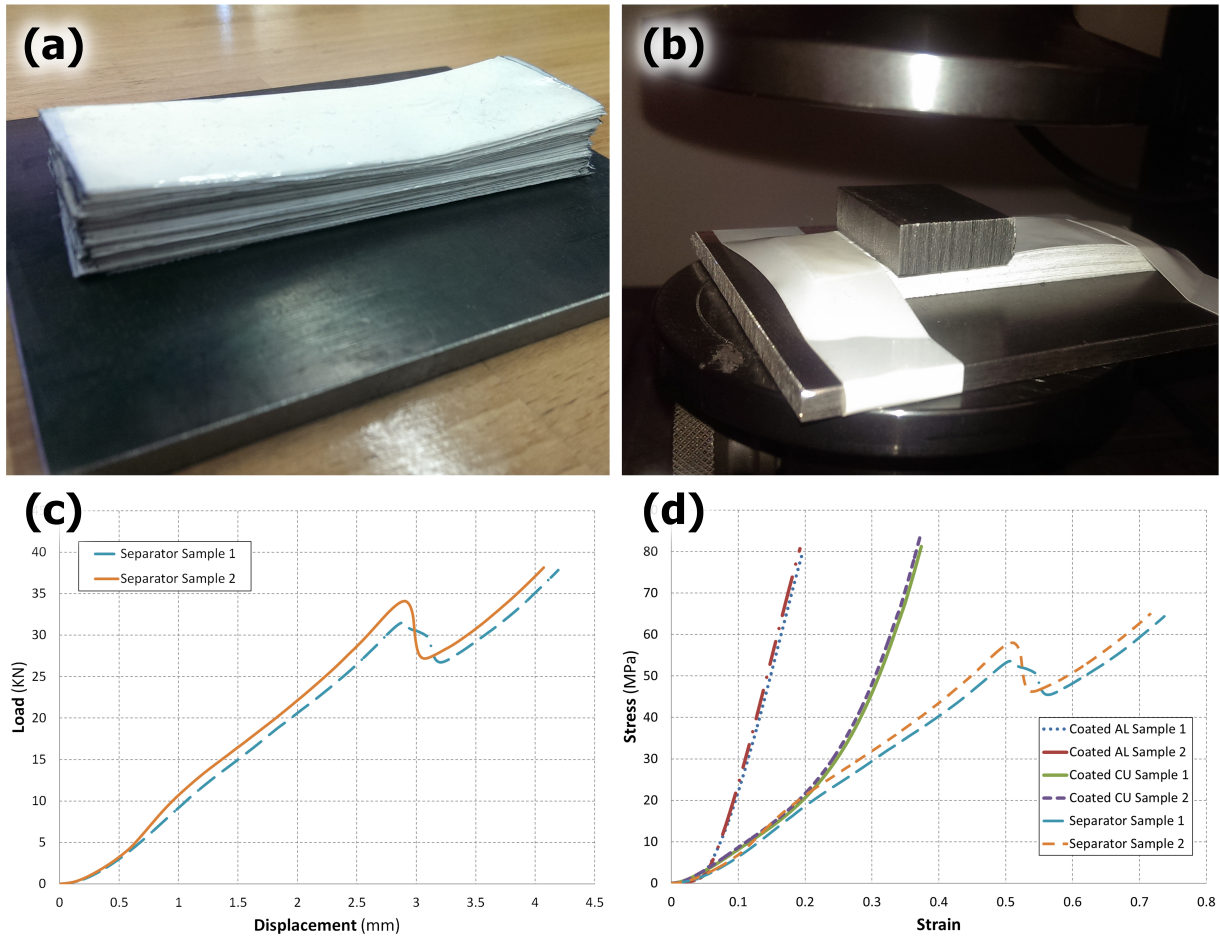


**Figure 2.13:** (a) Stack of 224 Separator layers, (b) Sample before being compressed, (c) Load-displacement curves for separator samples and (d) Stress-strain relation comparison for individual jellyroll layers.

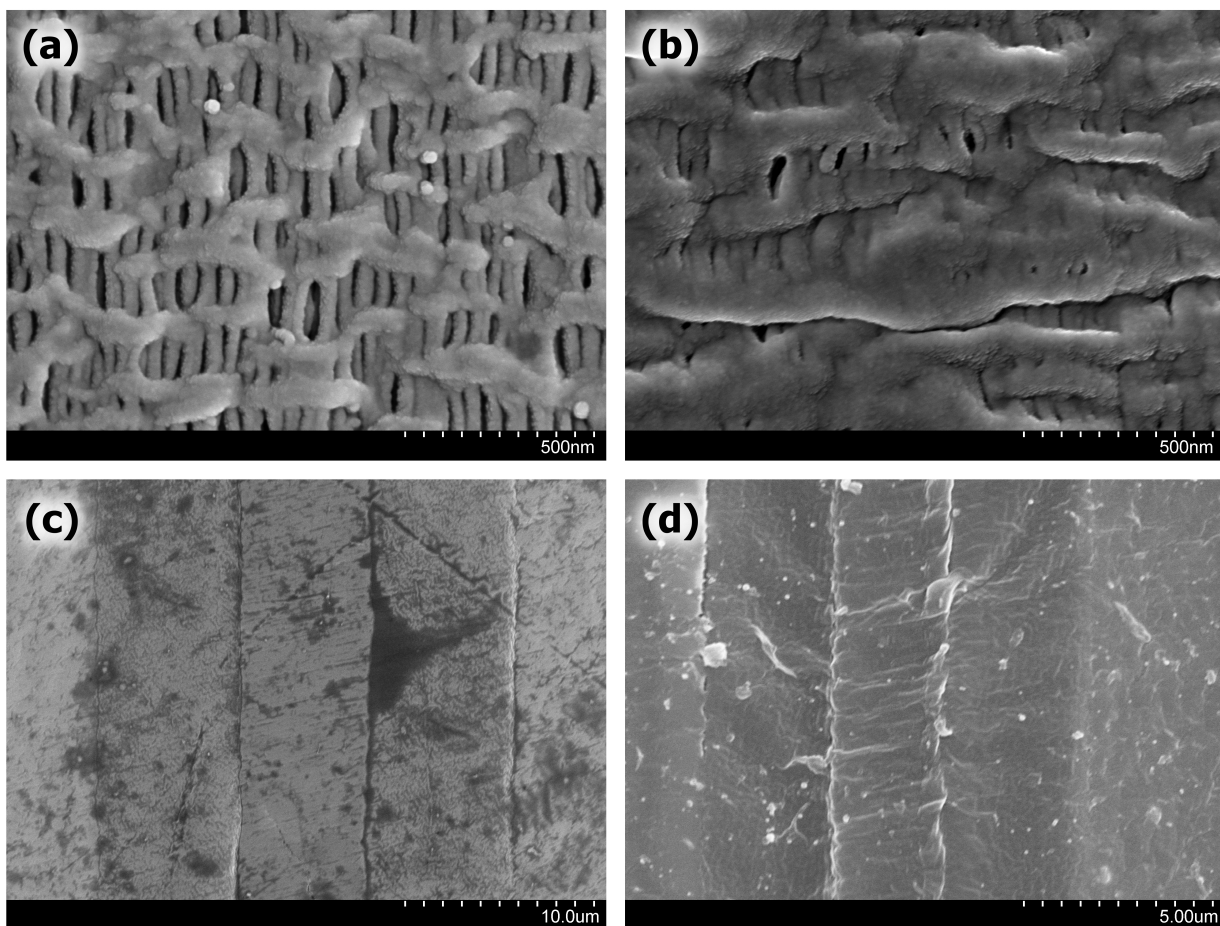


**Figure 2.14:** Scanning electron micrographs (SEM) of separator layers: (a) Surface SEM before compression, (b) Surface SEM after compression, (c) Cross-sectional SEM before compression and (d) Cross-sectional SEM after compression.

## 2.3 Jellyroll Characterization Using LVDT Deflection Sensor

In general, for universal testing machines, crosshead displacement readings are usually used for the cases when testing is done at low load levels and/or high elongations. However, if the load levels are higher and elongations are small, crosshead displacements are not accurate anymore, because crosshead displacement sensors are calibrated under "no-load" conditions. During a test with relatively higher load levels and small elongations, there are several potential sources of displacement errors such as crosshead and column deflections, grip or fixture deflections, compressibility of oil for servo-hydraulic machines and etc. For those cases, it is usually recommended to use compliance corrections, extensometers or linear variable differential transformers (LVDT) [107].

For compression testing of jellyroll layers, depending on the maximum desired load, crosshead readings can indicate an extra displacement of 0.5 to 1 *mm*, causing an error of 10-20 percent in the final stress-strain curves. Therefore, many of the previously reported experiments were repeated to get a more accurate stress-strain data using LVDT deflection sensor. All of the following experiments were conducted using an Instron 5985 universal testing machine with a 250 *kN* load cell. An LVDT 2601-043 sensor [108] (Fig. 2.15a) with a deflection range of  $\pm 15$  *mm* was attached to the machine to accurately measure specimen's deflection.

Before using the LVDT sensor for jellyroll characterization, a simple setup was used to compare the deflection data from testing machine's crosshead and LVDT. Based on the specifications of Instron 2601-043 deflection sensor, the maximum stroke is  $\pm 22$  *mm* while its linear stroke is only  $\pm 15$  *mm*. This means that for accurate measurements, the first and last 7 *mm* of total range of the sensor should not be used. For initial deflection comparison, the testing machine and LVDT was set up so that there was a gap between compression platens and the LVDT was in its fully extended position (Fig. 2.15b). Compression test



started with a rate of  $2 \text{ mm/min}$  and displacement was measured using both crosshead and LVDT sensors. Fig. 2.16a plots the deflections found from the two sensors and their difference over time. Crosshead deflection shows a perfectly linear variation throughout the test as expected based on the specified displacement rate. However, the LVDT readings are initially nonlinear and after about  $7 \text{ mm}$  of crosshead movement the two curves remain parallel for the rest of the test. This, complies with LVDT's specifications and confirms that for accurate results, the midrange of deflection sensor's stroke must be used. Force-deflection curve is also plotted in Fig. 2.16b. Since the compression platens are not in touch, the load cell essentially measures the LVDT's force over its travel. Since the maximum load is about  $5 \text{ N}$  when the sensor is fully retracted, it can be considered negligible compared to the maximum loads applied during jellyroll characterizations ( $\sim 100 \text{ kN}$ ).

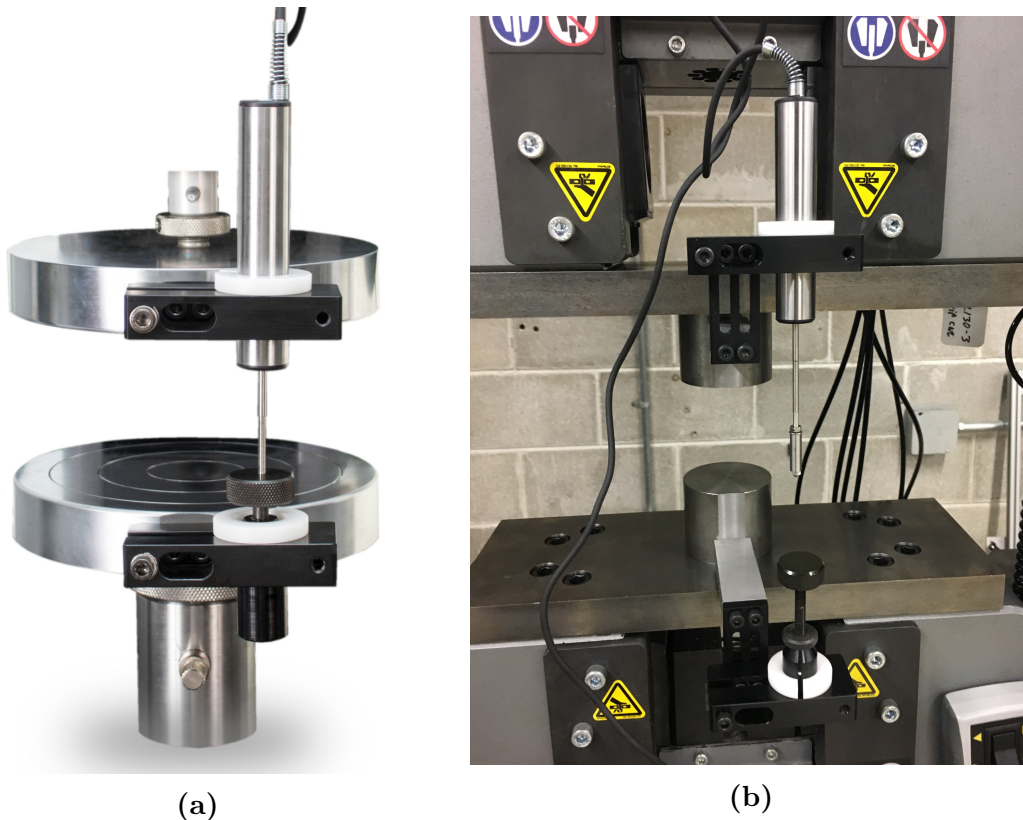


**Figure 2.15:** (a) Instron LVDT deflection sensor, model 2601-043 and (b) LVDT sensor installed on an Instron 5985 testing machine.

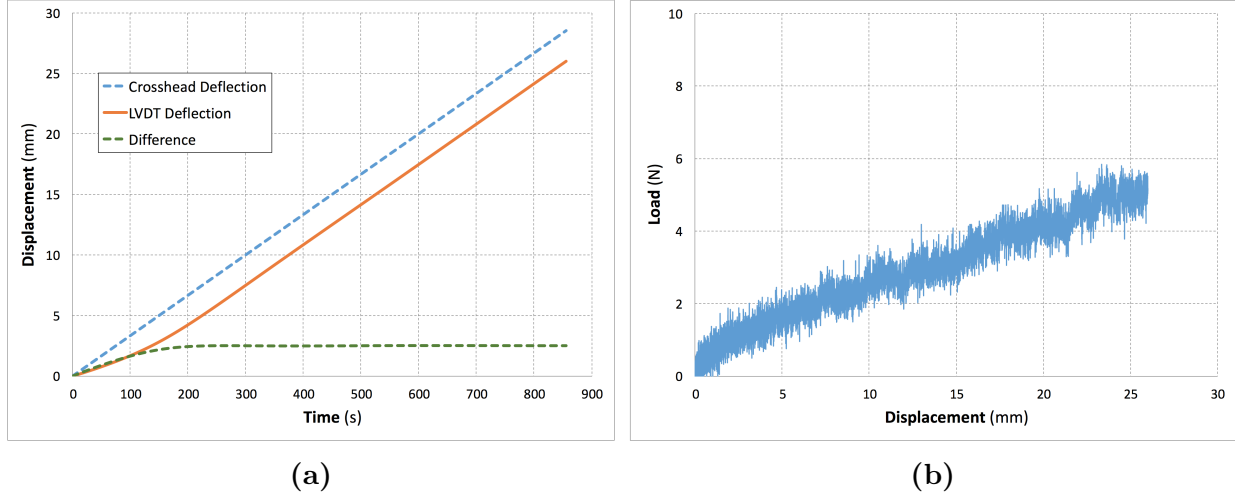


**Figure 2.16:** (a) Deflection comparison for crosshead and LVDT sensors and (b) Force caused by LVDT deflection.

### 2.3.1 Effects of Clamps and Sample Thickness

LVDT sensor eliminates many of the aforementioned errors for strain calculations caused by crosshead measurements since it directly measures sample's thickness change. Hence, there is no need to prepare a relatively thick sample in order to reduce strain measurement errors. To realize how sample thickness and presence of clamps change the calculated stress-strain curve, three coated copper samples were tested under compression. For the first sample 30 layers of coated copper layers were stacked and taped to a steel plate. The second sample was made by 50 layers (see Fig. 2.17a) while for sample 3, two aluminum clamps were used to stack 100 coated copper layers as shown in Fig. 2.17b.

All of the three samples were compressed at a rate of  $2 \text{ mm/min}$  using a  $21.6 \text{ mm}$ -wide steel bar (Fig. 2.18a). The measured load-displacement curve was converted to stress-strain relation. Comparison of the results (see Fig. 2.18b) showed negligible differences between the three stress-strain curves. The experiments also showed that failure load is inversely related to the sample thickness. This might be attributed to the fact that chances of slippage of layers are higher for thicker samples with more number of layers.

For the dry/wet compression tests on individual layers explained in the following sections,



stacks of 50 layers have been used for coated copper and aluminum layers. For separators, 100 layers were stacked on a steel plate because of their relatively smaller thickness.

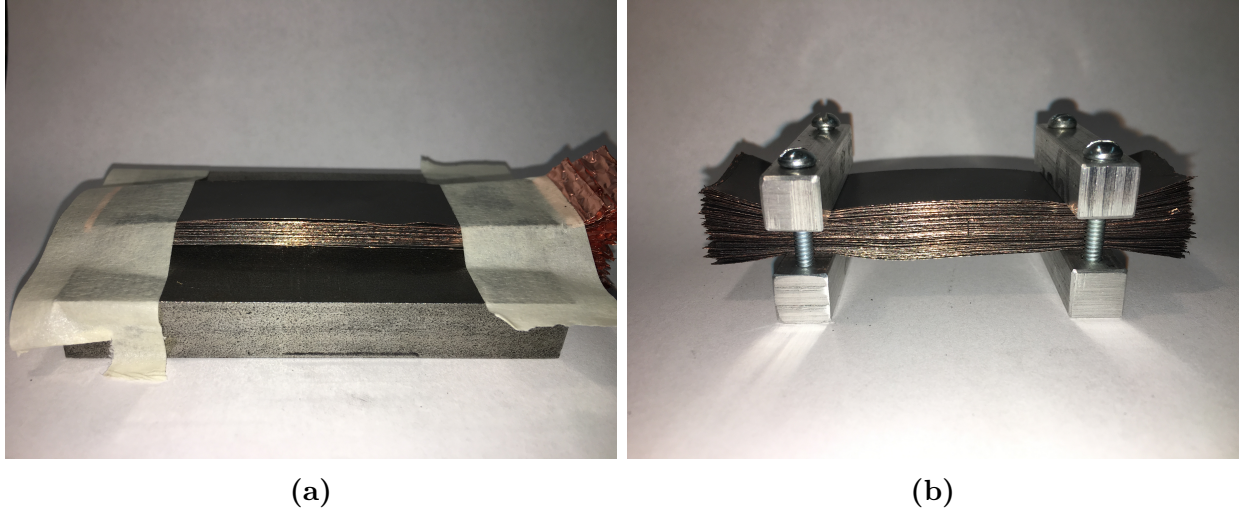


**Figure 2.17:** (a) Stack of 50 layers of coated copper layers taped on a steel plate and (b) Stack of 100 coated copper layers clamped on both ends.

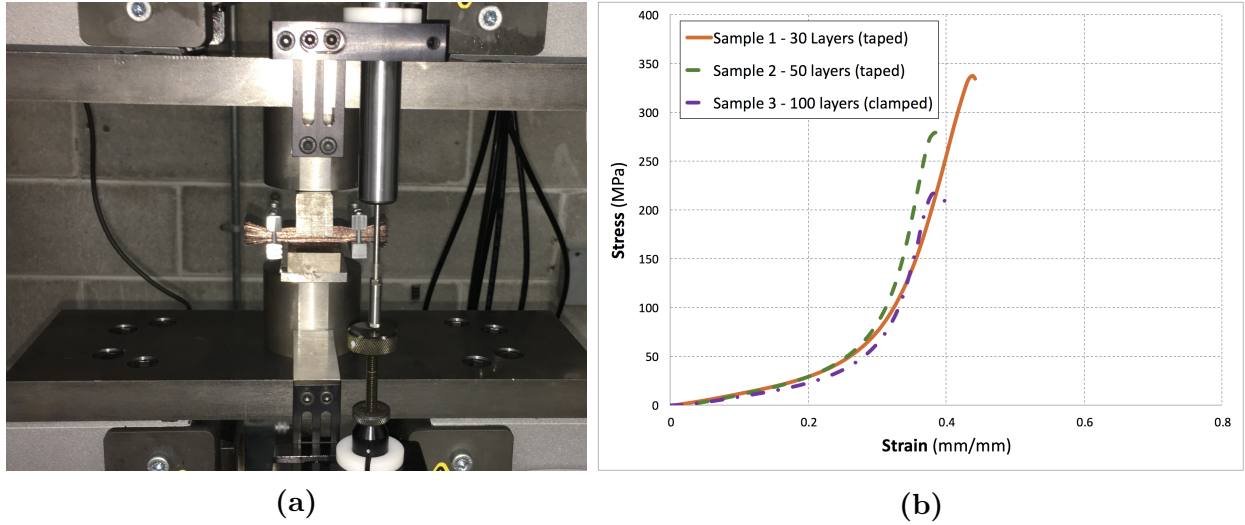


**Figure 2.18:** (a) A stack of coated copper layers being tested and (b) Stress-strain curves for coated copper samples with various number of layers.

### 2.3.2 Jellyroll Wet/Dry Compression Tests

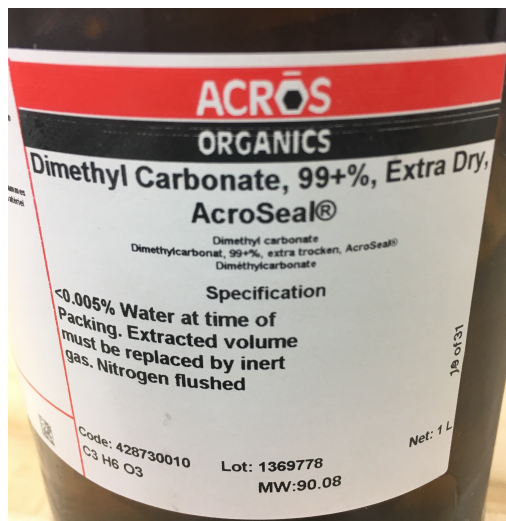
Homogenization of dry and wet jellyroll samples previously mentioned in Section 2.1.3 was repeated using Instron 5985 testing machine with a 250 *kN* load cell to achieve higher strain

levels and LVDT deflection sensor to get more accurate displacement measurements. Similar to the previous tests, samples were prepared by cutting jellyroll into about one-inch pieces. They were also cut in radial direction so they can be unrolled and flattened. From each sample, 40 jellyroll revolutions which consist of 40 coated copper, 80 separator and 40 coated aluminum layers were divided and stacked for compression tests. For saturated experiments, two samples were soaked in Dimethyl Carbonate (DMC) made by Acros Organics for 24 hours (Fig. 2.19a and b). DMC is an organic electrolyte solvent commonly used in lithium-ion batteries.

The samples were tested by placing them on the bottom compression platen while a 21.6 *mm*-wide steel bar was used to apply compressive load as shown in Fig. 2.20a. Two dry and two saturated jellyrolls were tested at a displacement rate of 2 *mm/min*. Fig. 2.20b shows one of the crushed jellyrolls. Measured displacements from LVDT sensor and measured forces from the load cell were converted to a homogenized stress-strain relation for the jellyroll (see Fig. 2.21) which is used as the jellyroll's constitutive model in finite element simulations. Similar to the results found from previous experiments without using LVDT, existence of DMC solvent has negligible effects on jellyroll's stress-strain curve. The only difference is that the experiments using LVDT shows a slightly higher stiffness for saturated samples while in previous tests, dry jellyroll seemed to have higher stiffness (Fig. 2.11d).

### 2.3.3 Strain-Rate Dependence

Although all of the previous jellyroll compression tests were conducted at a rate of 1 and 2 *mm/min*, the resultant stress-strain curves are supposed to be used to simulate high-rate impact on lithium-ion batteries. Therefore, a new set of experiments was performed at higher displacement rates in order to study how strain-rate affects the jellyroll's load carrying capacity. Similar to the experiments reported in the previous section, 40 revolution of anode, cathode and separator layers were crushed at various displacement rates. A total of seven samples were tested with a cross-head speed of 2, 4, 8, 16, 32, 64 and 128 *mm/min*.



(a)

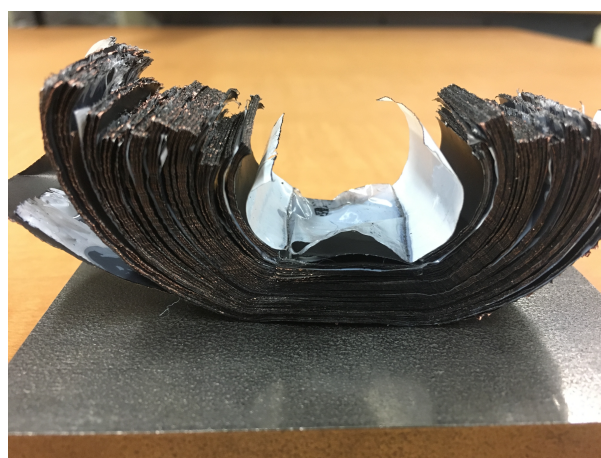


(b)

**Figure 2.19:** (a) The DMC solvent used for jellyroll saturation and (b) Jellyroll samples being soaked in the solvent.



(a)



(b)

**Figure 2.20:** (a) A jellyroll sample being tested under compression and (b) Crushed jellyroll sample.

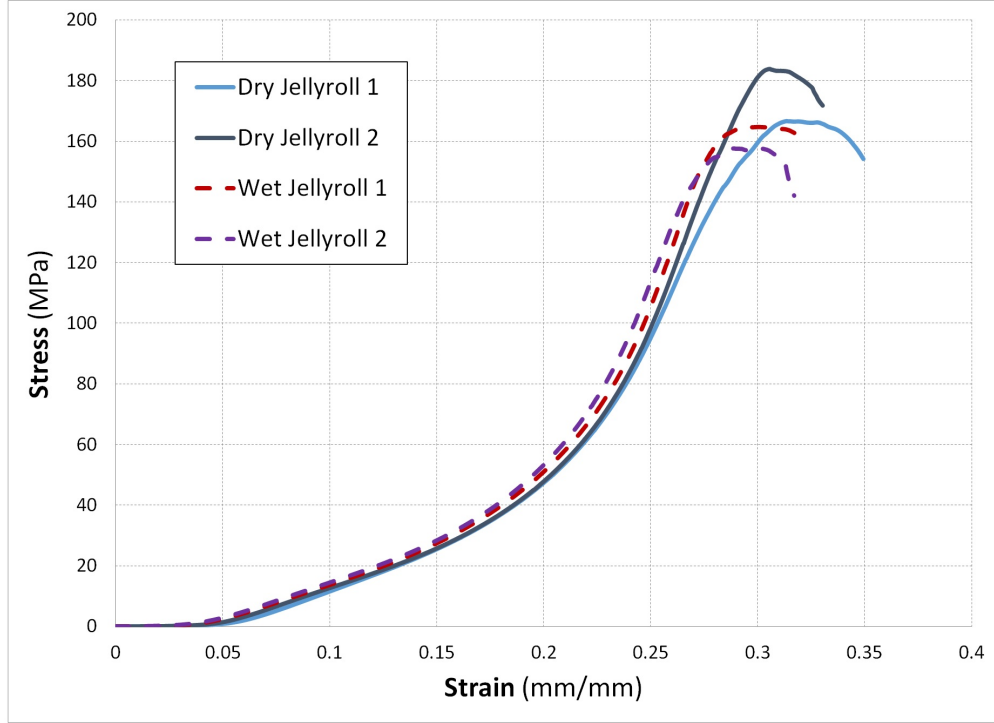


**Figure 2.21:** Stress-strain curves for flattened jellyroll samples under dry and saturated conditions.

Jellyroll was cut to 25 *mm* wide samples and the test was performed using a 21.6 *mm*-wide steel bar for compression. All of the tests were conducted on an Instron 5985 testing machine with a 250 *kN* load cell (fig. 2.22a). The measured load-displacement values were converted to engineering stress-strain curves as depicted in Fig. 2.22b. Comparison of the curves for different strain-rates shows that the crush speed does not significantly affect the calculated stress-strain relationship for strain values below 0.2. For larger strains, it can be observed that the slope of the curves increases with displacement rates up to a speed of 8 *mm/min* and decreases for higher strain rates. Overall, at higher strain values, there is a stress difference of  $\pm 15\%$ . For impact problems, the absorbed energy is directly related to the strain energy density of the material and comparing the area under the curves shows a difference of about 13% between the strain energies at lowest and highest displacement rates i.e. 2 and 128 *mm/min*. Although impacts usually occur at much higher rates, these results show that the previous flattened compression tests conducted at relatively slow rates of 2 *mm/min* can be still used for impact simulations with a reasonable error.



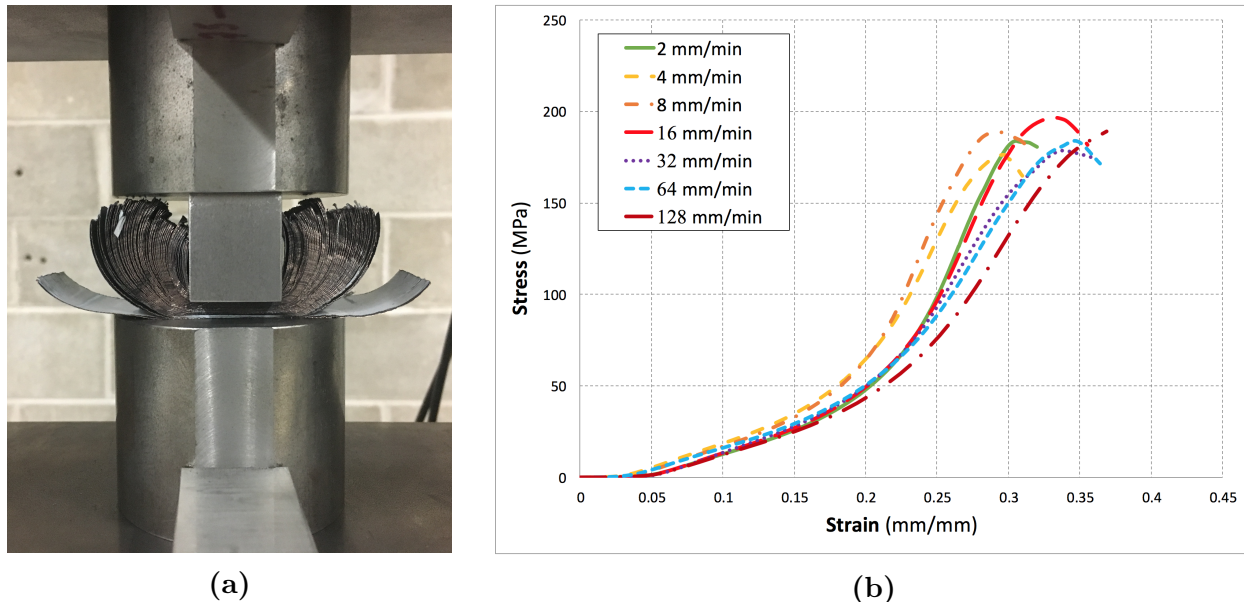


**Figure 2.22:** (a) A jellyroll sample being tested under compression and (b) Stress-strain curves for jellyroll compression tests at various displacement rates.

### 2.3.4 Characterization of Individual Jellyroll layers (Wet/Dry)

Mechanical properties of individual jellyroll layers i.e. anode, cathode and separators were characterized previously (Section 2.2) using compression experiments with cross-head displacements. In this section a new set of experiments is reported with more accurate data recorded by LVDT deflection sensor. Also, effects of DMC electrolyte solvent on individual layers' stress-strain curves have been studied.

Section 2.3.1 showed that changing the sample's number of layers from 30 layers to 100 layers does not influence the resulting stress-strain curve. Therefore, stacks of 50 layers for anode and cathode and 100 layers for separators were used for wet and dry characterization of individual jellyroll components. Each layer was carefully cut using an X-ACTO knife with a #2 blade. 20.6 mm-wide layers of identical materials were stacked, aligned and clamped at both ends as depicted in Fig. 2.23. For saturated experiments, similar to jellyroll tests (Fig. 2.19), one sample of each material was soaked in DMC solvent for 24 hours. During the tests, the samples were placed and taped on a steel plate to minimize layers' slippage as illustrated in Fig. 2.24a for a coated aluminum sample. Fig. 2.24b depicts how one of

the coated aluminum samples is deformed and Fig. 2.25 compares the resulting stress-strain curves for dry and wet samples. DMC solvent does not affect coated aluminum properties under small strain values. However, when the layers' through-the-thickness strain reaches a value of about 0.24 with a stress level of 250 *MPa*, there seems to be a failure in saturated samples while the dry layers can still carry more loads.

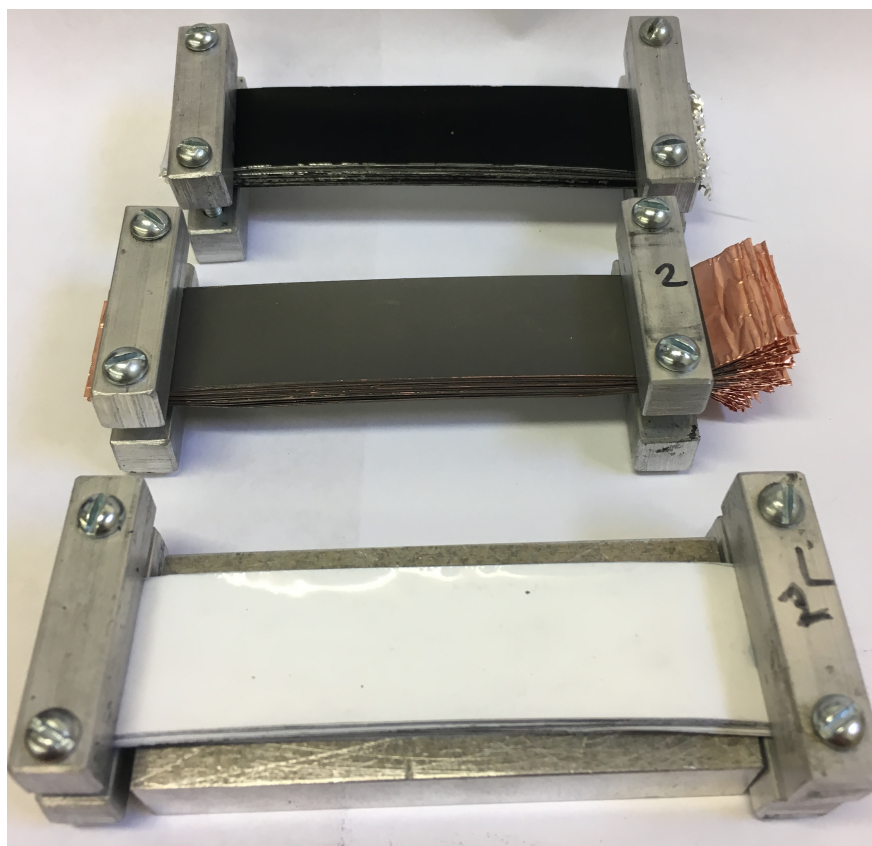
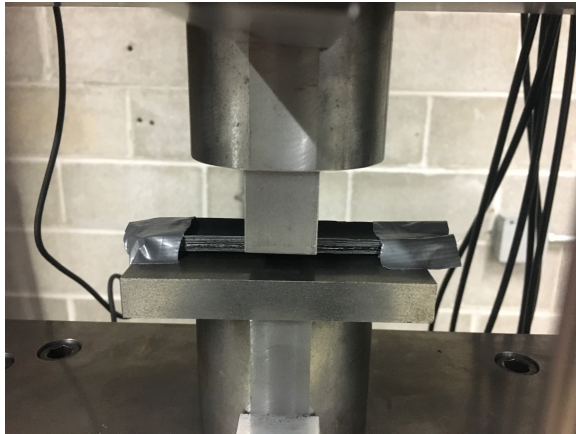
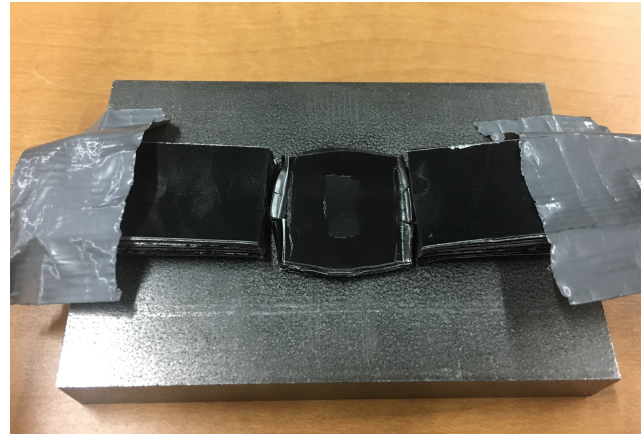


**Figure 2.23:** Stacks of coated aluminum (top), coated copper (middle) and separator layers (bottom) clamped at both ends.

Coated copper layers were tested in an identical process under dry and wet conditions (Fig. 2.26a). Crushed layers and the resulting stress-strain curves are depicted in Fig. 2.26b and 2.27. The curves for dry and wet layers are identical up to a strain level of 0.24 after which the wet sample carries about 30 percent more stress compared to the dry sample at similar strain levels. The other difference is the failure stress which is about 270 *MPa* for dry sample while in the presence of DMC, failure occurs when the stress reaches 190 *MPa*. Failure strain is also smaller for wet sample and is about 0.37 compared to 0.41 for the dry



(a)



(b)

**Figure 2.24:** (a) A stack of 50 coated aluminum layers being tested under compression and (b) Deformed coated aluminum sample.

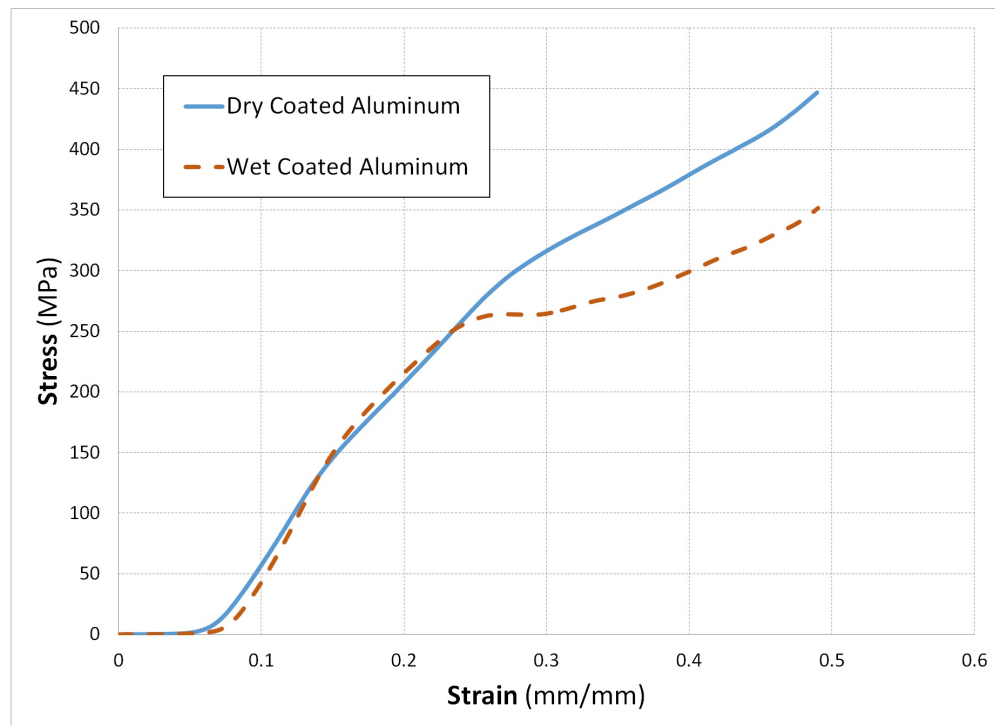


**Figure 2.25:** Stress-strain curves for coated aluminum samples under dry and saturated conditions.

test.

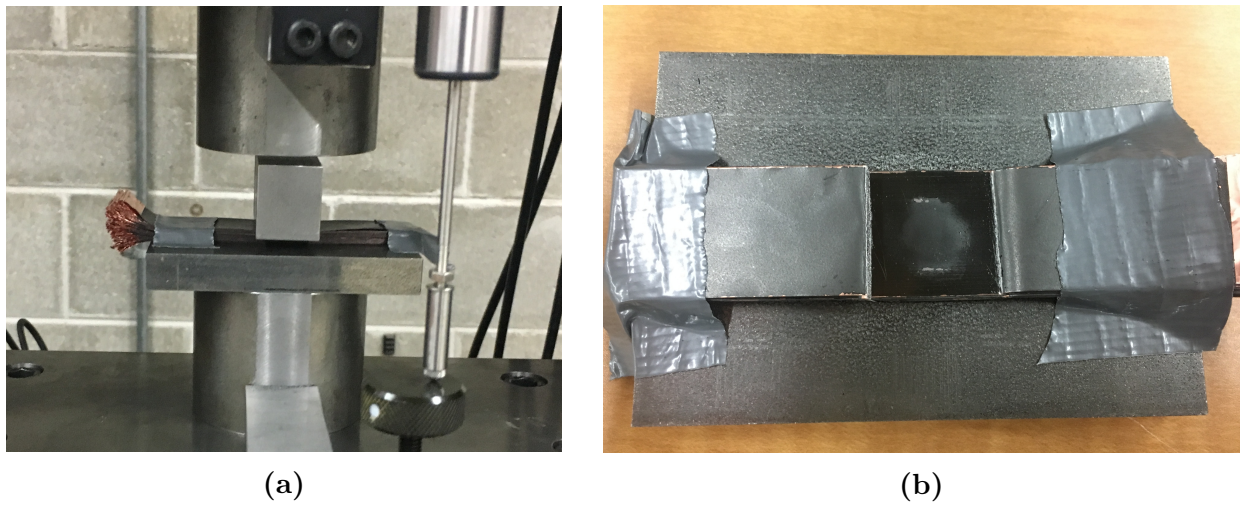


**Figure 2.26:** (a) A stack of 50 coated copper layers being tested under compression and (b) Deformed coated copper sample.

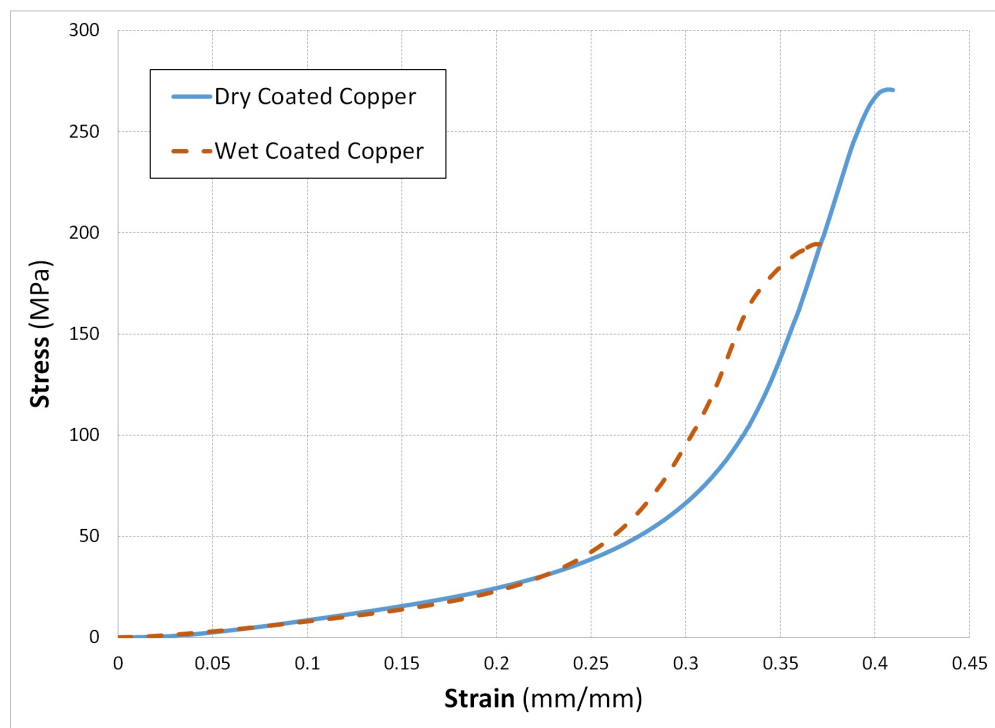


**Figure 2.27:** Stress-strain curves for coated copper samples under dry and saturated conditions.

Because of their relatively smaller thickness, characterization of separator layers was performed on stacks of 100 layers. Sample width and compression bar dimensions were



identical to anode and cathode layers' experiments. Fig. 2.28a shows one the samples under compression while the displacement is being measured using LVDT sensor. Compressed to a strain level of 0.9, separator layers became transparent after crush (Fig. 2.28b). The stress-strain curves plotted on Fig. 2.29 illustrate that the difference between separator's mechanical properties under wet and dry conditions is significantly greater than anode and cathode layers. Dry separator layers tend to have a nonlinear stress-strain behavior until they fail at a stress of just below  $180\text{ MPa}$  and about 0.58 strain level. However, when DMC solvent is present, initially the curve has a higher slope before there seems to be a failure when the stress reaches about  $40\text{ MPa}$ .

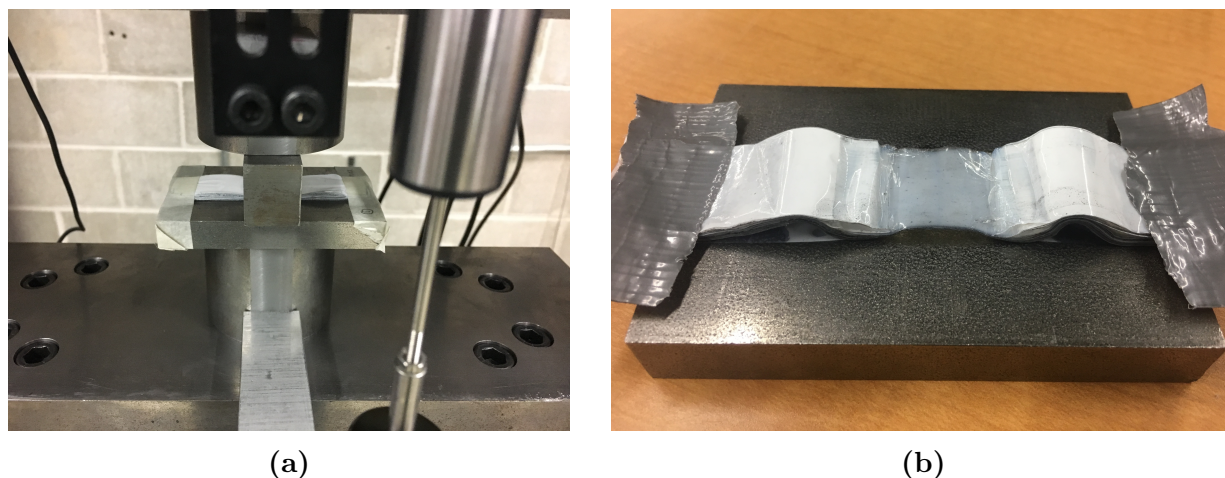


**Figure 2.28:** (a) A stack of 100 separator layers being tested under compression and (b) Deformed separator sample.

Overall, when all three of the jellyroll layers are compared under compression, it seems that the coated aluminum layers have the highest stiffness, while the separator layers tend to be more flexible under transverse compressive forces. When DMC solvent is present, all of the three types of jellyroll layers, i.e. anode, cathode and separator, fail at lower stress values compared to dry conditions. Separator layers and coated aluminum layers have an overall higher stiffness when there is no electrolyte solvent. However, for coated copper layers, DMC solvent seems to inversely affect the mechanical properties and there is a higher stiffness for saturated samples before failure.

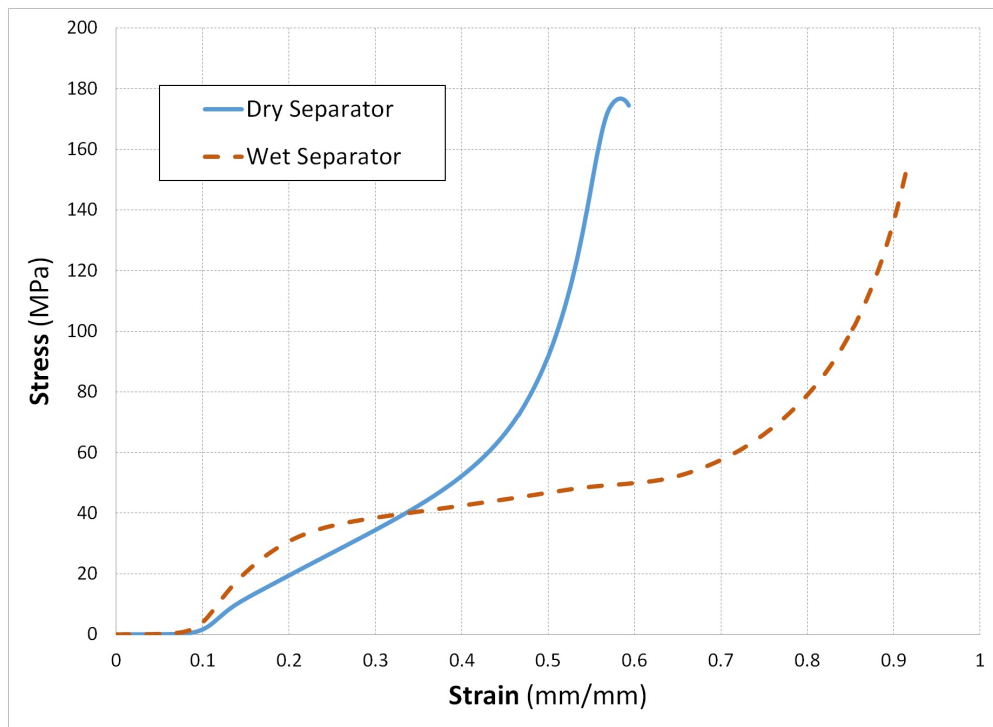


**Figure 2.29:** Stress-strain curves for separator samples under dry and saturated conditions.

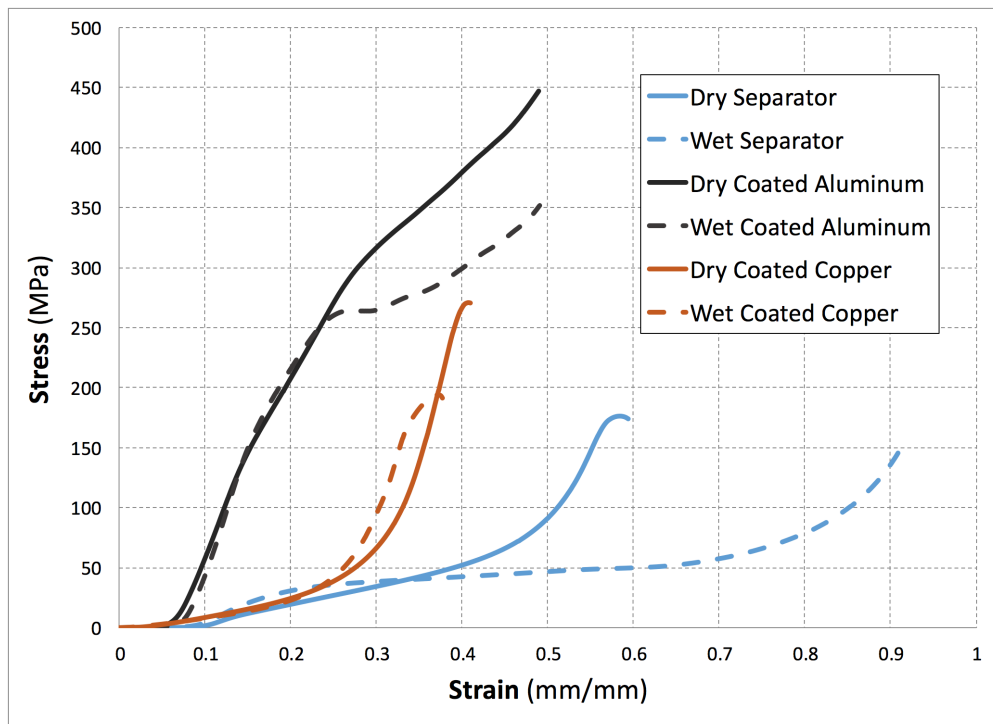


**Figure 2.30:** Stress-strain curves for jellyroll components under dry and saturated conditions.

## 2.4 Study of Separator Pore Size under Compression

One of the safety features of lithium-ion batteries is that under high temperatures the polyethylene (PE) layer of a trilayered separator melts and stops the transport of ions by closing the pores of the separator. This provision, effectively shuts the cell down and minimizes the heat generation inside the cell. It would also be helpful to know how the pore size changes when the separator is under compression. In order to study this, four separator samples were prepared to perform additional compression tests. Each sample consisted of a stack of 100 separator layers. 20.6 *mm*-wide samples were attached to a steel plate depicted in Fig. 2.31a. Samples were tested under compression using an Instron 5985 testing machine at a rate of 2 *mm/min* (see Fig. 2.31b). A 21.6 *mm*-wide steel bar was used to apply compression. Displacement was measured using an LVDT deflection sensor. The first sample was compressed up to a load of 15 *kN*. For sample 2 and 3, a maximum force of 30 *kN* and 45 *kN* was applied respectively. For sample 4, the test was continued until reaching failure at a load of 56 *kN*.

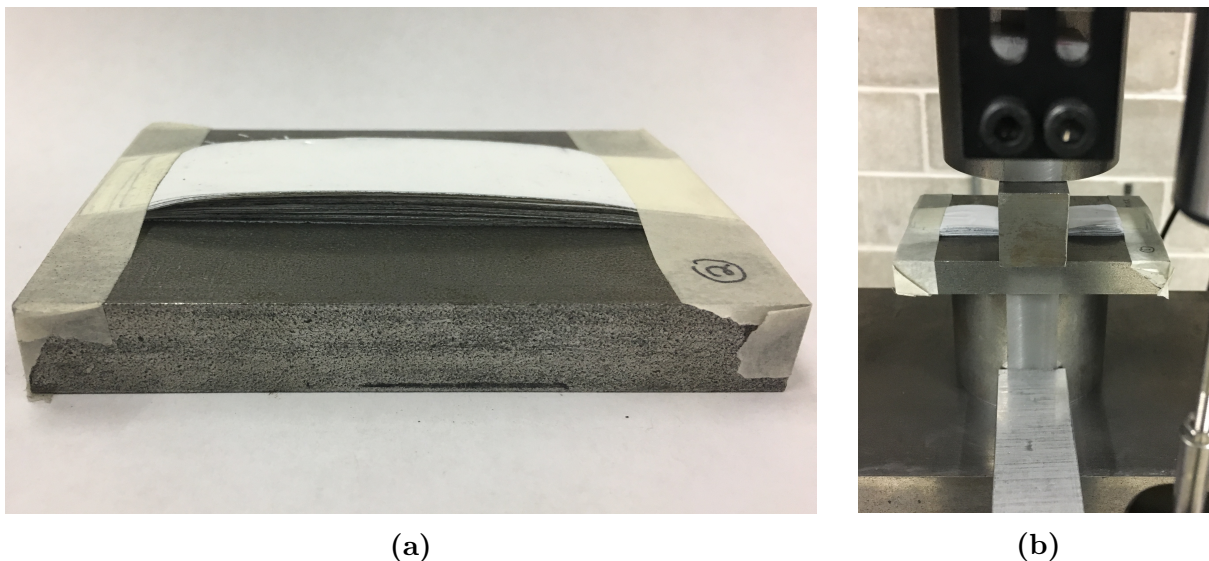


**Figure 2.31:** (a) Stack of 100 separator layers before compression and (b) Compression test of separator sample.

Stress-strain curves for the four samples are plotted in Fig. 2.32. As expected, all of the

curves are almost coincident. The only difference is that for sample 1, 2 and 3 the maximum stress does not reach the failure stress since the tests were stopped at lower load levels. SEM images of separator layers before test and after being crushed under various load levels are compared in Fig. 2.33. Fig. 2.33a shows a trilayered separator layer before applying any load. Fig. 2.33b to 2.33e are the SEM images for samples crushed up to 15 *kN*, 30 *kN*, 45 *kN* and 56 *kN* respectively. Comparing the SEM images illustrates that the number of pores decreases with higher compressive loads. There is also a considerable drop in size of the remaining pores. In order to do a quantitative study on the pore sizes, 10 pores were randomly selected from each SEM image. Pores were assumed to be ellipse-shaped. The major and minor axes of each pore were measured to estimate the area (plotted in Fig. 2.34). Average pore size was calculated for the 10 pores of each sample and a curve fitted through the average pore sizes (also plotted in Fig. 2.34). Calculations show that the pore size roughly follows a linear decay with an increase in compressive load.

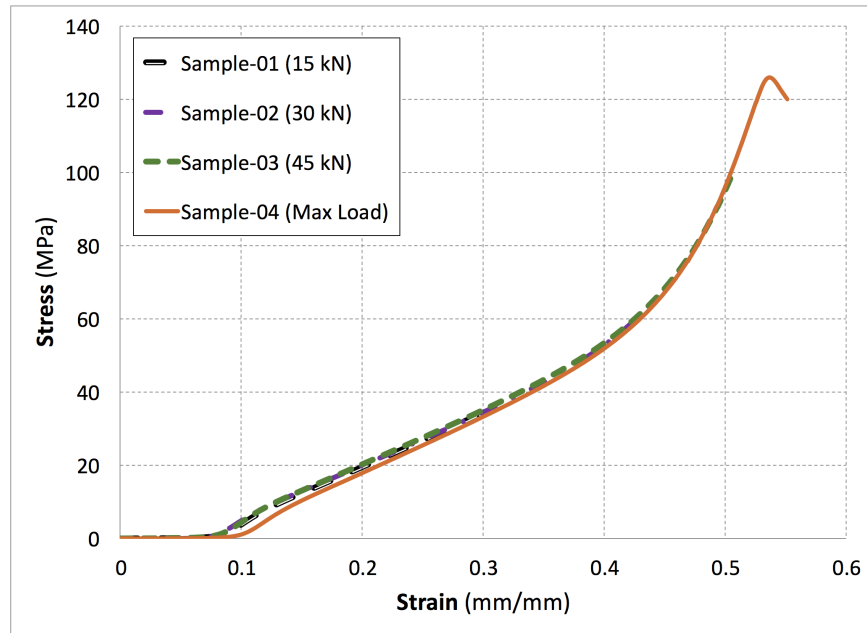
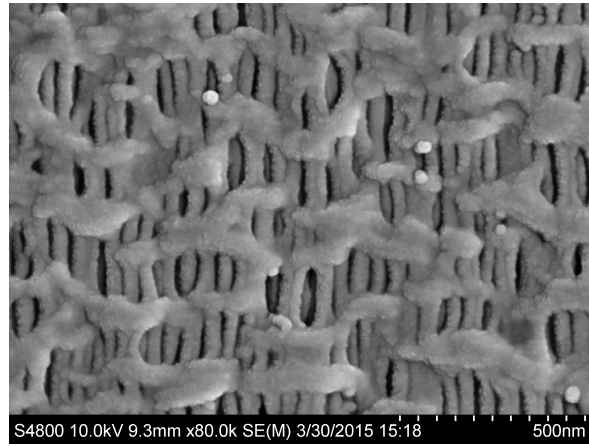
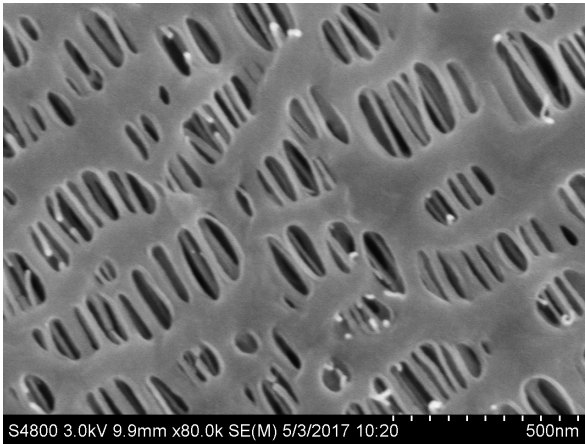


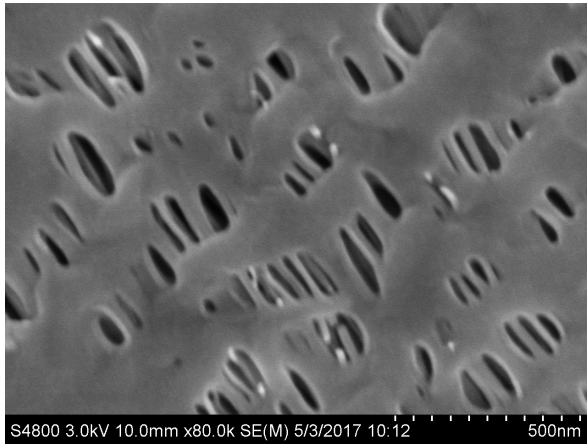
**Figure 2.32:** Stress-strain curve found from compression test of separator samples.



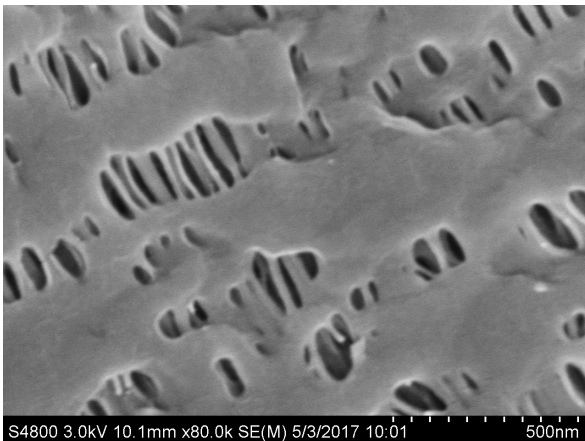
(a)



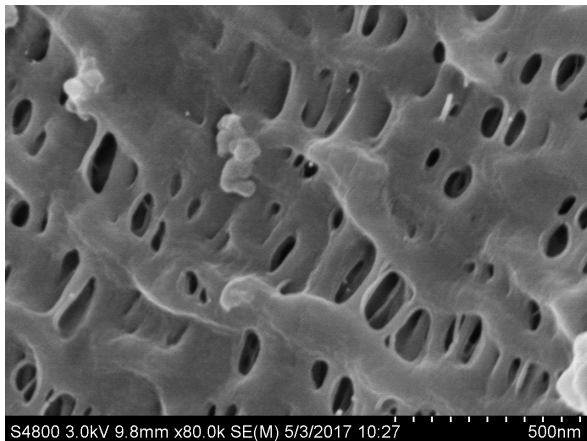
(b)



(c)



(d)



(e)

**Figure 2.33:** SEM images of separator layers: (a) Separator layer before compression, (b)-(e) Separator after compression tests with a crush load of 15 *kN*, 30 *kN*, 45 *kN* and 56 *kN*, respectively.

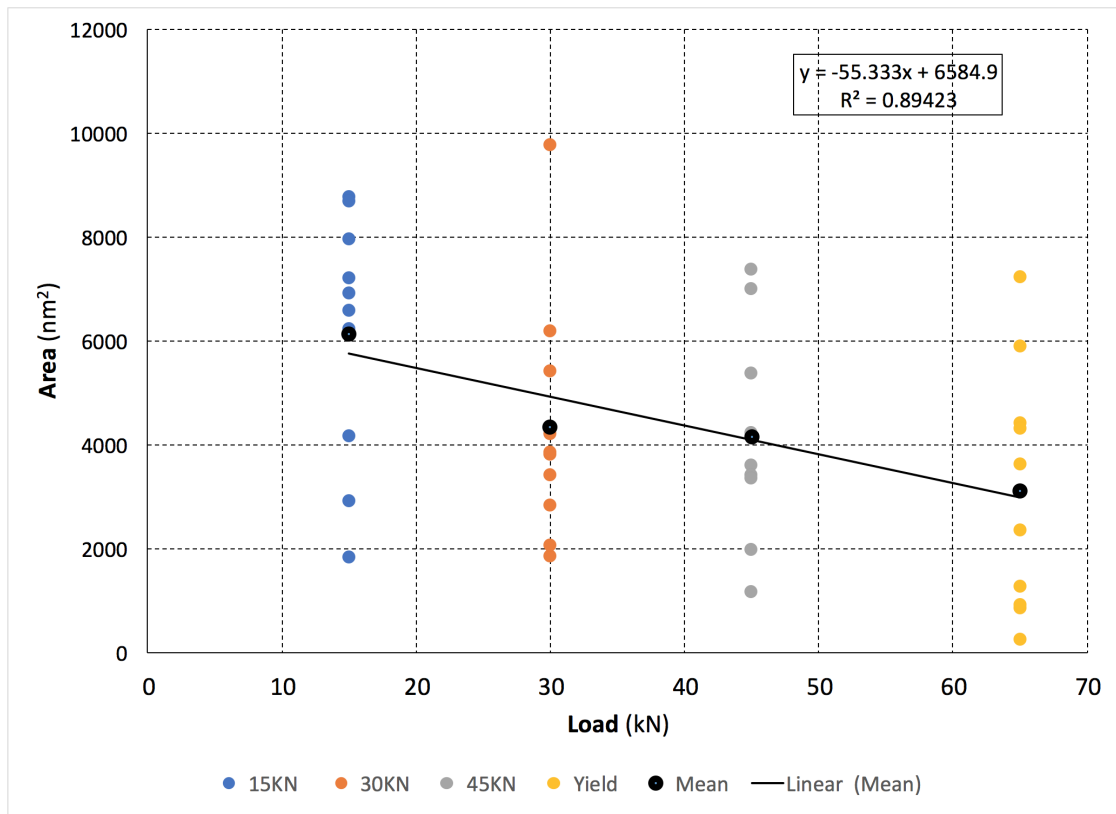


**Figure 2.34:** Variation of separator pore size with compressive load magnitude.

---

## Chapter 3

### Cell Level: Experiments

#### 3.1 Drop Tests

##### 3.1.1 Experimental Procedure and Setup

A number of standards have been developed and found in the literature to assess the safety aspects of lithium-ion battery cells and packs. These standards typically suggest different experiments on batteries that can be categorized as electrical, mechanical or thermal experiments. Crushing, drop test and impact tests are some examples of mechanical tests found in various standards [1, 109, 110]. For example, impact test is used to determine a cell's ability to withstand a specified impact applied to a cylindrical steel rod placed across the battery cell. Most of these experiments are qualitative tests; that is, to pass the tests, the cell or pack may not explode or ignite. However, in this study, dry cells were used instead of cells with electrolyte and no ignition or explosion was possible. The goal was to validate the finite element model, which will be used for impact simulations. Therefore, in this study, in addition to impact test using a steel rod, impact between two rigid plates was also performed on the cells. A 2.8-*m* drop test apparatus (see Fig. 3.1) was designed and manufactured for this purpose consisting of a bottom steel plate and a moving drop cart capable of adding additional weight. The drop cart was guided in the drop tower using eight roller bearings that ensured straight movement with minimum friction between the cart and the guide bars. A manual winch was used to lift the drop cart to the desired height before release. A high-speed camera was used to capture the impact scene.





**Figure 3.1:** Custom-designed drop test apparatus: (a) CAD model and (b) actual drop test.



### 3.1.2 Lateral Impact Between Two Flat Plates

Because of the asymmetric shape and location of the anode and cathode cell terminals, two impact configurations were investigated: (1) horizontal and (2) vertical (see Table 3.1). Cell impact was studied using two different drop carts weighing 11.34 *kg* and 22.68 *kg*. The theoretical impact velocity was calculated using the drop height assuming negligible friction and was found to be 7.4 *m/s*. In order to measure the actual plate's impact velocity, a set of markers was placed on the drop tower wall in front of a high-speed camera. By measuring the distance the drop cart moves between two subsequent frames of the recorded movie, the impact velocity of the drop cart was found to be equal to 7.0 *m/s*. Fig. 3.2 depicts three frames of a cell impact with horizontal terminal orientation: before impact, during impact and after impact. Also, a comparison of undeformed and crushed cells is presented in Fig. 3.3 and Fig. 3.4 for horizontal and vertical terminals orientation respectively. Various types of battery failures such as electrolyte leakage, short circuiting or activation of a permanent disabling mechanism are likely to occur due to an impact. But the most critical one would be the short circuit between electrodes that may cause a thermal runaway. The cells being dry, it was impossible to measure the voltage and temperature in order to track the internal short circuits and temperature increases. However, it is always a possibility that the terminals will touch causing an external short circuit due to severe deformation especially for the case of vertical orientation (Fig. 3.4).

**Table 3.1:** Lateral impact test configurations: cell orientation and drop mass.

Sample orientation		Drop mass ( <i>kg</i> )
Sample 1	Terminals aligned vertically	11.34
Sample 2		22.68
Sample 3	Terminals aligned horizontally	11.34
Sample 4		22.68

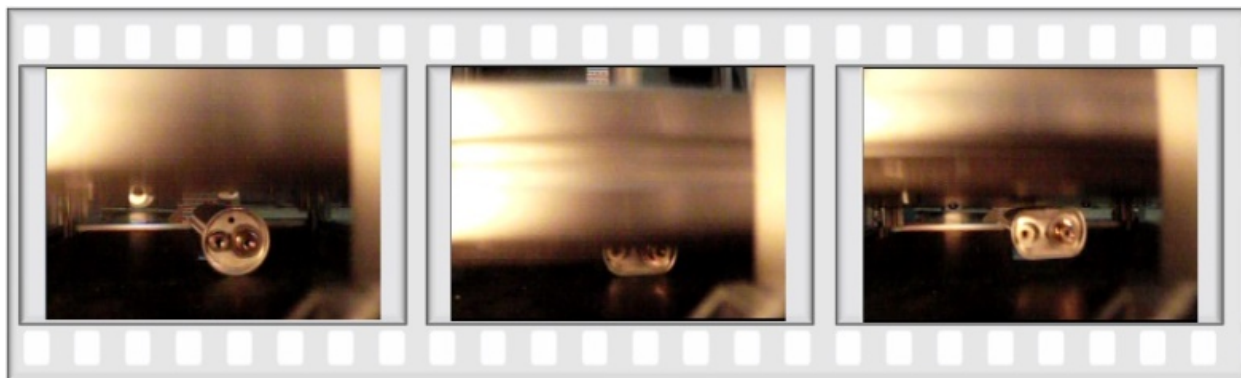


**Figure 3.2:** Lateral impact test (high-speed camera footage).



(a)



(b)

**Figure 3.3:** Cylindrical cell before/and after impact, 11.34 *kg* drop weight, horizontal orientation.

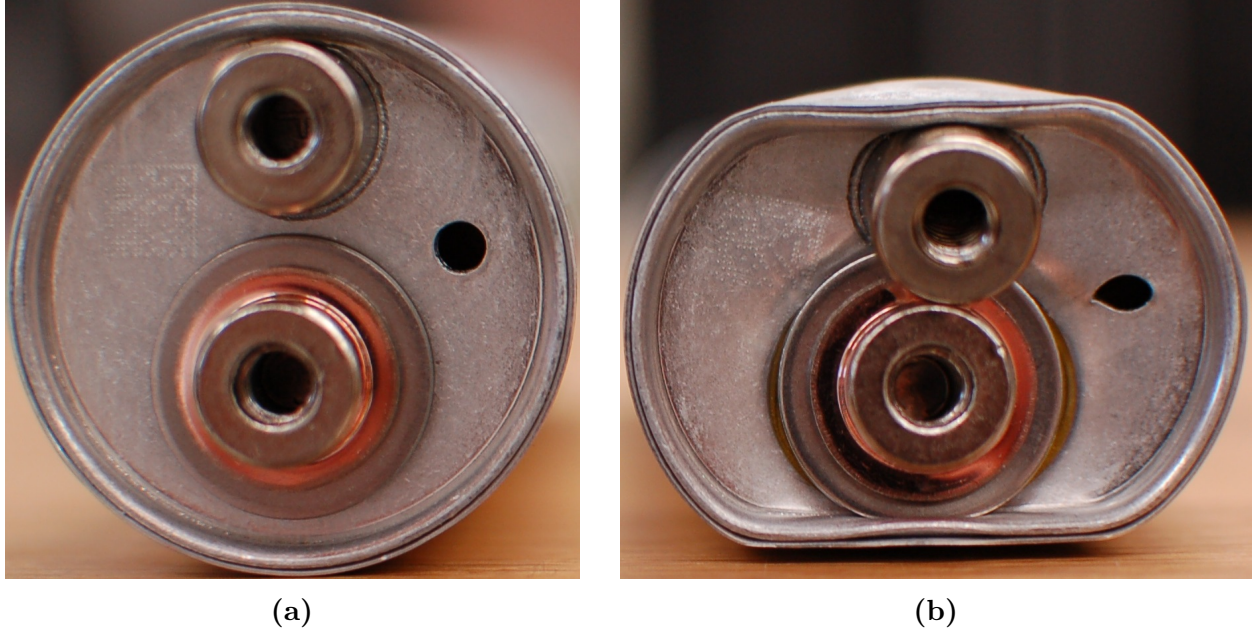


**Figure 3.4:** Cylindrical cell before/and after impact, 11.34 *kg* drop weight, vertical orientation.

### 3.1.3 Lateral Impact Using a Rigid Bar

A second set of experiments was planned and conducted based on the UN DOT 38.3 [110] standard which requires a 15.8 *mm* rigid rod to be placed across the center of battery cell (Fig. 3.5) and a 9.1 *kg* Impact weight to be dropped from a height of  $61 \pm 2.5$  *cm*. The aforementioned drop test apparatus was used with a few modifications. A simple mechanism was implemented to prevent a secondary impact after the rebound of the drop cart during the first impact. Furthermore, Vibra-Metrics 1018 accelerometers were used to measure the acceleration of the drop cart and record impact data during the experiments. The sensors have a 500 g amplitude range and 5000 g shock limit. Two sensors were mounted on top of the drop cart for additional accuracy and LabVIEW was used as the data acquisition software (Fig. 3.6). The experiments used dry and uncharged Johnson Controls 6P cells and were conducted in accordance with the standard and modified for investigation of short circuit occurrence caused by mechanical deformations. Thus, additional experiments were conducted at an increased height of 2.76 *m* and weights of 9.07 *kg* and 14.15 *kg*.

Table 3.2 lists the three impact weight and height configurations. Sample A were tested

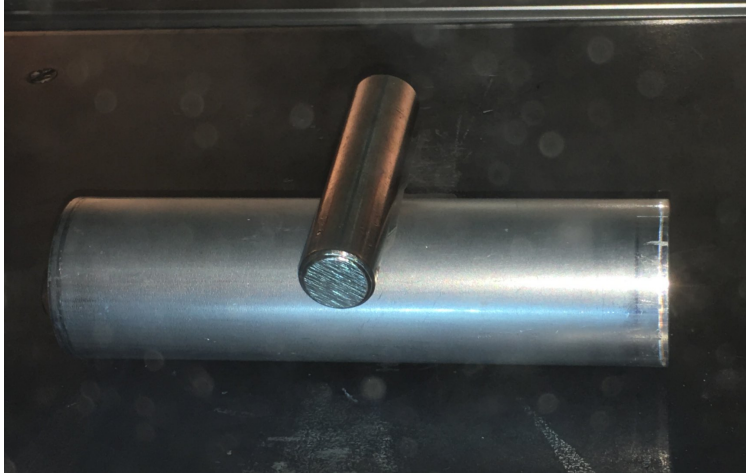
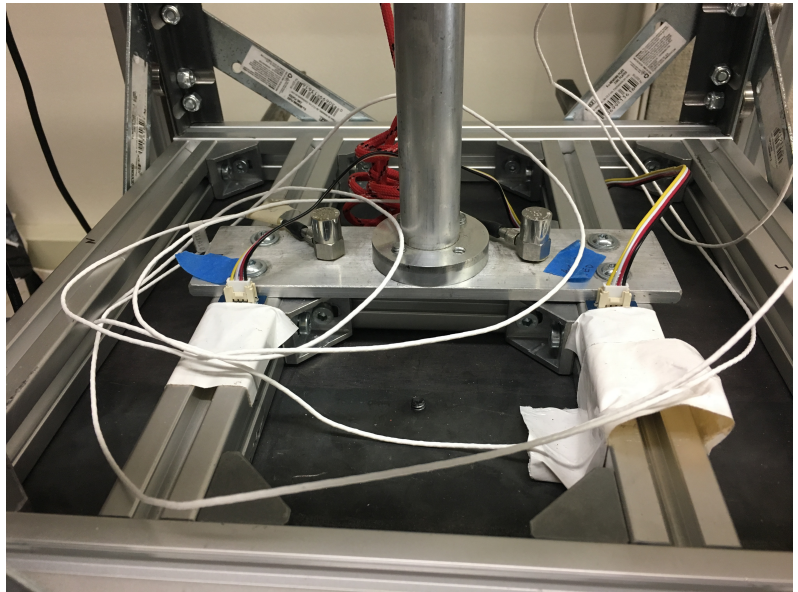


**Figure 3.5:** Steel rod placed across the center of a cell based on UN DOT 38.3 standard.



(a)



(b)

**Figure 3.6:** (a) A Vibra-Metrics 1018 sensor (Credit: mistrasgroup.com), (b) Accelerometers installed on the drop cart.

**Table 3.2:** Test configurations for lateral impact by a rigid bar.

	Drop height ( <i>m</i> )	Drop mass ( <i>kg</i> )
Sample A	0.635	9.07
Sample B	2.76	9.07
Sample C	2.76	14.15





**Figure 3.7:** Deformed cells after impact by a rigid bar.

under UN DOT 38.3 [110] requirements i.e. drop mass of  $9.07\text{ kg}$  and drop height of  $0.635\text{ m}$ . For sample B the same weight was dropped from a height of  $2.76\text{ m}$  and sample C was tested with an increased drop mass of  $14.15\text{ kg}$  and the maximum height. For all of the experiments, terminals were oriented horizontally as shown in Fig. 3.7. For comparison purpose, the maximum indentation caused by impact was measured at the middle of the cell (Fig. 3.8) and is listed in Table 3.3. Sample A shows a minimum indentation of  $7.05\text{ mm}$  while as expected, the deformation is the highest ( $13.74\text{ mm}$ ) for sample C with maximum drop height and weight.

The acceleration data, recorded by the two sensors attached to the drop cart is illustrated in Fig. 3.9 for sample A. Acceleration change over time for all of the tests showed three different regimes: at the beginning of the tests, there were some fluctuations because of the release mechanism; the second phase showed a constant acceleration during drop and finally, there was a very high acceleration jump when the cart impacted the steel rod. Using the acceleration data, drop time was recorded for each experiment and an average acceleration was calculated based on the corresponding drop height. Measured drop times and calculated

accelerations are listed in Table 3.4. The calculated accelerations are 15-24 percent less than the standard gravity (g) which is likely to be a result of friction and air resistance of the drop test enclosure.

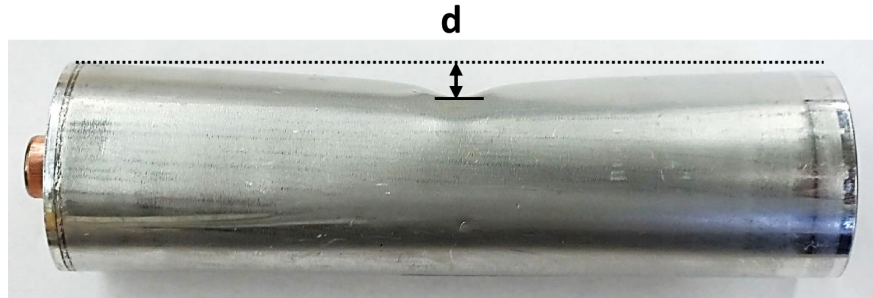


**Figure 3.8:** A deformed cell after impact by a rigid bar.

**Table 3.3:** Cell indentation for various impact configurations.

	Indentation, $d$ ( $mm$ )
Sample A	7.05
Sample B	11.59
Sample C	13.74

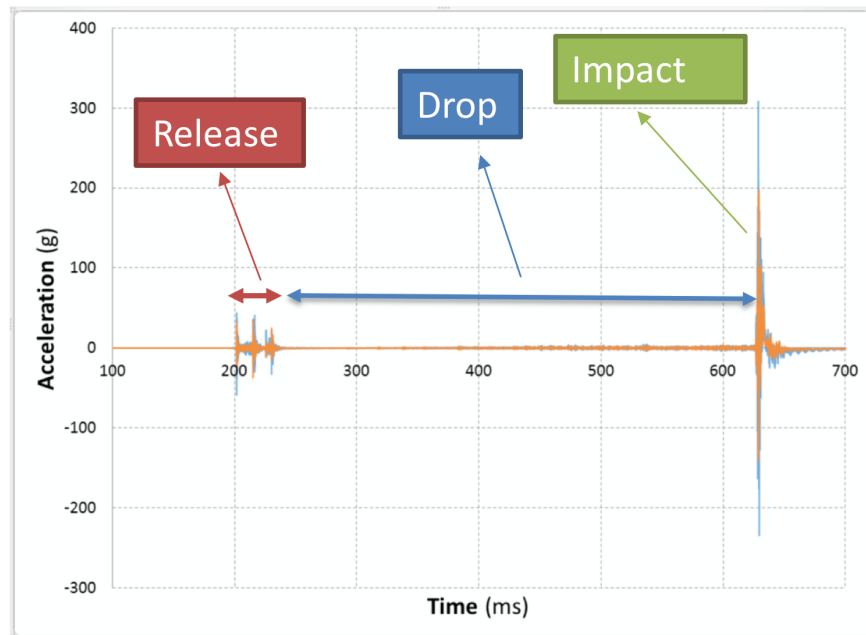


**Figure 3.9:** Recorded acceleration data for sample A.

**Table 3.4:** Drop time measured by accelerometers and corresponding average accelerations.

	Drop height ( <i>m</i> )	Drop time ( <i>ms</i> )	Acceleration ( <i>m/s</i> <sup>2</sup> )
Sample A	0.635	390	8.35 (.85g)
Sample B	11.59	860	7.46 (.76g)
Sample C	13.74	840	7.82 (.80g)

## 3.2 Quasi-Static Compression Experiments

In order to check and realize if any of the previous impact tests by a rigid bar led to an internal short circuit, a digital multimeter was used to measure resistance between the two terminals of each cell. It was assumed that in case of a separator failure, anode and cathode electrodes will be in contact, leading to small or zero resistance readings. All of the previous crushed cells i.e. samples A, B and C showed overload resistance values, implying no electrode contact and short circuit occurrence inside the cells. Since the current drop test setup is limited to a 2.76 *m* height and a 14.16 *kg* drop mass, it was not possible to increase the impact load to a level at which short circuit occurs. Therefore, a quasi-static compression test was designed based on the UN DOT 38.3 requirements with some modifications. For this test (sample D), the sample was placed on a rigid plate and a 15.8 *mm* diameter steel rod was placed across the center of the cell. Another steel bar was pressed against the rod at a rate of 2 *mm/min* (see Fig. 3.10). The advantage of this steady compression test is that the load can be increased up to any desired amount depending on the load cell being used. Therefore, it can provide valuable information regarding the load levels leading to short circuit or mechanical failure inside the cell.

Sample D was crushed up to a load level of 50 *kN* and similar to the impact samples, the resistance between its terminals was measured using a multimeter (Fig. 3.11). Unlike the impact samples, measured resistance for sample D was 111.6  $\Omega$ , indicating an internal short circuit inside the cell (see Table 3.5).

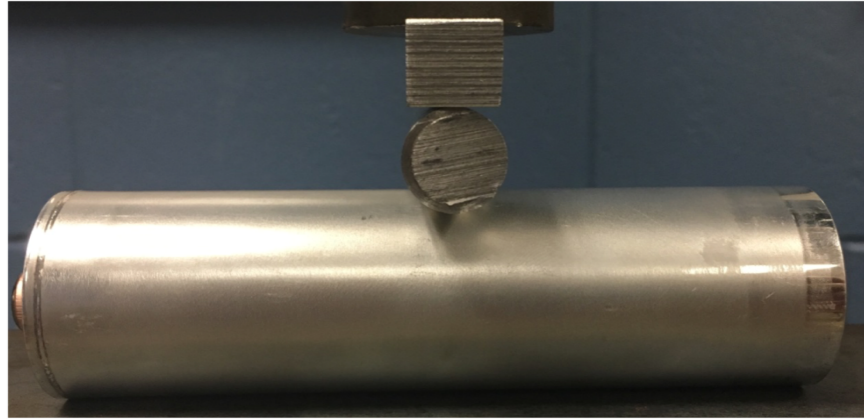


**Figure 3.10:** Sample D, quasi-static compression test by a steel rod.



**Figure 3.11:** Resistance measurement for sample D using a digital multimeter.

**Table 3.5:** Resistance values for crushed cells after impact and steady compression tests.

	Resistance ( $\Omega$ )
Sample A (Impact)	Overload
Sample B (Impact)	Overload
Sample C (Impact)	Overload
Sample D (Compression)	111.6 ( <b>Short</b> )



Since the steady compression test with a maximum load of  $50\text{ kN}$  led to an internal short circuit, a new set of experiments was conducted to monitor the state of the cell and track any separator failure and short circuit occurrence during the tests. In order to monitor voltage and resistance changes, the simple circuit of Fig. 3.12 was used where a  $1\text{ M}\Omega$  resistor was connected to the cell in series. A 5-volt power supply was attached to the circuit in order to monitor any current passing through the cell in case of short circuit. Two channels of a Hewlett Packard 34970A data acquisition system (Fig. 3.13a) was utilized to measure the voltage over the  $1\text{ M}\Omega$  resistor and also cell's resistance. At the beginning of the tests, there was no connection between the cell's anode and cathode electrodes; therefore, no current passed through the circuit and the data acquisition system showed a zero value for voltage and an infinite value for cell's resistance. These values remained constant until there was a separator failure due to compressive loads when the resistor voltage rises to maximum and cell's resistance drops to a small value as a result of a short circuit.

For this series of experiments, an Instron 5985 tensile testing machine with a  $250\text{ kN}$  load cell was used to be able to apply higher compressive loads. Again, the cell was placed on a rigid plate attached to the lower crosshead. A  $15.8\text{ mm}$  diameter steel rod was placed across the center of the cell. The upper crosshead applied displacement against the rod at a rate of  $2\text{ mm/min}$  (Fig. 3.13b). Both of the tensile testing machine and data acquisition system were set to start recording data simultaneously.

The experiments were conducted in two terminals orientations: horizontal and vertical. Five samples were tested at each orientation. Fig. 3.14 shows two cells with horizontal and vertical orientations before and during the tests. The experiments continued until there was a major mechanical failure causing a significant drop in the load-displacement curve. In all of the samples, electrical short circuit happened before mechanical collapse in the batteries. The maximum deformation of the cell is located in the middle part of the cell and below the rigid bar and therefore, any possible separator failure is likely to be near that area.

The load-displacement curves found from steady compression tests are plotted in Fig.

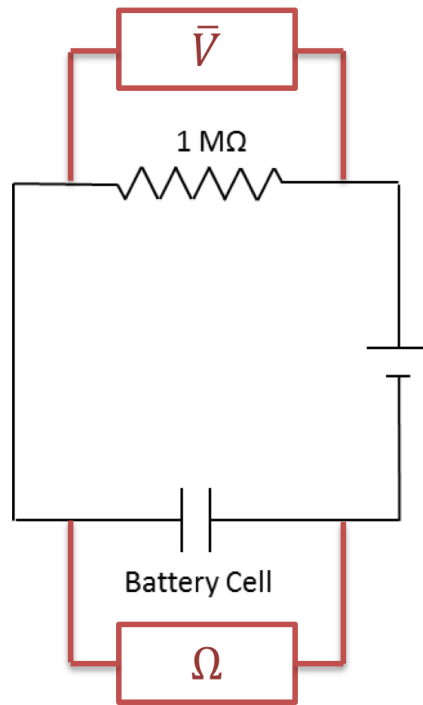
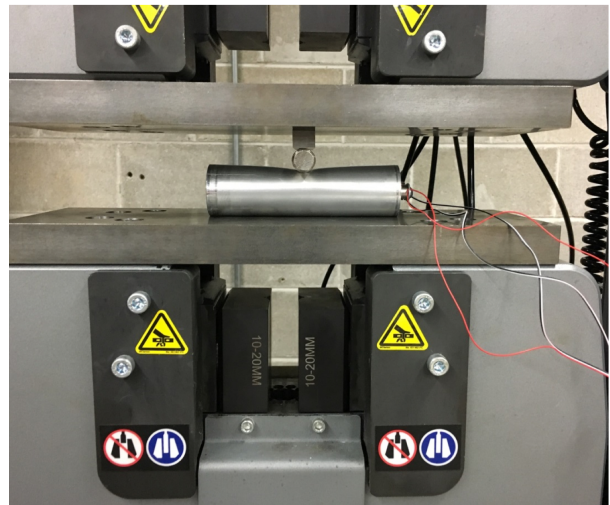


**Figure 3.12:** Schematic of the circuit used for steady compression tests with live resistance measurements.



(a)



(b)

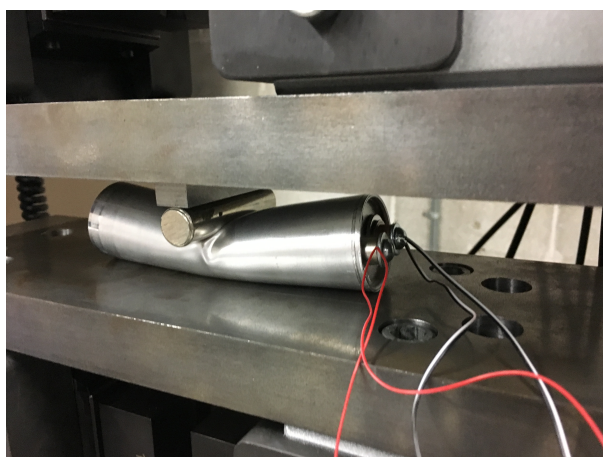
**Figure 3.13:** An Instron 5985 universal testing machine and a Hewlett Packard 34970A data acquisition system being used for steady compression tests.



(a)



(b)



(c)



(d)

**Figure 3.14:** Cylindrical cell with horizontal and vertical terminal orientations being compressed using a steel rod.

3.15a. Comparison of the 5 cells with horizontal terminals and the 5 cells with vertical terminals indicates that the orientation of the terminals does not have any significant effects on load carrying behavior of the cell. Similar to the previous compression tests of flattened jellyroll samples, the first part of the curves has a relatively small slope. After the jellyroll layers are compressed enough, the load starts to rise at a much higher rate at about 12 *mm* displacement. Mechanical failure and load drop occurs at about 64-68 *kN* and 19-20 *mm* indentation for all of the samples. Voltage change across the 1 *MΩ* resistor is plotted in Fig. 3.15b. Since there is no current before anode and cathode come into contact, voltage is also zero across the resistor. At displacements of between 17.5 *mm* and 19 *mm*, short circuit occurs and voltage jumps to a value near 5 volts. Similar to the load-displacement curves, there seems to be no correlation between the cell orientation and short circuit occurrence for steady compression tests.

Fig. 3.16 depicts the voltage change and compressive load on the same displacement scale. Voltage change in all of the 10 tested samples shows that short circuit occurs before a complete mechanical collapse in the cell. It seems that chances of separator failure is the highest in an indentation range of between 17.5 *mm* and 19 *mm*, while structural failure and load drop occurs at about 20 *mm* indentations for all of the samples.

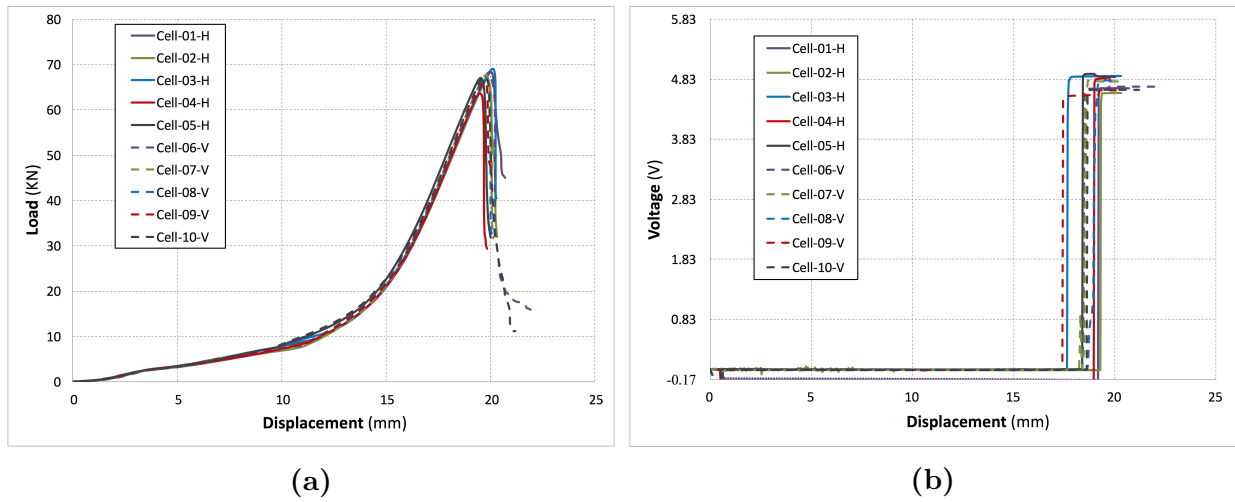


**Figure 3.15:** (a) Recorded load-displacement curves for steady compression tests and (b) Recorded voltage change over the 1 *MΩ* resistor.

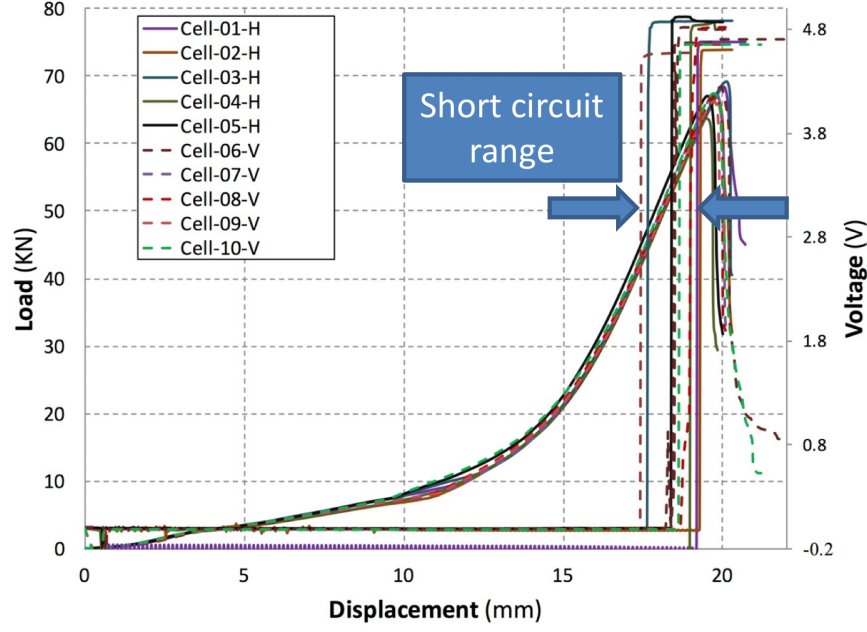


**Figure 3.16:** Load and voltage changes for steady indentation tests.

### Estimation of drop configurations leading to short circuit:

Results from the quasi-static compression tests, demonstrated that in order to reach a short circuit, there must be at least  $45 \text{ kN}$  of compression load when a steel rod is used. Since none of the impact tests led to an internal short circuit, assuming quasi-static compression force is equivalent to average impact force, a minimum drop mass required to cause a short circuit in the present drop test apparatus can be roughly estimated. Average impact force can be calculated by Eq. 3.1 as change of drop cart's momentum during impact, where  $m$  is drop mass,  $V_1$  and  $V_2$  are drop cart's velocity before and after impact and  $t_{\text{impact}}$  is the impact time.

$$F_{\text{impact}} = \frac{d(mV)}{dt} = m \frac{V_2 - V_1}{t_{\text{impact}}} \quad (3.1)$$

Table 3.6 lists various parameters required to estimate the drop mass. It is assumed that the current apparatus is being used, therefore, drop height remains  $2.76 \text{ m}$ . Friction and air resistance will still be available, thus based on the previous measurements, drop acceleration

is estimated to be  $0.8\text{ g}$ . Based on the drop height and acceleration, impact velocity ( $V_1$ ) can be calculated. In the actual tests,  $V_2$  will be a fraction of  $V_1$  (in the order of 1 to 2  $m/s$ ) in the opposite direction; However, here we are assuming a perfectly plastic impact to be able to estimate the minimum impact force. The actual impact force will be more because of the opposite direction of  $V_2$ . Finally, impact time is estimated to be about 6  $ms$  based on the finite element results. Using the aforementioned values and the 45  $kN$  impact force in Eq. 3.1, a minimum of 41.0  $kg$  mass is required for the drop cart to cause a short circuit during an impact test. The present drop test setup would not withstand that amount of weight because of the size of extrusions and strength of attachments.

**Table 3.6:** Estimation of drop mass leading to short circuit.

Drop height	2.76 $m$
Drop acceleration	0.8 $g$
Impact velocity	6.58 $m/s$
Impact time	6 $ms$
Minimum impact force for short circuit	45 $kN$
<b>Expected drop mass for short circuit</b>	41.0 $kg$

### 3.3 Post Processing of Crushed Cells

Two methods were utilized to further inspect the jellyroll for highly deformed layers: Computed tomography and optical microscopy.

#### 3.3.1 Computed Tomography Scanning of Battery Cells

Critically deformed cells which lead to short circuits were analyzed using computed tomography (CT scanning) for a non-destructive observation of the internal failure modes. The scans were performed on a North Star Imaging machine then analyzed using Mimics reconstruction software. One of the CT-scanned cells was sample D from Section 3.2 which



was compression tested up to 50  $kN$  load. Results indicated highly distorted layers on both sides of the aluminum core, depicted in Fig. 3.17. Also, looking closely at the layers adjacent to the aluminum core, failure of a copper layer can be spotted in Fig. 3.18. In the CT images, copper is illustrated as the brighter material due to the higher density compared to the aluminum cathode and polymer separator.

The second CT-scanned cell was chosen from one of the 10 cells tested with live voltage/resistance measurements. The cell had been compressed up to a load level of more than 65  $kN$  and test had been stopped after mechanical failure and load drop, therefore, it was tested under more catastrophic conditions compared to sample D. The computed tomography image of this cell illustrated in Fig. 3.19, shows how all layers and aluminum core sheared from top to bottom through approximately 75% of the jellyroll thickness.

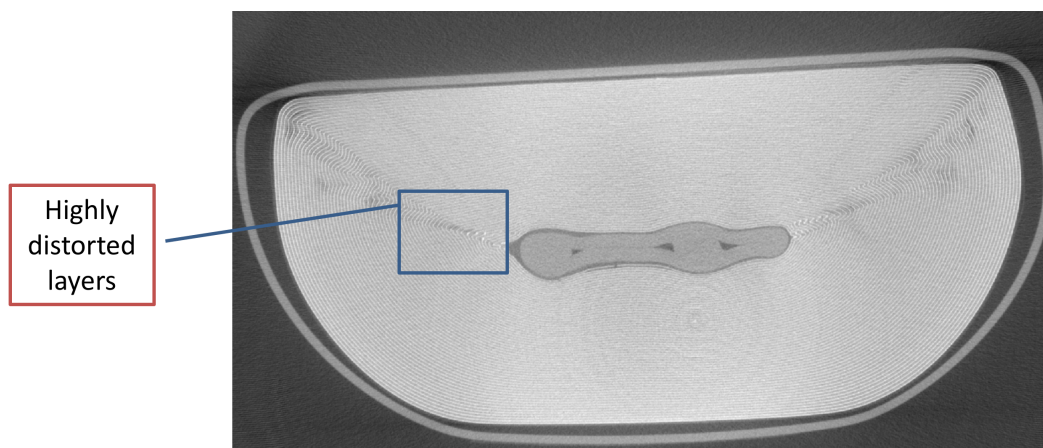


**Figure 3.17:** CT scan of a crushed cell after steady compression test (sample D) showing highly distorted layers.

### 3.3.2 Microscopy of Crushed Jellyrolls

In order to study the deformations of jellyroll layers and possibility of internal short circuits, optical microscopes were utilized to look at the cross section of crushed samples. Optical microscopy required to cut the jellyroll at the middle of the cell which could destruct the layers. Thus, resin casting was used before cutting the cell to reduce the chance of any

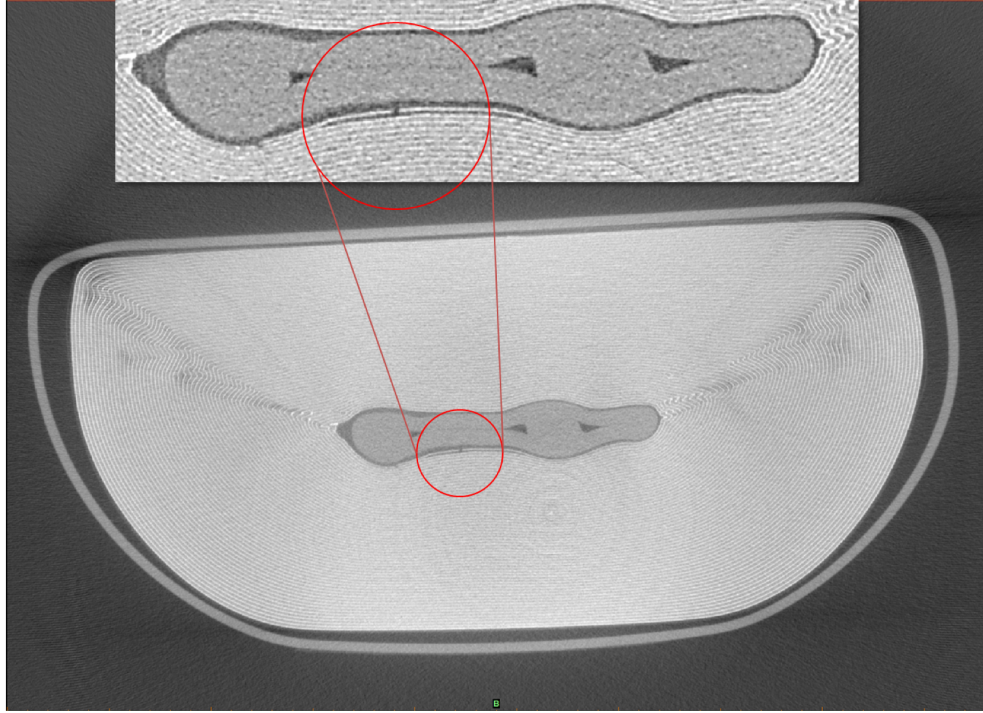


**Figure 3.18:** CT scan of a crushed cell after steady compression test (sample D) showing a crack in an electrode near the aluminum core.

extra distortion of layers during the cutting process. First the cell was cut into three pieces, depicted in Fig. 3.20. The middle piece was placed in a plastic cup and a mix of epoxy resin-hardener with a mass ratio of 25:3 was poured into the cup and was cured overnight (Fig. 3.21). A vacuum chamber was also used for an hour to let resin flow well inside the sample and enclose the casing and jellyroll layers. The relatively rigid cured sample was then cut carefully using a band saw in the most deformed cross section. The surface was then polished several times to reach to a level of 1200 grit size. Fig. 3.22a and 3.22b compare the unpolished and polished jellyroll surfaces. The polished sample was then used to be looked at in an optical microscope with various magnifications from  $6.5\times$  to  $200\times$ . One impact-tested cell and once compression-tested cell (samples C and D) were chosen for microscopy.

All of the microscopic images shown here belong to sample D of Section 3.2. From the images three critical regions could be identified in the crushed cell: Similar to computed tomography images, there are areas with highly distorted layers on both sides of the cell



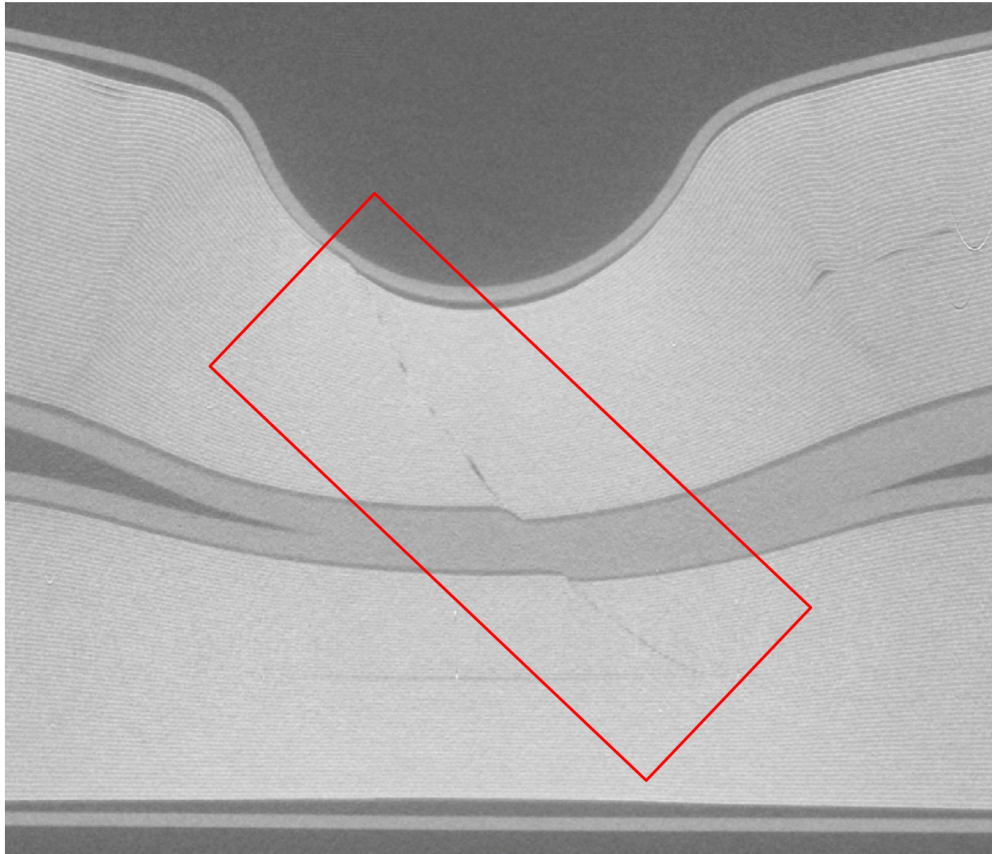


**Figure 3.19:** CT scan of a crushed cell after mechanical collapse showing cracks in the jellyroll and the aluminum core.



**Figure 3.20:** A crushed cell before cutting the middle section for microscopy of jellyroll layers.

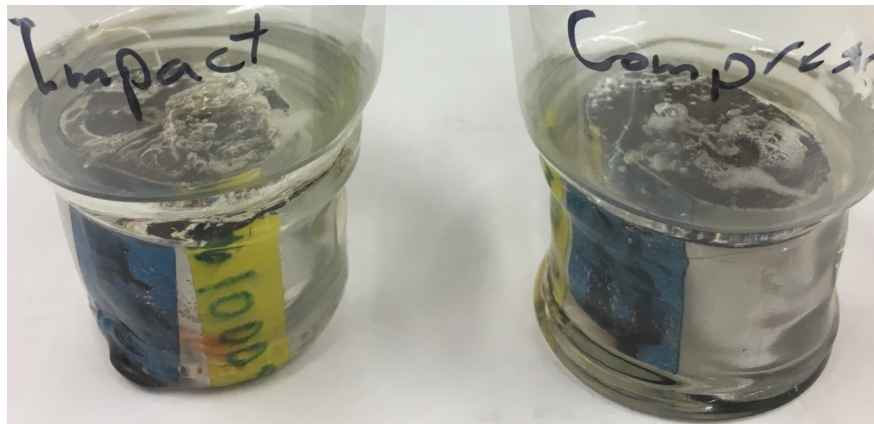
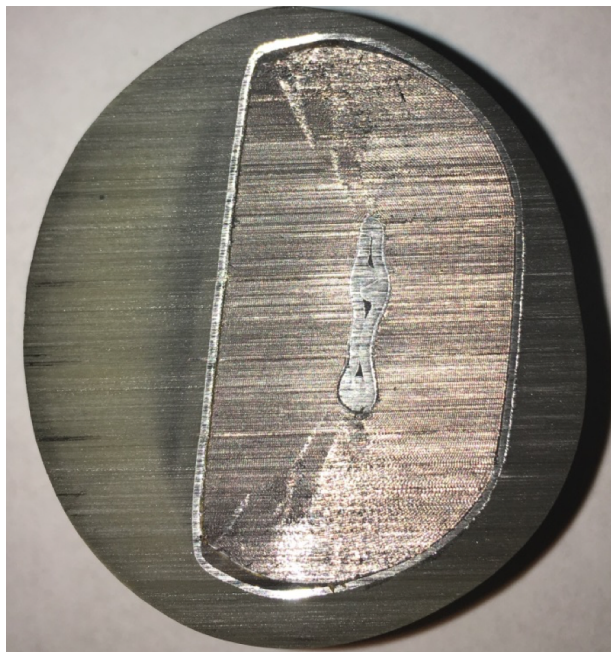
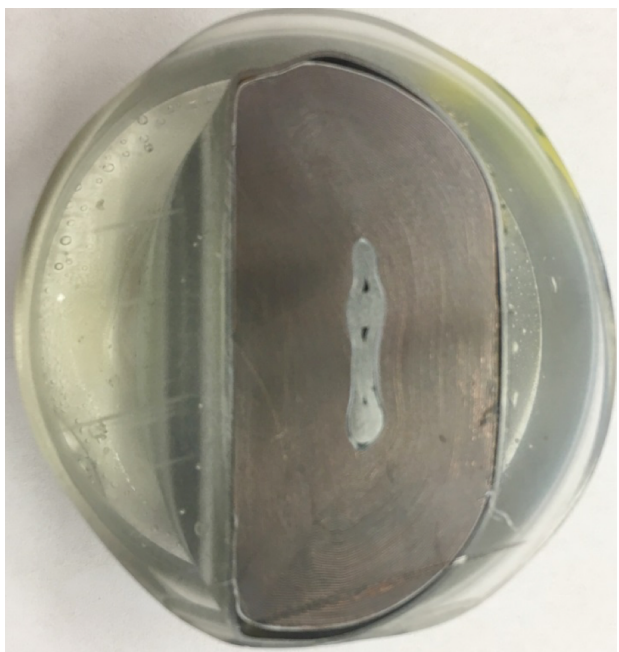


**Figure 3.21:** Deformed jellyrolls after resin casting.



(a)



(b)

**Figure 3.22:** (a) Resin molded sample after being cut at the highest deformed cross section and (b) Polished cross section (1200 grit size).



core, depicted in Fig. 3.23a. There are also highly compressed layers adjacent to the casing where the testing machine's fixed and moving platens are in contact with the cell (see Fig. 3.23b). Images with higher magnification factors show that there are locations where the separator layer failed due to high compressive load resulting a contact between anode and cathode layers, shown in Fig. 3.24. The third critical area seems to be the layers adjacent to the aluminum core where high tensile loads might cause fracture in layers. Fig. 3.25 shows one of these failures in a copper layer in the vicinity of cell core. The same failure was captured before using computed tomography.

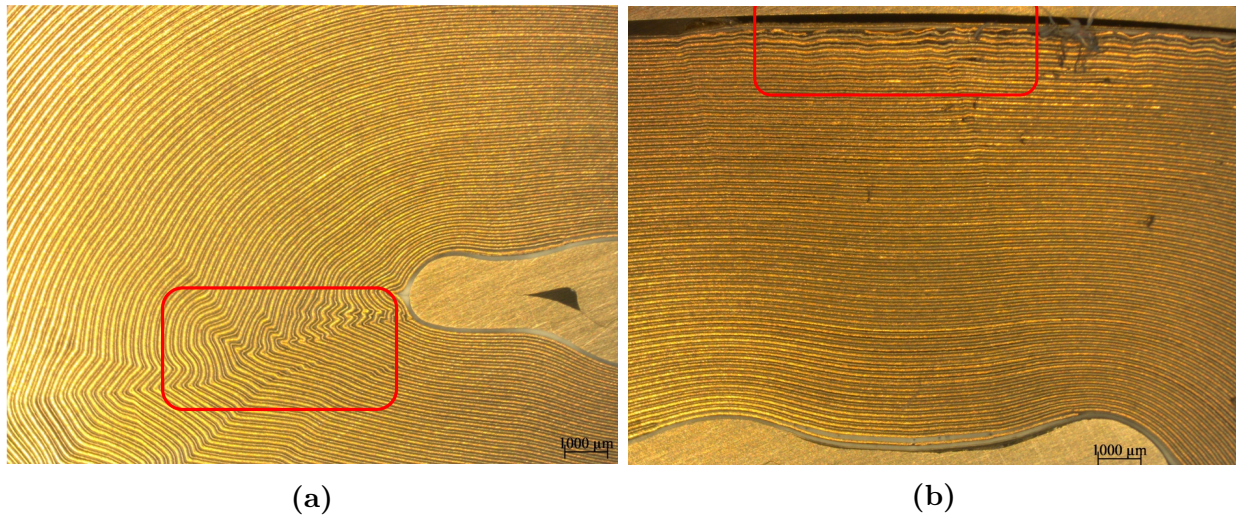


**Figure 3.23:** Microscopic images of a deformed jellyroll (6.5x magnification) (a) Highly distorted layers and (b) Layers/separator failure near the casing.

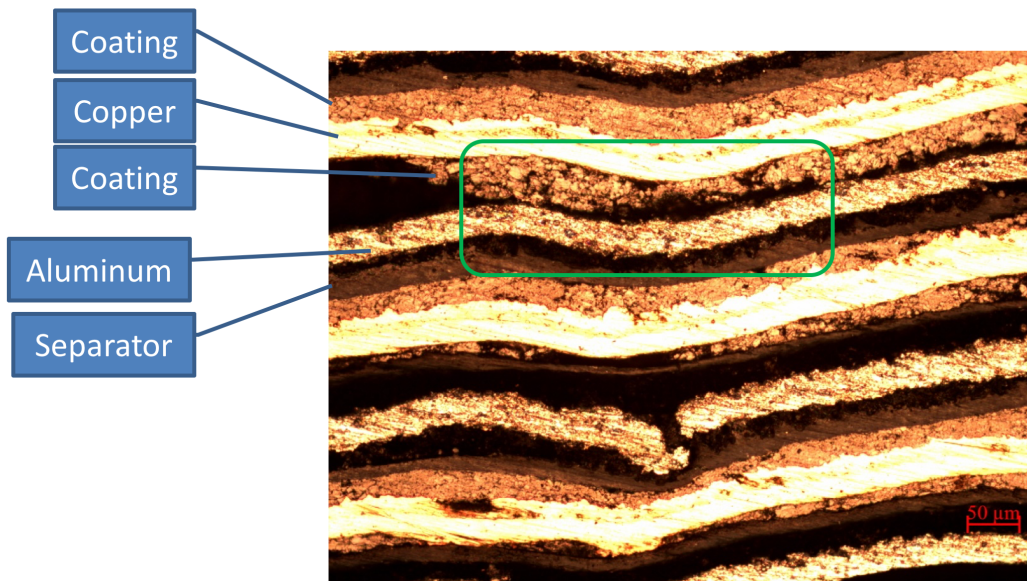


**Figure 3.24:** Separator failure near the casing (200x magnification).

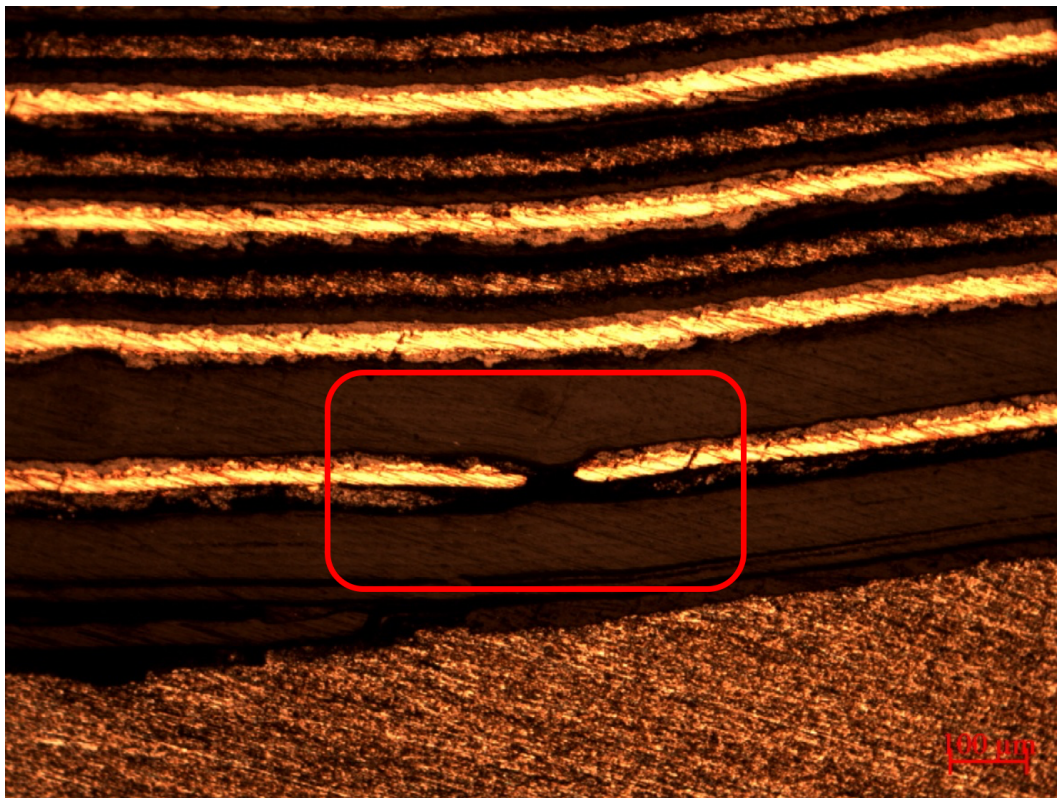


**Figure 3.25:** Copper layer failure adjacent to the aluminum core (100x magnification).

---

## Chapter 4

### Cell Level: Explicit Finite Element Analysis

#### 4.1 Lateral Impact between Two Flat Plates

##### 4.1.1 Homogeneous Jellyroll Model

An explicit finite element model of a cylindrical cell was developed to simulate lateral impact in LS-DYNA (see Fig. 4.1 and 4.2). All of the finite element models in this study (i.e. geometry, nodes and elements) were generated using ANSYS APDL and the models were transferred to LS-DYNA using a custom-developed APDL macro. For the homogeneous model, the crushable foam material model was used as the constitutive model for the jellyroll [83], incorporating the stress-strain curve from the flattened jellyroll tests discussed in Section 2.1. The tensile cut-off value of the crushable foam model was set to 10 *MPa*, based on the tensile strength for coated aluminum, coated copper and separator [87]. The casing and the core tube were assumed to be made of aluminum 1100 (with properties of 99 *MPa* yield strength and 111 *MPa* ultimate strength) and modeled in LS-DYNA using material model 24 (Piecewise linear plasticity). The internal spacer between the terminals and the jellyroll was assumed to be made of polyetherimide and modeled in LS-DYNA with material model number 3 (Mat\_plastic\_kinematic) [111, 112]. A total of 19,740 solid elements with one-point integration used to model all of the components of the cell. Having elements with reduced formulation in the model, hourglass Type 6, Belytschko-Bindeman was used to prevent nonphysical, zero-energy modes [111, 112].

The battery cell was assumed to be crushed between a lower and an upper rigid plates (see Fig. 4.3). Lower plate was stationary and assuming a drop height of 2.78 *m*, impact



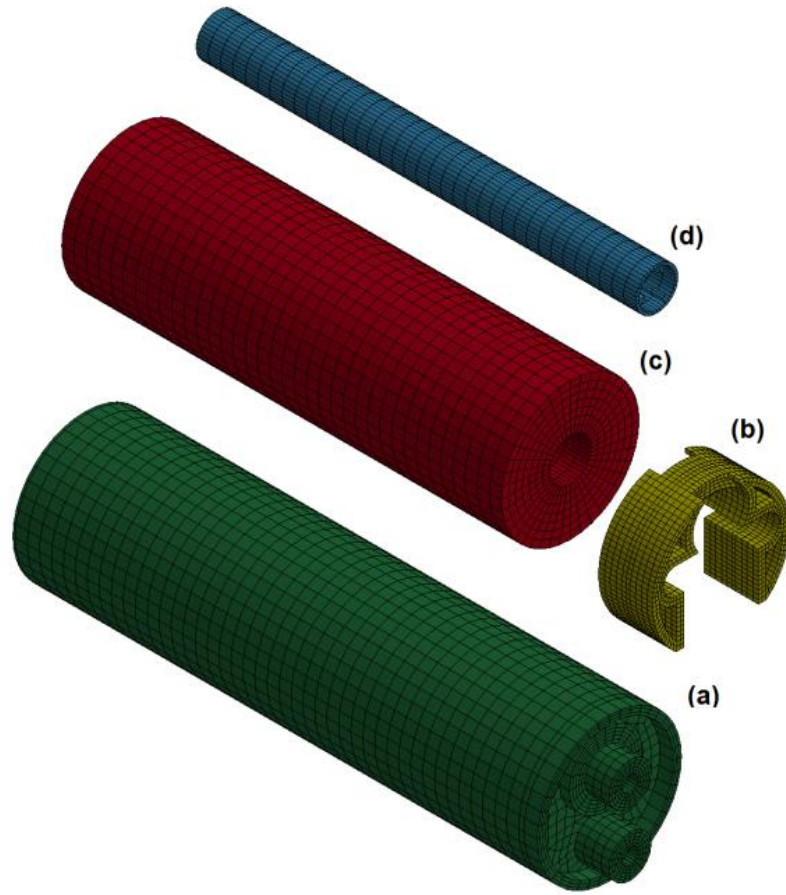


**Figure 4.1:** Main components of a cell's finite element model: (a) case, (b) spacer, (c) homogenized jellyroll and (d) inner tube.

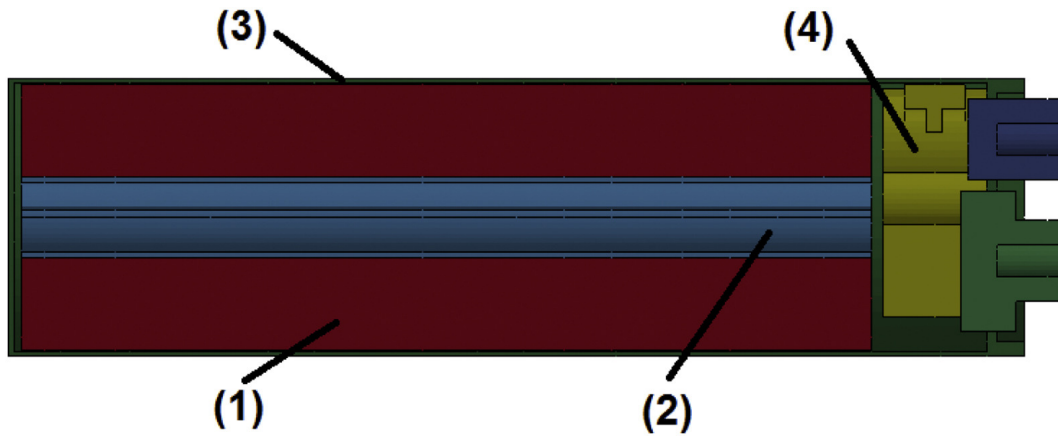


**Figure 4.2:** Cross section of a cell's finite element model: (1) jellyroll, (2) aluminum core, (3) case and (4) spacer.

velocity was calculated to be  $7.4 \text{ m/s}$  for the upper plate. Two impact configurations with vertical and horizontal terminal orientations were considered and each configuration were analyzed using two drop mass values of  $11.34 \text{ kg}$  and  $22.68 \text{ kg}$ .

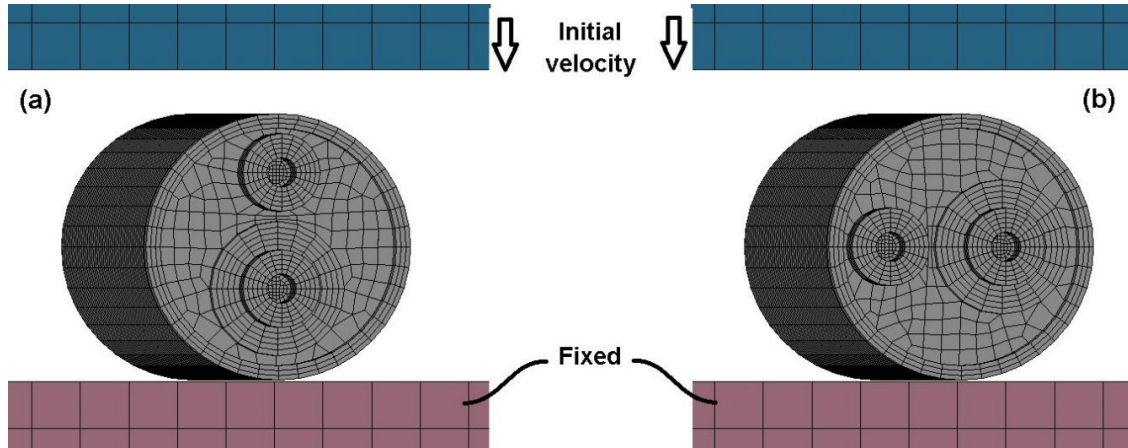


**Figure 4.3:** Cell impact configurations: (a) vertical and (b) horizontal.

Fig. 4.4 shows the deformed shape of the cell with horizontal terminals found through the finite element analysis. In order to compare the results to the experiments and verify the finite element simulation, deformed cells' dimensions at three sections (A) top, (B) middle and (C) bottom are listed in Table 4.1. The first two rows list the values for the cell with horizontal terminals, and the last two rows compare the thickness for the cell with vertical terminals. The difference between the experiments and the finite element results in most cases is less than 5%, especially for sections B and C where jellyroll is located. Some of the errors can be attributed to the fact that, in the experiments, the drop cart might tilt sideways during the impact, causing less deformations in the terminal side of the cell because of its higher stiffness. Jellyroll's stress-strain curve, assuming an isotropic material model, and the skipping rate dependency of the mechanical properties can be other sources of the error.

Impact loads were calculated using the forces transferred through the contact between the drop cart and the cell and are plotted over time in Fig. 4.5. The maximum impact load was found to be  $120\text{-}140 \text{ kN}$  and  $44\text{-}48 \text{ kN}$  for  $22.68 \text{ kg}$  and  $11.34 \text{ kg}$  drop mass

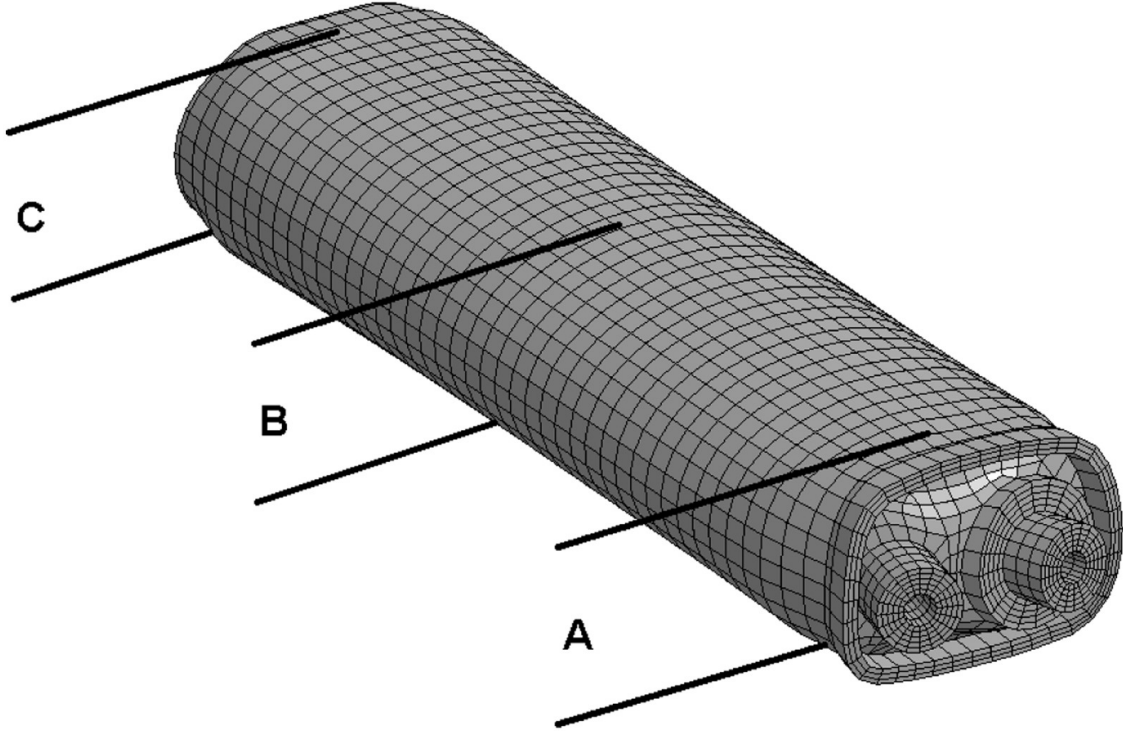


**Figure 4.4:** Deformation comparison locations (horizontal orientation, 11.34 *kg* weight).

**Table 4.1:** Deformed thickness comparison for the cells with horizontal (h) and vertical (v) terminals.

	A ( <i>mm</i> )		B ( <i>mm</i> )		C ( <i>mm</i> )	
	11.34 <i>kg</i>	22.68 <i>kg</i>	11.34 <i>kg</i>	22.68 <i>kg</i>	11.34 <i>kg</i>	22.68 <i>kg</i>
Experiments (h)	30.5	28.4	29.6	27.2	27.5	23.5
FE results (h)	28.2	24.6	28.8	26.1	25.9	23.3
Experiments (v)	29.7	27.8	30.2	27.6	27.0	24.4
FE results (v)	29.4	25.8	30.0	27.4	25.5	23.0



respectively. Variation of the plate's velocity over time is also plotted in Fig. 4.6. During the impact, the velocity changes from  $7.38 \text{ m/s}$  in the downward direction to  $1.6\text{-}2.7 \text{ m/s}$  in the upward direction. From the velocity curve, impact duration can be estimated to be around  $3.7 \text{ ms}$  and  $3.2 \text{ ms}$  for the  $11.34 \text{ kg}$  and  $22.68 \text{ kg}$  drop mass cases. Considering the fact that the drop plate is rigid, mean impact force can be estimated using the plate's change of linear momentum. These average impact force values are calculated using Eq. 4.1. Calculated average forces are listed in Table 4.2 and are in agreement with the load variations plotted in Fig. 4.5 which can be another criterion to verify the simulation results. Terminal orientation slightly changes the maximum impact load, however average impact force and impact duration remains the same.

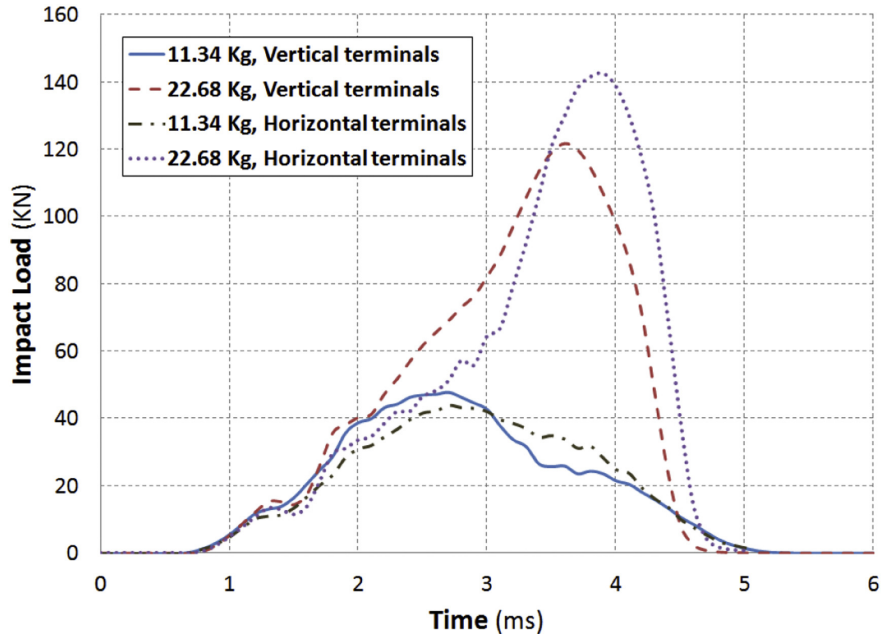


**Figure 4.5:** Impact load for various load cases and cell orientations.

$$F_{impact} = \frac{d(mV)}{dt} = m \frac{V_2 - V_1}{t_{impact}} \quad (4.1)$$

In order to find the deformed shape of individual components inside the cell, deformed cells were CT scanned using a North Star Imaging 3-D computed tomography system at

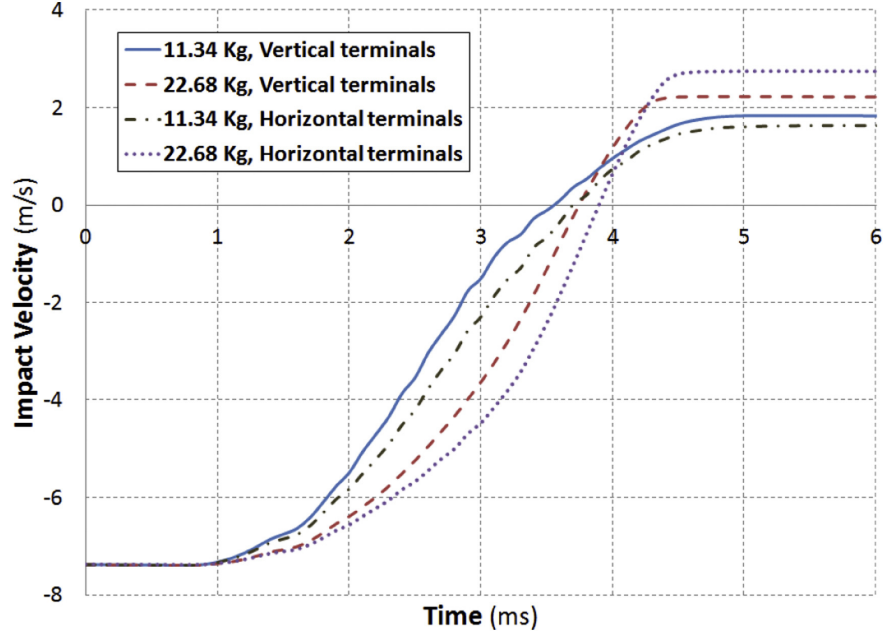


**Figure 4.6:** Impact velocity for various load cases and cell orientations.

**Table 4.2:** Average impact force estimation.

Cell orientation	Weight ( $kg$ )	Impact time ( $ms$ )	Average impact force ( $m/s^2$ )
Vertical	11.34	3.7	28.1
Vertical	22.68	3.2	67.8
Horizontal	11.34	3.7	27.5
Horizontal	22.68	3.2	69.3

Johnson Controls Inc. battery testing laboratory (Glendale, WI). Fig. 4.7 compares two cross sections of the cell after impact with 11.34 *kg* drop mass with the deformed shapes found from finite element simulation. Thickness of jellyroll and inner tube was measured at both sections and is listed in Table 4.3. A comparison of cell dimensions shows that the overall deformed geometry, and specifically jellyroll, is in very good agreement with the CT scanned cell. Simulation errors for jellyroll thickness is less than 1%.

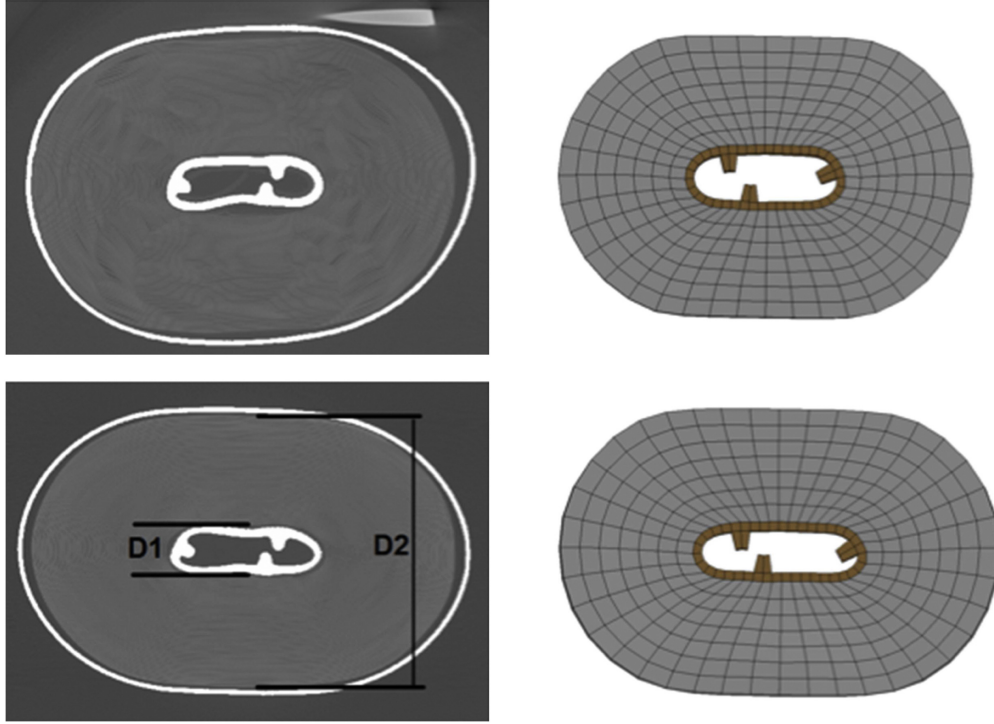


**Figure 4.7:** Comparison of the cell's deformed shape after impact; CT-scan vs. finite element results (11.34 *kg* drop mass, horizontal orientation).

**Table 4.3:** Deformed shape thickness comparison of internal components.

	Top cross section ( <i>mm</i> )		Bottom cross section ( <i>mm</i> )	
	Inner tube (D1)	Jellyroll (D2)	Inner tube (D1)	Jellyroll (D2)
CT scan	4.45	25.19	4.29	24.11
Simulation	5.85	25.00	5.07	24.23

Deformed shapes and Von-Mises stress contours for jellyroll and center tube are displayed in Fig. 4.8. For the case of impact between flat plates, the risk of a short circuit occurrence

and the consequent thermal runaway is not as high as the cases of impact in axial direction or penetration by sharp objects [1]. This is because distributed load is applied perpendicular to the plane of electrodes. In this case, areas with high stresses may lead to a short circuit because of separator thinning or separator failure. Based on the simulation results, the inner parts of the jellyroll close to the inner tube experience higher stresses, and hence, can be assumed to be jellyroll's critical areas.

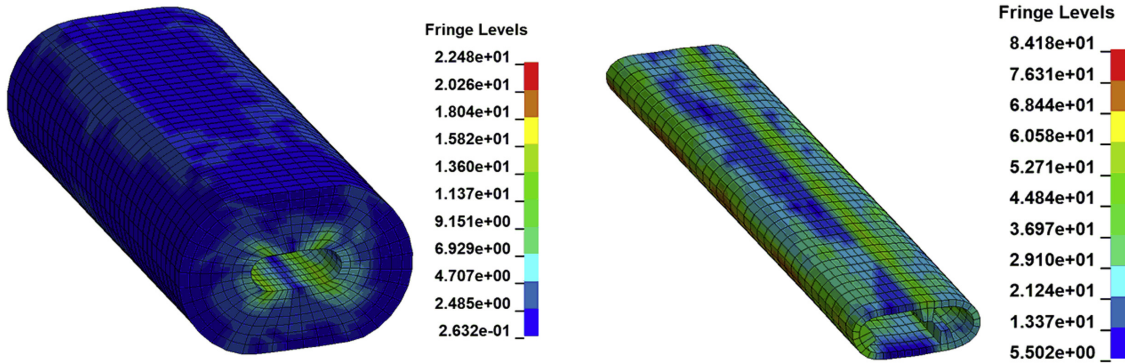


**Figure 4.8:** Jellyroll and inner tube's Von-Mises stress for the cell with horizontal orientation of terminals (11.34 *kg* drop weight).

### 4.1.2 Heterogeneous Jellyroll Model

In the previous section, an explicit finite element model of a cylindrical cell was developed in LS-DYNA to simulate lateral impact. The simulation was performed assuming homogenized mechanical behavior for the jellyroll. The crushable foam material model was used as the constitutive model of the jellyroll, incorporating the stress-strain curve, found from flattened jellyroll tests. The homogeneous model cannot provide any information regarding jellyroll's individual layers. Therefore, a heterogeneous finite element model of the cell was also developed to better predict the behavior of the cell under extreme loading conditions. The model incorporated the compressive properties of the jellyroll's individual layers reported in Section 2.2, Using the stress-strain curves found in Fig. 2.13, jellyroll layers were assigned crushable foam model with different tensile cut-off values. Anode, cathode and separator layers (Fig. 4.9a) have very small thicknesses ( $\sim 25 - 75 \mu\text{m}$ ) which leads to com-

putational complexities such as: (1) elements will have high aspect ratios, and (2) time step size will be very small resulting in a very large solution time. In order to mesh the jellyroll, the layers were divided to 300 elements in axial direction and 300 elements in tangential direction, leading to a maximum element size of about  $0.38 \times 0.38 \text{ mm}$  for the outer layer. Inner layers had smaller element sizes in tangential direction. Coincident nodes of adjacent layers were merged together. Fig. 4.9b compares the homogeneous and heterogeneous jellyroll models. The complete battery cell with a layered jellyroll was modeled using about 22 million solid elements. The casing and the core tube were assumed to be made of aluminum 1100 (with properties of 99 *MPa* yield strength and 111 *MPa* ultimate strength) and modeled in LS-DYNA using material model 24 (Piecewise linear plasticity). The internal spacer between the terminals and the jellyroll was assumed to be made of polyetherimide and modeled in LS-DYNA with material model number 3 (Mat\_plastic\_kinematic) [111, 112]. All of the components were modeled using one-point integration solid elements. Having elements with reduced formulation in the model, hourglass Type 6, Belytschko Bindeman was used to prevent nonphysical, zero-energy modes [111, 112]. The cell was assumed to be stationary on a rigid plate, while another plate having a mass of 11.34 *Kg* impacted the cell with a speed of 7.4 *m/s* (see Fig. 4.9c).

The model was solved on an HPC cluster using 192 cores and a memory of 3 GB/core and the solution time was 58 hours. Previous lateral drop-test experiments were used to compare the deformed shape found from the simulations. CT-scan of a jellyroll's cross section after drop-test is shown in Fig. 4.10c and is compared to the deformed shapes found from homogeneous and heterogeneous simulations (Fig. 4.10a and 4.10b). Fig. 4.10d depicts the impacting plate's velocity during impact for homogeneous and heterogeneous models. Using the velocity curves, the impact time can be estimated to be about 4 *ms* for both models. Fig. 4.10e shows how the impact load changes over time. The difference between the two curves can be attributed to the fact that in the heterogeneous model, load carrying capacity of layers are different while in the homogeneous model, a single stress strain curve is used

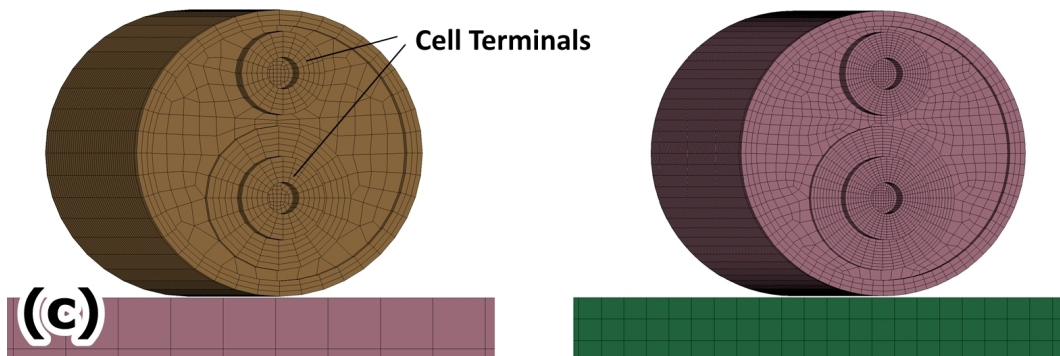
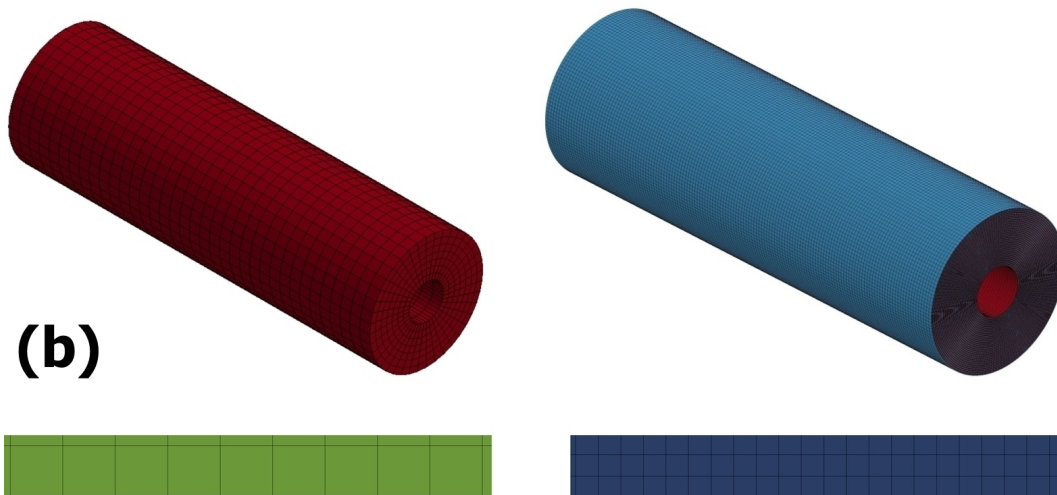
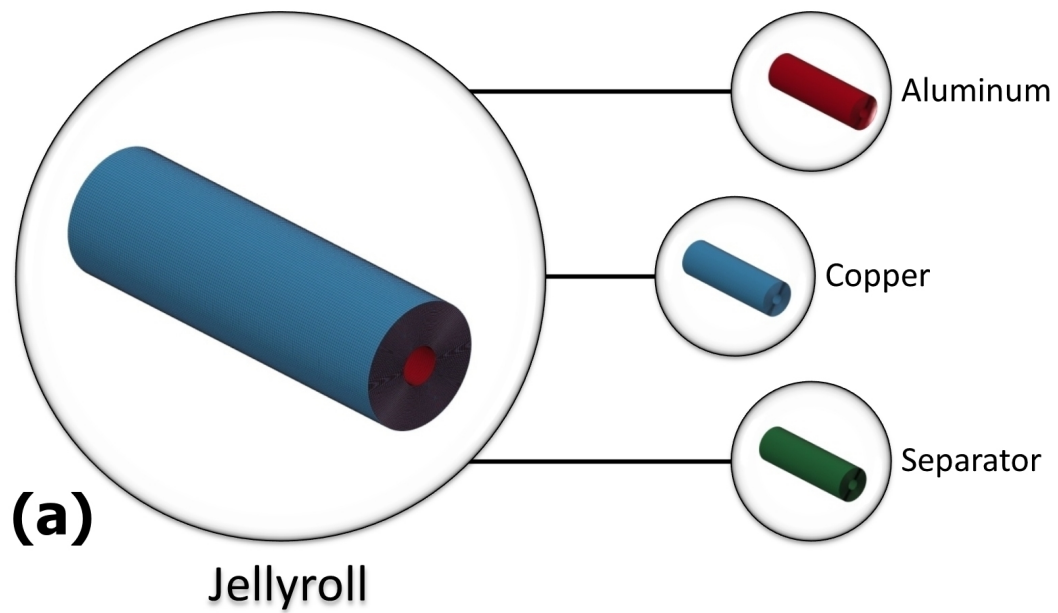


**Figure 4.9:** (a) Finite element model of jellyroll layers, (b) Comparison of homogeneous and heterogeneous jellyroll models and (c) Comparison of homogeneous and heterogeneous cell models.

for all of the jellyroll elements. Thickness of the deformed cell at different locations (top, middle and bottom of the casing) is listed in Table 4.4 for the experiment and simulations.

**Table 4.4:** Cell's deformed thickness under 11.34 *kg* impact load.

	<b>Top</b> ( <i>mm</i> )	<b>Middle</b> ( <i>mm</i> )	<b>Bottom</b> ( <i>mm</i> )
Experiment	29.7	30.2	27.0
FE (Homogeneous)	29.4	30.0	25.5
FE (Heterogeneous)	28.1	30.9	28.2

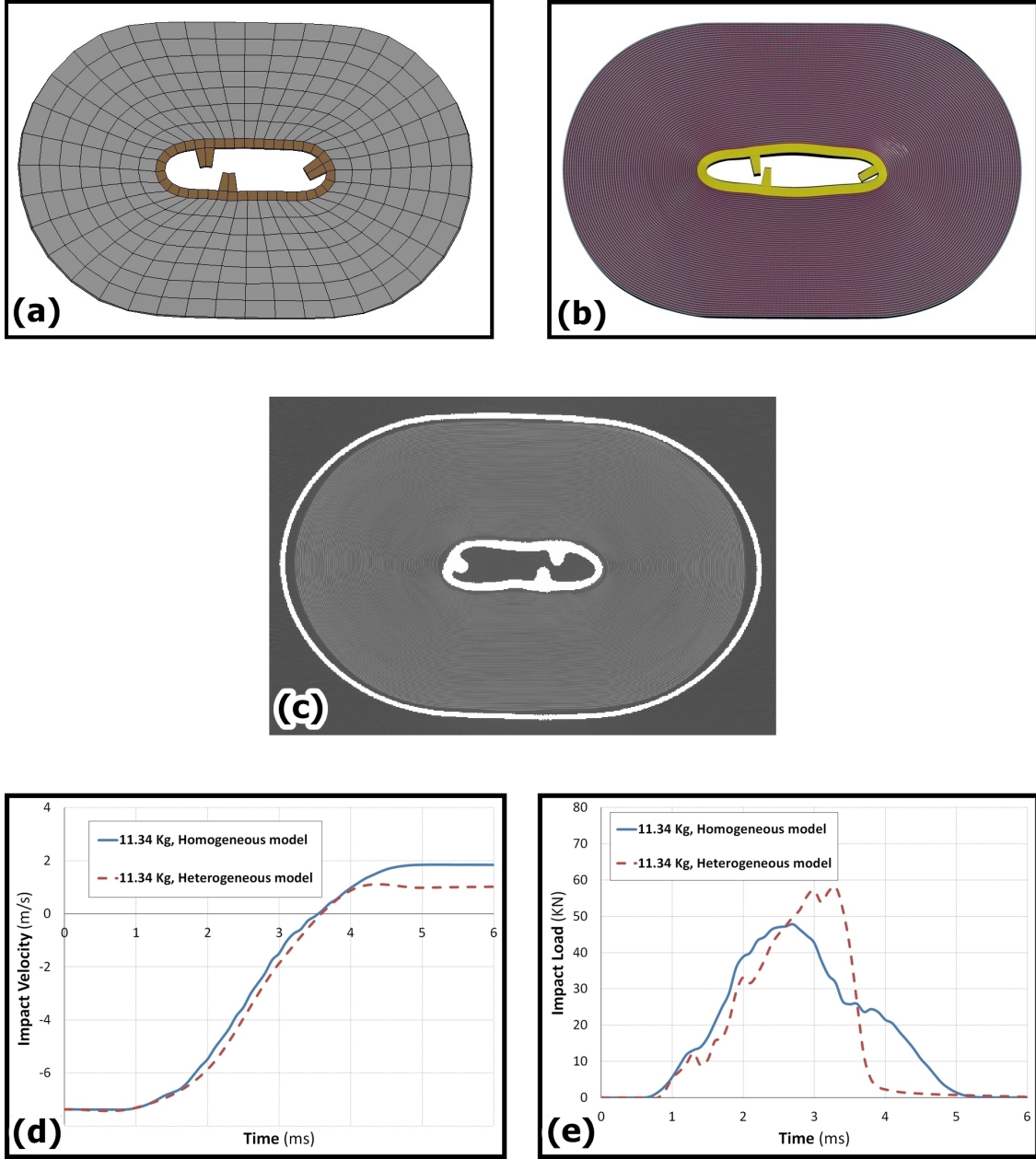
Strain values for separator layers were extracted from the simulation results. Fig. 4.11 shows how the strain in the transverse direction changes with respect to radial location of separator layers. It compares variation of strain under maximum compression and after the load is removed. The fact that there is no significant difference between the two cases implies that most of the separator's deformation has been plastic. Also, the maximum thinning in both curves occurs at about  $r=13 \text{ mm}$  which means under high impact loads a short circuit is likely to occur at this radius due to separator thinning.

### 4.1.3 Updated Simulations using LVDT Characterizations

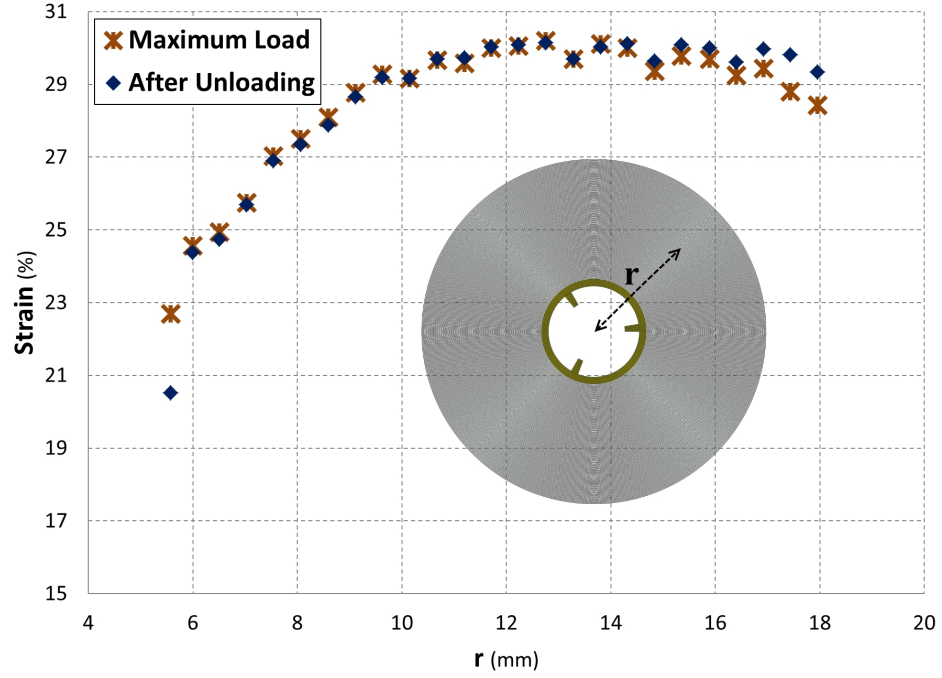
Jellyroll homogenization and characterization of individual jellyroll layers performed using LVDT deflection sensor resulted in different stress-strain curves compared to the original experiments, especially for higher stress levels. Therefore, the previous homogeneous and heterogeneous simulations were repeated using the new stress-strain curves to determine how this changes cell's deformation under impact. Simulation results for vertical terminal orientation and 11.34 *kg* impact weight is reported in this section. Table 4.5 lists the cell thickness at three (top, middle and bottom) cross sections. Comparison of the thicknesses from the simulations with the test data indicates a maximum error of less than 11% for the homogeneous model while the error is within 6% for the heterogeneous model.

Fig. 4.12 shows a contour plot of Von-Mises stress during impact (before the load is





**Figure 4.10:** (a) Jellyroll's deformed shape found from the homogeneous model, (b) deformed shape for heterogeneous model, (c) CT-scan of the crushed jellyroll, (d) Velocity change during impact and (e) Impact load for homogeneous and heterogeneous models.



**Figure 4.11:** Strain values of separator layers under maximum impact load and after unloading.

**Table 4.5:** Updated cell's deformed thickness using LVDT characterizations (11.34 *kg* impact weight).

	Top ( <i>mm</i> )	Middle ( <i>mm</i> )	Bottom ( <i>mm</i> )
Experiment	29.7	30.2	27.0
FE (Homogeneous, LVDT)	30.3	32.8	29.9
FE (Heterogeneous, LVDT)	28.0	30.9	28.4

removed) for the homogeneous model. As expected, most of the load is carried by the rectangular area under the impacting plate. Similar contour can be plotted for the heterogeneous model, however because of the extremely small size of the elements and since the stress values will be changing from layer to layer, anode and cathode layers were unselected and the stress contour was plotted only for separator layers in Fig. 4.13. The figure illustrates that separator stresses are the highest near the center of jellyroll and also adjacent to the impacting plate. Fig. 4.14 depicts velocity change and impact force for the new homogeneous and heterogeneous models. Changes in velocity and force indicates an impact duration of about 3 *ms*. Because of using a single material with homogenized mechanical properties, homogeneous model seems to behave symmetrically during impact and rebound phases. For the heterogeneous model, layers have different load carrying capacities and it takes longer to the peak value of impact force. Maximum impact force is about 65 *kN* for both models. The calculated rebound velocities are about 1 *m/s* for both homogeneous and heterogeneous simulations.

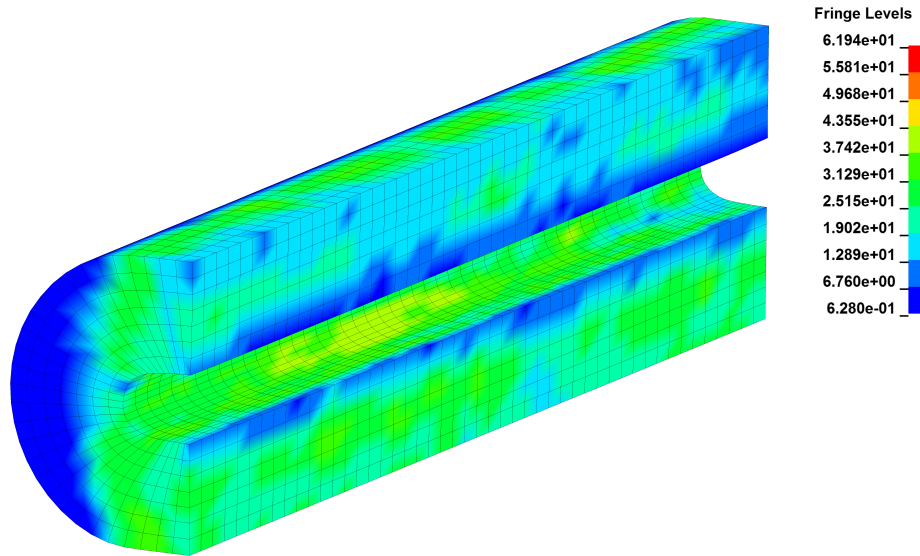


**Figure 4.12:** Jellyroll's Von-Mises stress contour (before unloading) for the homogeneous model.

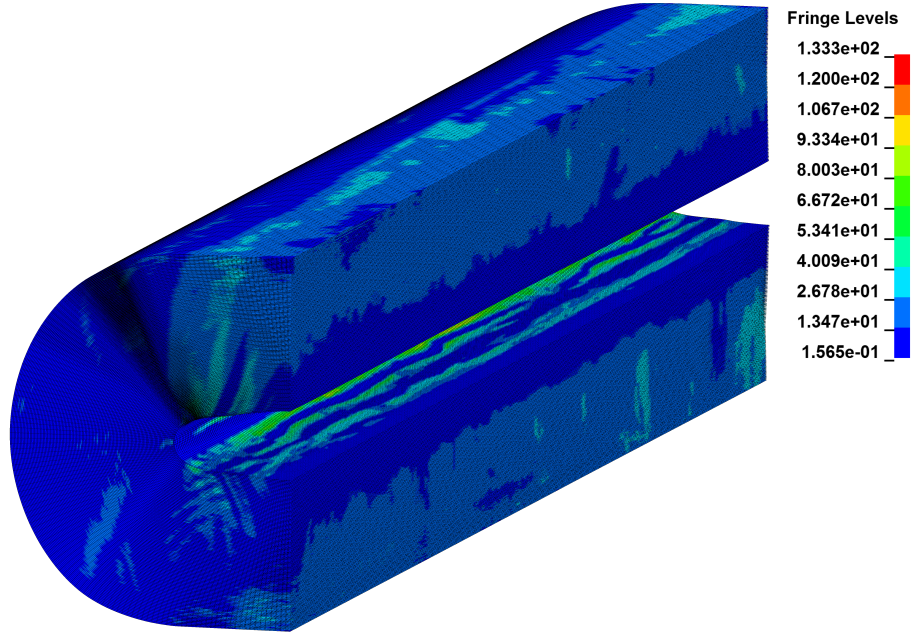


**Figure 4.13:** Von-Mises stress contour for separator layers in the heterogeneous model (before unloading).

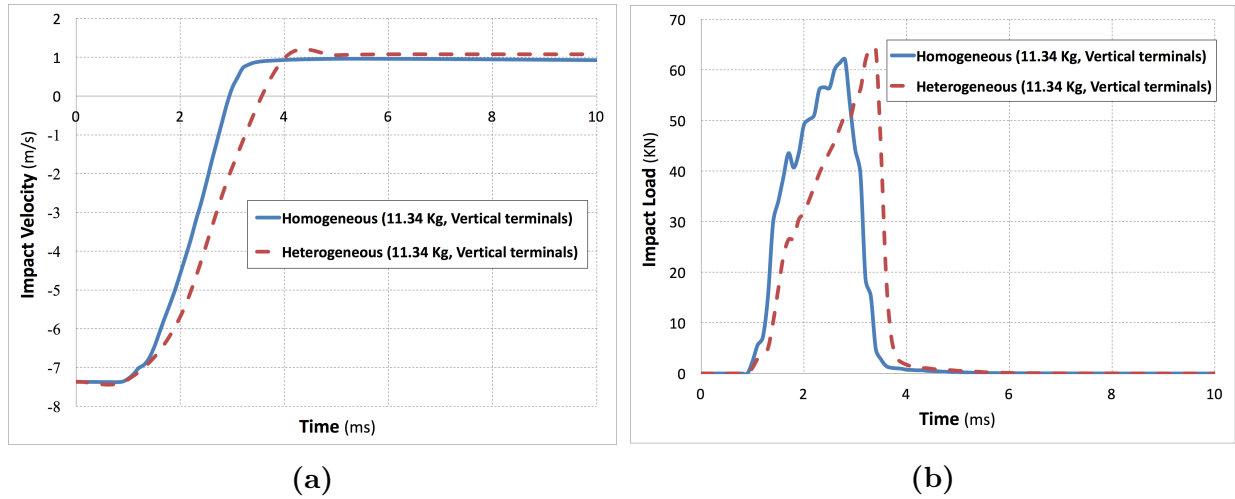


**Figure 4.14:** (a) Change of velocity and (b) Impact force over time for the updated homogeneous and heterogeneous models.

## 4.2 Rod Impact Simulations

A homogeneous and a heterogeneous finite element model were developed in LS-DYNA to simulate rod impact on battery cells (see Fig. 4.15). In the homogeneous model, jellyroll was considered to be homogenized and the stress-strain curve found from compression test of jellyroll layers (Fig. 2.21) was used to define crushable foam material model in LS-DYNA. In the heterogeneous model, jellyroll layers i.e. anode and cathode electrodes and separator, were implemented individually and different stress-strain relations were considered for each layer. Small thickness of the layers and the need for maintaining the aspect ratio of jellyroll elements relatively small to decrease numerical errors lead to a very large number of elements and small time step size. Therefore, the heterogeneous model was solved on an HPC cluster using 184 cores.

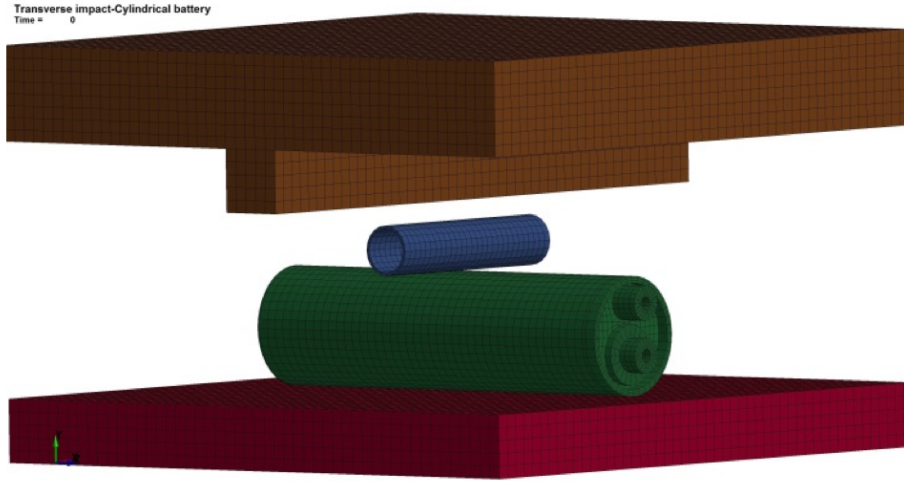


**Figure 4.15:** Rod impact model based on the UN DOT 38.3 requirements.

Similar to the homogeneous model, crushable foam from LS-DYNA material library was utilized as the constitutive model of individual jellyroll layers in the heterogeneous model. Stress-strain relations were derived from compression experiments performed on stacks of individual jellyroll layers using LVDT deflection sensor (Fig. 2.30). In the homogeneous model, jellyroll was divided into 48, 12 and 60 elements in the axial radial and tangential

directions respectively. In the heterogeneous model, each layer was modeled with one solid element in the thickness direction and the element divisions were 300 in axial and tangential directions. In both models, the casing and the center tube were assigned material model 24 (Piecewise linear plasticity) with properties of 1100 aluminum alloy with  $68.9 \text{ GPa}$  modulus of elasticity,  $115 \text{ MPa}$  yield strength and  $125 \text{ MPa}$  ultimate strength properties. The internal spacer between the terminals and the jellyroll was assumed to be made of polyetherimide and modeled in LS-DYNA with material model number 3 (Mat\_plastic\_kinematic).

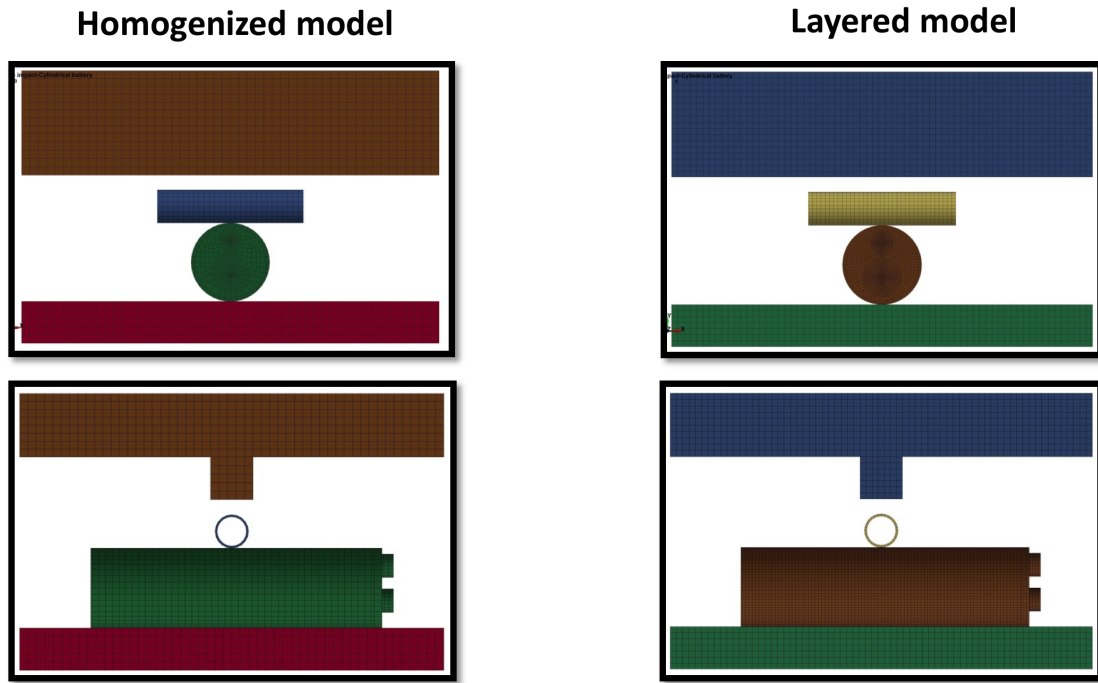


**Figure 4.16:** Homogeneous and heterogeneous models for rod impact simulations.

Both models were meshed with one-point integration elements and hourglass type 6, Belytschko-Bindeman was used to prevent nonphysical, zero-energy deformations [111, 112]. A stationary rigid tube was modeled in contact with the middle of the cell. Two rigid plates were also considered in the model to mimic the ground and the drop cart. The bottom plate was fixed in all directions, while the top plate, with a mass of  $9.1 \text{ kg}$  and an initial velocity of  $3.188 \text{ m/s}$  was allowed to move in the impact direction. The drop velocity was calculated based on the height ( $0.61 \text{ m}$ ) specified in the UN DOT 38.3 requirements assuming an impact

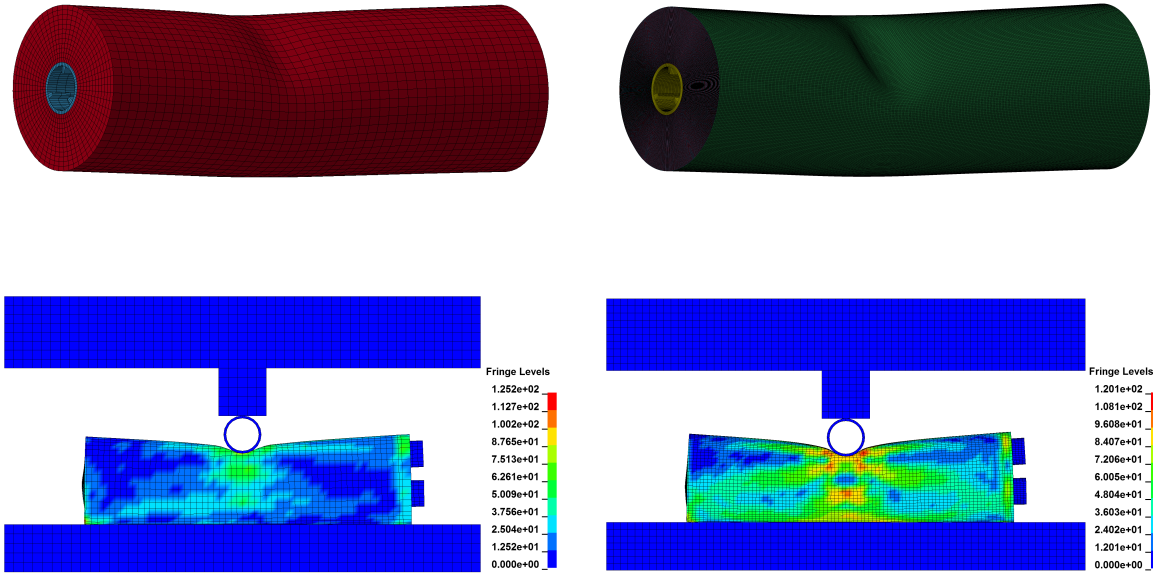
acceleration of  $0.85\ g$  which was measured experimentally using two accelerometers. The homogeneous and heterogeneous models consisted of 80,922 and 21.8 million solid elements respectively (Fig. 4.16). The solution type was transient explicit and lasted 66 minutes using 7 CPUs for the homogeneous model. Solution time for the heterogeneous model was about 41 hours on an HPC cluster using 184 cores and 3 GB memory per core. Table 4.6 lists the simulation data for both of the impact models.

Fig. 4.17a and b demonstrate how jellyroll was deformed under impact in homogeneous and heterogeneous simulations respectively. Also, Von-Mises stress contours during impact are depicted in Fig. 4.17c and 4.17d. They show how the stresses are beyond aluminum's yield strength causing plastic deformations in the casing. Similar to flat-plate impact simulations, impact velocity and impact force are plotted in Fig. 4.18. Impact velocity changes from  $3.19\ m/s$  in the downward direction to about  $0.5\ m/s$  in the upward direction. From the impact load curves, duration of impact is estimated to be about  $6\ ms$  and maximum impact force for both homogeneous and heterogeneous models is  $13.5\ kN$ . Values of the cell's deformed thickness after impact are listed in Table 4.7. Comparison with the experimentally measured data shows that the homogeneous model predicted the cell's deformations with a negligible error. For the heterogeneous model, the error was less than 4%.

**Table 4.6:** Simulation data for rod impact analysis models.

Simulation data	Homogeneous model	Heterogeneous model
Number of elements	80,922	21.8 million
Number of nodes	98,028	22 million
Number of parts	7	9
Analysis type	Transient explicit	Transient explicit
Solution time	66 minutes	41 hours
Number of cores	7	184





**Figure 4.17:** Deformed jellyrolls and Von-Mises stress contours found from homogeneous and heterogeneous simulations.

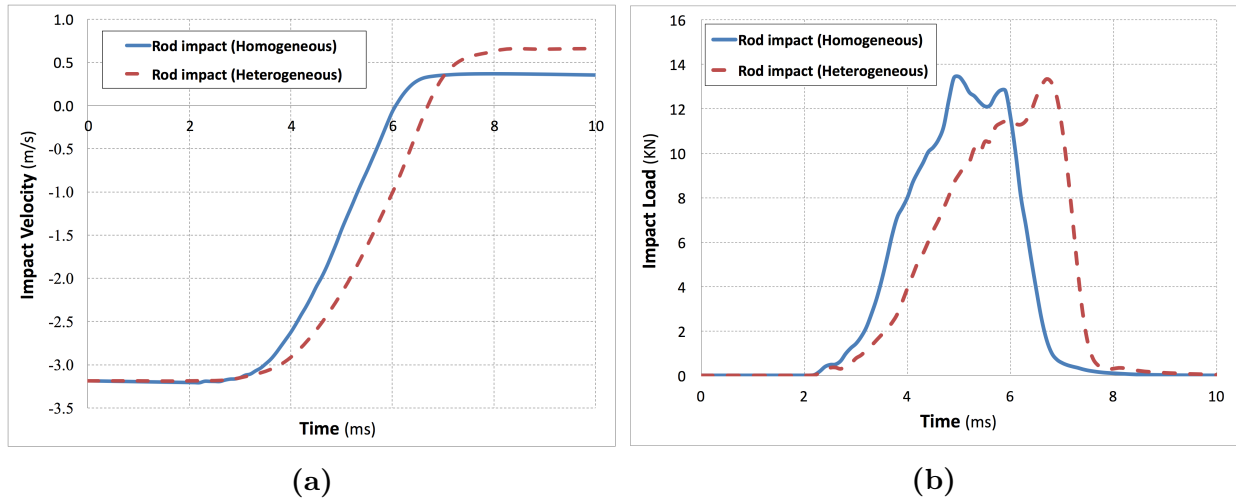


**Figure 4.18:** (a) Change of velocity and (b) Impact force over time for rod impact simulations.

**Table 4.7:** Cell's deformed thickness after impact by a rigid rod.

	Cell thickness ( <i>mm</i> )	Error (%)
Experiment	30.55	—
FE (Homogeneous)	30.6	0.16
FE (Heterogeneous)	29.4	3.76

### 4.3 Rod Indentation Simulations

Previously developed heterogeneous finite element model was slightly modified and used for quasi-static rod indentation simulation. The upper rigid plate (impacting plate) was removed from the model as depicted in Fig. 4.19. The rigid tube was assigned a constant velocity of  $2 \text{ mm/min}$  and pressed against the cell casing. The bottom rigid plate was fixed in all degrees of freedom to resemble the fixed end of the testing machine. Similar to the rod impact simulations, crushable foam material model from LS-DYNA material library was chosen for anode, cathode and separator layers incorporating stress-strain curves found from compression experiments using LVDT deflection sensor (Fig. 2.30). Transient explicit simulation was conducted using MPP version of LS-DYNA on an HPC cluster with 184 cores and 3 GB of memory per core. The model consisted of about 22 million solid elements and the solution time was about 104 hours.

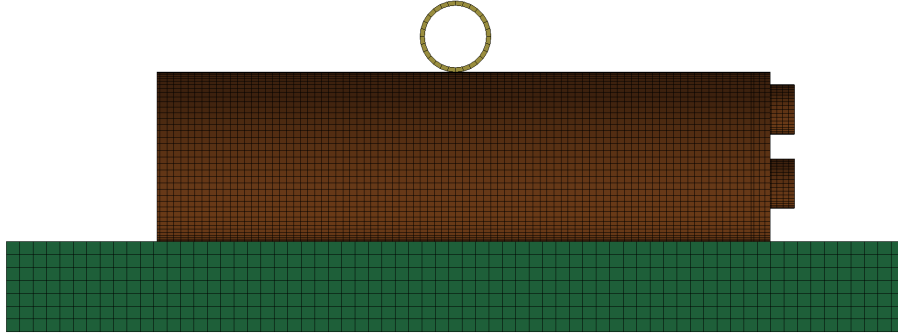


**Figure 4.19:** Heterogeneous model for rod indentation simulation.

The load transferred through the contact between the tube and the casing was recorded at predefined intervals. The resulting load-displacement curve is plotted in Fig. 4.20 and is compared to the curves measured found from indentation experiments. Results show that the heterogeneous rod indentation simulation can predict the loads measured during experiments quite accurately, especially for higher load levels. The load causing mechanical failure was found to be  $67 \text{ kN}$  which is also within the range of  $64\text{-}68 \text{ kN}$  measured for the

experiments. A cross section of jellyroll under maximum deformation is displayed in Fig. 4.21. The deformed shape shows highly distorted layers on each side of the center tube. Similar distortions were observed in the experiments through CT-scanning and microscopy of crushed cells. Von-Mises stress contour for the casing is plotted in Fig. 4.22. High-stressed areas are the locations where the casing undergoes plastic deformation.

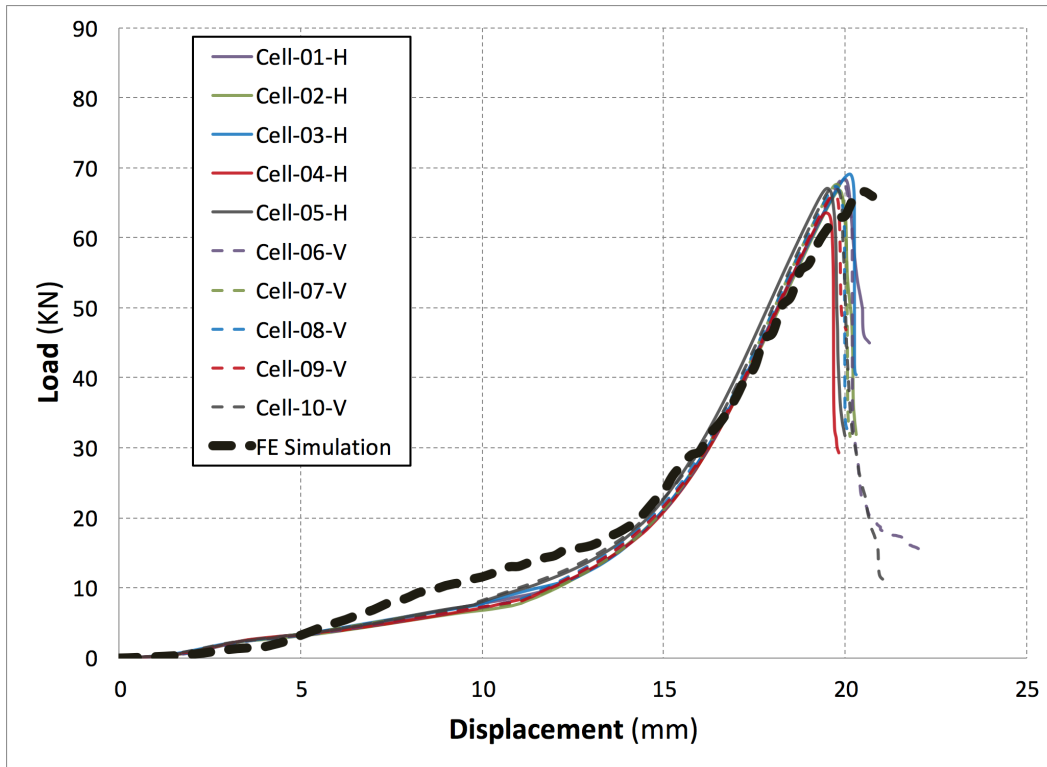


**Figure 4.20:** Load-displacement curves found from rod indentation experiments and finite element simulation.

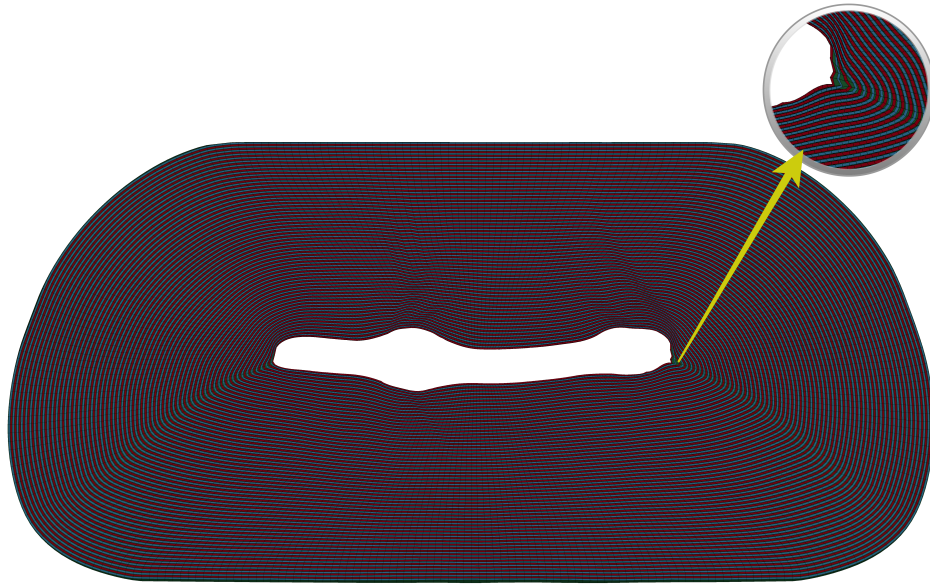


**Figure 4.21:** Cross section of jellyroll found from rod indentation simulation.

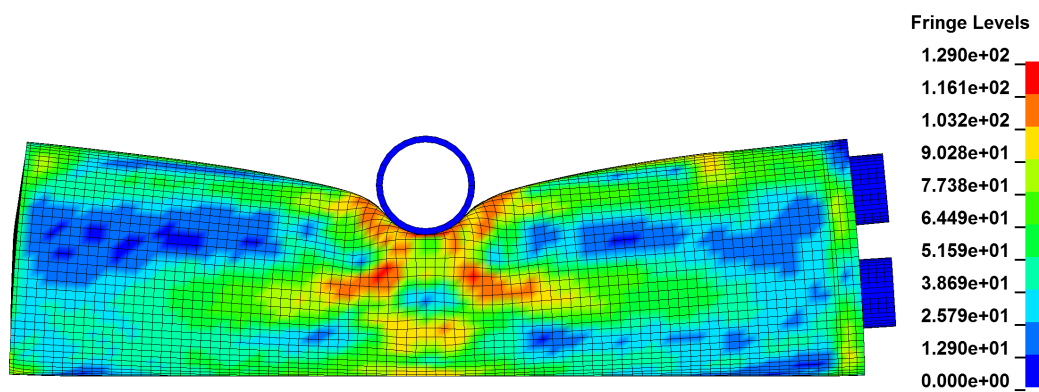


**Figure 4.22:** Von-Mises stress contour for the cell casing found from rod indentation simulation.

---

## Chapter 5

### Module Level: Multi-Scale Finite Element Simulation

#### 5.1 Finite Element Model of PM12 Module

In a battery pack used in electric vehicles, cells are placed in modules and therefore, modeling impact on individual cells will not represent the real-life impacts that might occur when an electric vehicle is in an accident. Thus, a finite element model of PM12 module was also developed so that impact can also be studied on a module including 12 cylindrical cells. A single heterogeneous cell model (Fig. 5.2b) takes several days to be solved on an HPC cluster using 200 cores. Therefore, it is almost impossible to include 12 heterogeneous cells in a model with a reasonable solution time. However, it is possible to simulate impact on battery modules consisting of homogeneous cells and later apply the obtained deformations to the cell/cells of interest that incorporate individual jellyroll layers. A multi-scale framework has been developed and is described in more details in Section 5.2. Jellyroll homogenization was performed in Chapter 2 and the homogeneous cell model was validated using experiments in the previous chapter. Thus it will be a reasonable approach to use homogeneous cell models in a battery module to decrease the solution time and still get the same impact response as heterogeneous cells models. The approach is shown in Fig. 5.1 schematically. Jellyroll was characterized and homogenized experimentally which leads to developing a homogeneous finite element model (Fig. 5.2a) of cylindrical cell. The impact model was solved explicitly and drop-test results validated the homogenization approach and simulations. The homogeneous cell model can now be used as batteries inside a complete finite element model of a battery module.

The battery module is made of glass-fiber-reinforced polypropylene (PP-GF40). Because

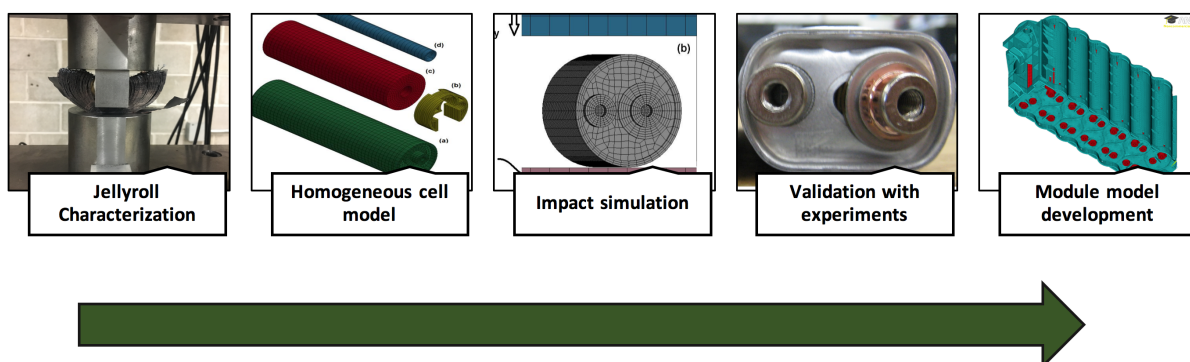


**Figure 5.1:** The process of developing battery module finite element model.

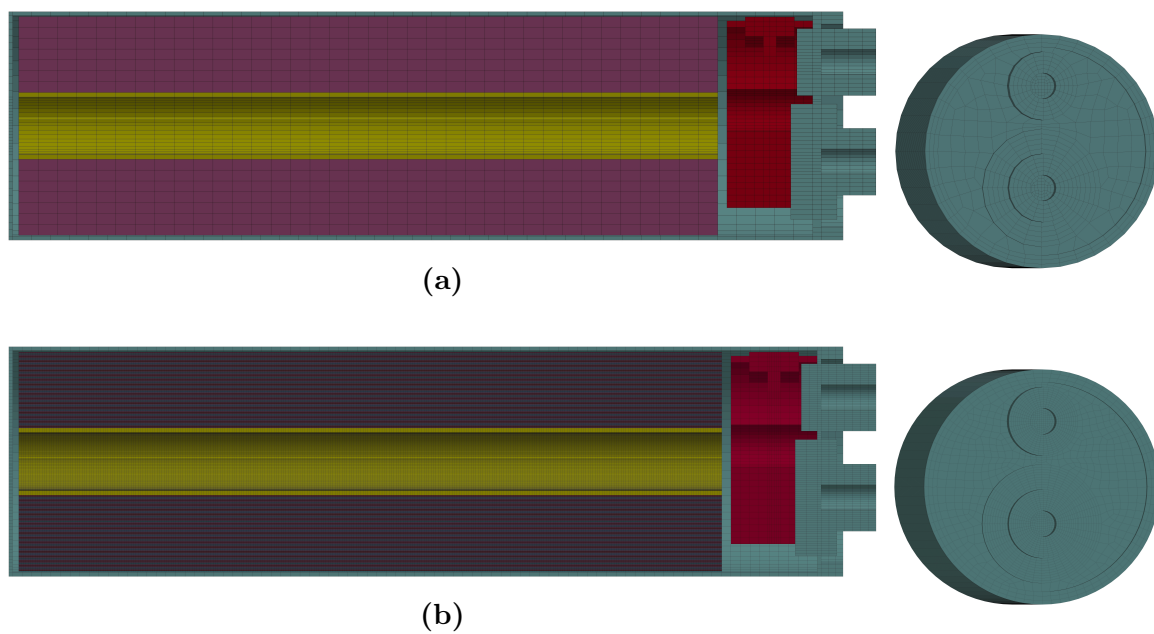


**Figure 5.2:** (a) Homogeneous cell model and (b) Heterogeneous cell model.

of its relatively small thickness, shell elements were used to model the module. Although it is made of two parts (the module itself and the top cover), the finite element model was considered to be a single part because the cover will be completely fitted into the module body and they will be bonded at multiple locations. 241,600 shell elements with thicknesses changing from 1.4 to 3.2 *mm* were used to model the module. Material model 3 (Mat\_plastic\_kinematic) from LS-DYNA library was chosen with an elastic modulus of 7.85 *GPa*, tensile strength of 96 *MPa* and maximum elongation of 1.85%. Similar to all of the other finite element models in this study, module's geometry and elements were generated using ANSYS APDL before they were transferred to LS-DYNA using a custom-developed APDL macro. Fig. 5.3 shows a module containing 12 cylindrical cells of type 6P and the finite element model of the module including homogeneous cylindrical cells is depicted in Fig. 5.4. Surface-to-surface contacts were defined between each cell's casing and the module to prevent any interference between them during impact. There were also contacts between all of the adjacent casings.

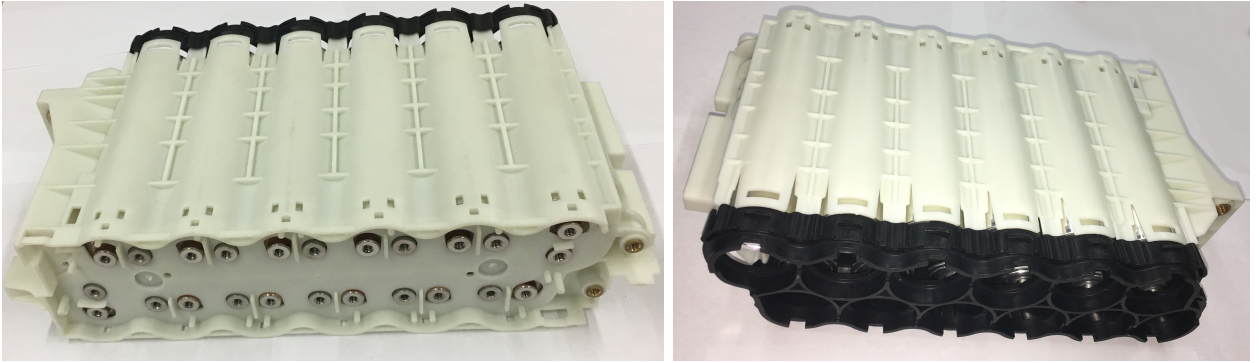


**Figure 5.3:** PM12 module containing 12 6P cylindrical cells.

## 5.2 Multiscale Simulation Scheme

The goal in simulating impact on lithium-ion batteries is to improve their safety by finding the critical points with a high risk of short circuit occurrence due to excessive deformation of cells during accidents. This cannot be accomplished by only using a module consisting of ho-



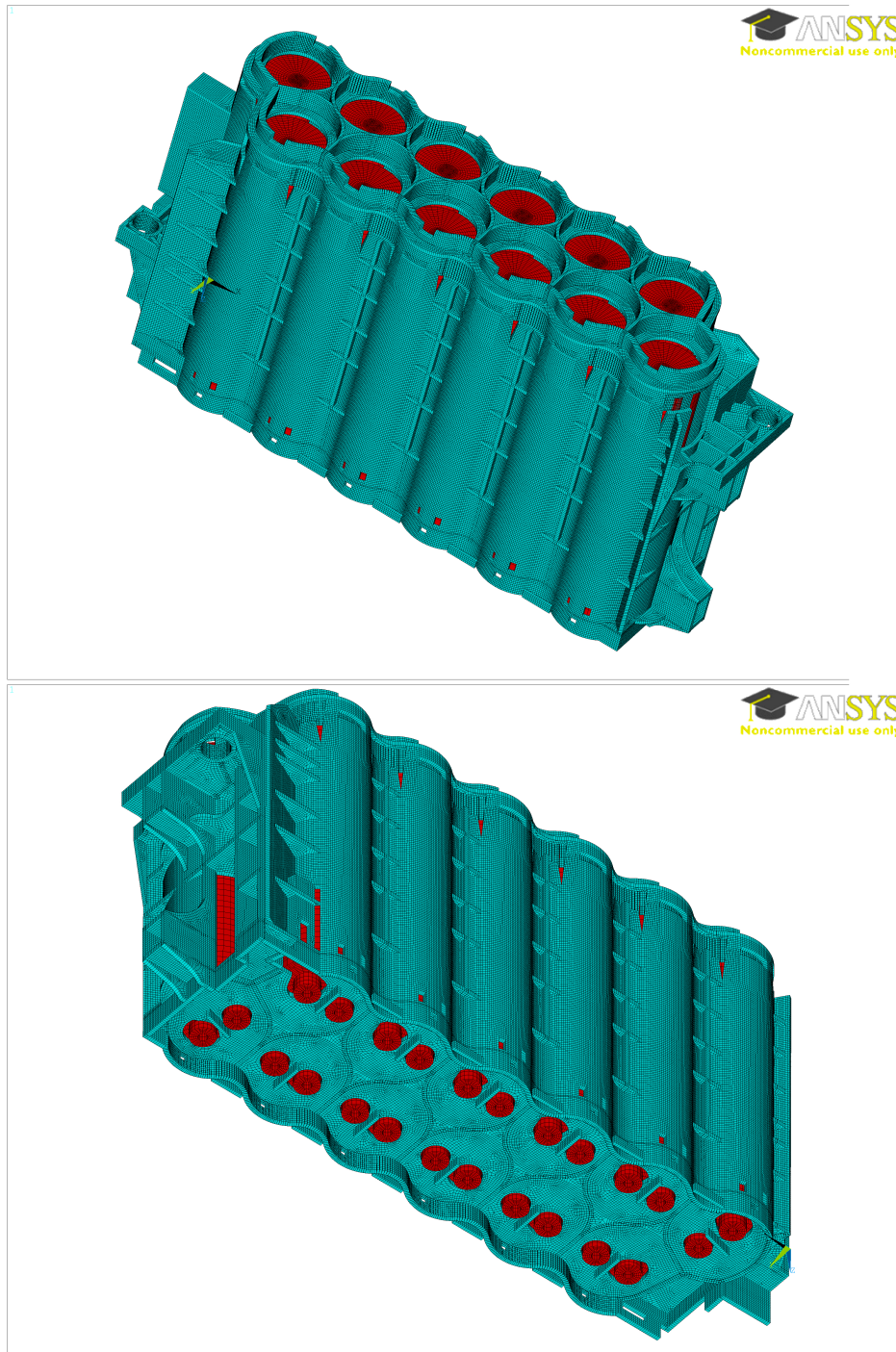


**Figure 5.4:** Finite element model of a PM12 module including homogeneous cells.

homogeneous cell models because in a homogeneous jellyroll, current collectors and separators are all grouped as a single material. In order to find the locations of potential short circuit, we need to monitor thickness change in individual jellyroll layers specially separators. This, calls for a heterogeneous model that accounts for anode, cathode and separator layers. Since replacing all of the homogeneous cell models in a battery module with heterogeneous models will be computationally very expensive, a multi-scale simulation approach is proposed that is computationally inexpensive and also accounts for individual layers of jellyroll.

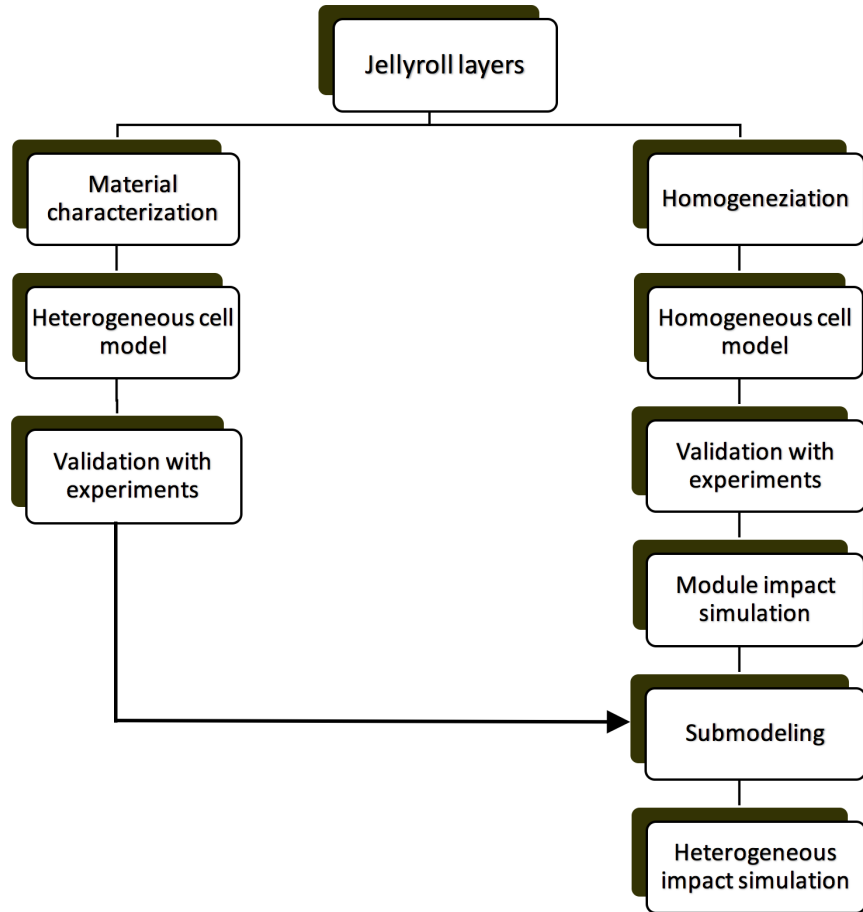


**Figure 5.5:** The process of multiscale simulation of impact on battery module.

The proposed multi-scale approach, schematically shown in Fig. 5.5, has several steps. Starting with jellyroll layers of the battery under study, homogenization is performed on jellyroll that leads to developing a homogeneous finite element model of the cell. Cells are then incorporated in a module or pack and are solved under impact or crush loads of interest.

The critical cell with the highest amount of deformation is then chosen to look into in more details using a submodel. For the selected cell, displacement and velocity time histories for the boundaries of the homogenized jellyroll are saved in a file at previously specified intervals. In a subsequent analysis, the stored time-history data is used to apply equivalent displacements to the boundaries of a heterogeneous jellyroll model. Therefore, in the second analysis instead of having the entire module with all the cells, only one heterogeneous jellyroll will be solved with the same deformation history of the homogenized jellyroll. For this step, the sub-modeling (interface) feature of LS-DYNA is used. This sub-modeling feature is a two-step process: the first analysis is done using `Interface.component` keyword and the second analysis uses `Interface.linking` keyword in LS-DYNA. Fig. 5.6 shows the jellyroll boundaries for which displacement and velocity time-histories were recorded. The boundary consists of the interface between jellyroll and inner tube, the outer surface and the top and bottom segments. No relevant standard could be found for impact testing requirements of

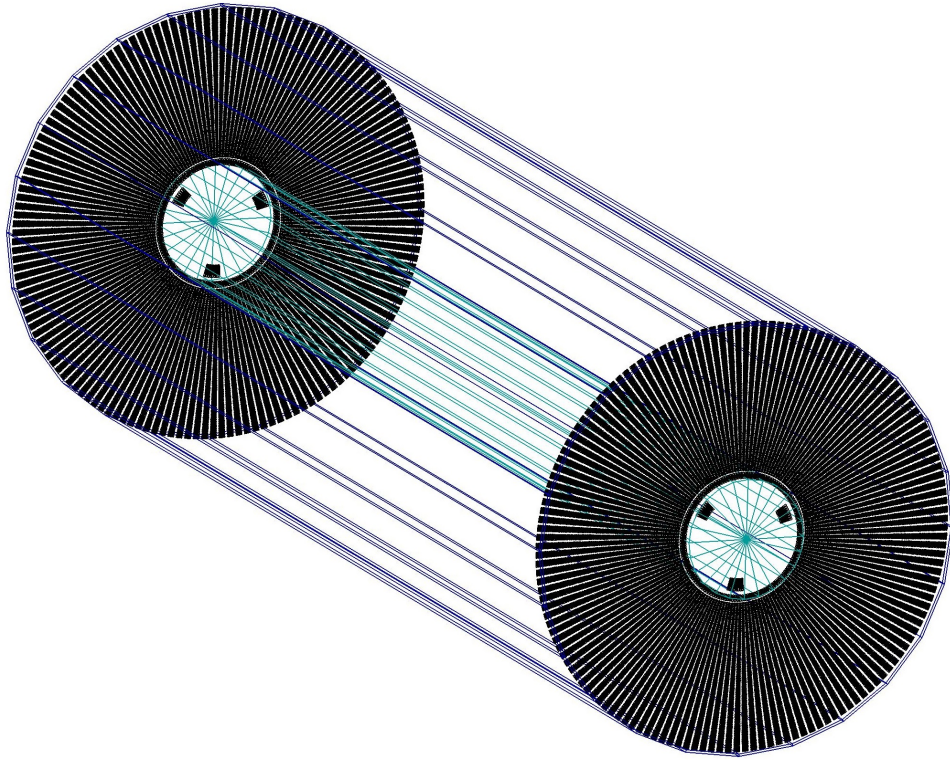


**Figure 5.6:** Cell boundary segments used for storing displacements data for submodeling.

battery modules. An arbitrary impact weight and velocity was chosen to conduct an impact simulation as a proof of concept. The battery module was placed on a rigid plate and another rigid plate with a mass of  $22.7\text{ kg}$  ( $50\text{ lbs}$ ) and an initial velocity  $7.37\text{ m/s}$  dropped onto the module and the cells. All of the deformed cells were checked and the most deformed one was chosen as the critical cell (see Fig. 5.7). The boundaries of the jellyroll of the critical cell was specified in LS-DYNA (illustrated in Fig. 5.6) and the solution was repeated so that displacement and velocity time histories of the boundary can be recorded. By considering the jellyroll and not the cell itself as the sub-model, several contact commands were eliminated and similar deformation on the jellyroll was obtained in a shorter solution time. The module impact model with 1.5 million solid elements and 241,600 shell elements was solved on an HPC cluster using 96 cores and the solution time was 10 hours.

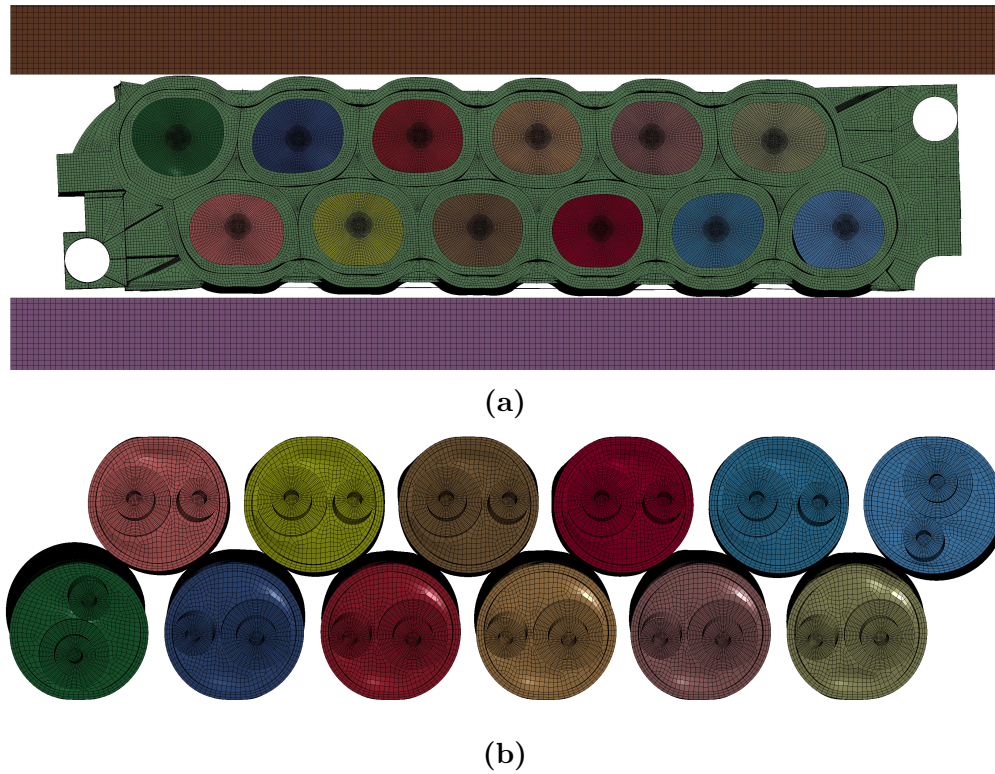


**Figure 5.7:** Deformed shape of the module including 12 homogenized cells.

For the purpose of this study, one of the middle cells in the bottom was selected as the critical cell. Fig. 5.8a shows the deformed shape of jellyroll and aluminum core of the chosen



cell that was obtained from the module impact simulation (i.e. Fig. 5.7). After running the second simulation, sub-modeling was conducted on the heterogeneous cell, resulting in the same overall deformation of the jellyroll. The subsequent solution was also solved on an HPC cluster using 192 cores and the solution time was 33 hours for a model with 22 million solid elements. Using the results from the heterogeneous jellyroll model, depicted in Fig. 5.8b, deformation of each individual jellyroll layer can be studied. The most important cause of internal short circuit and the subsequent thermal runaway is known to be separator thinning and separator failure. A plot similar to Fig. 4.11 can be derived to study the change of through-the-thickness strain in separator layers based on their radial location.

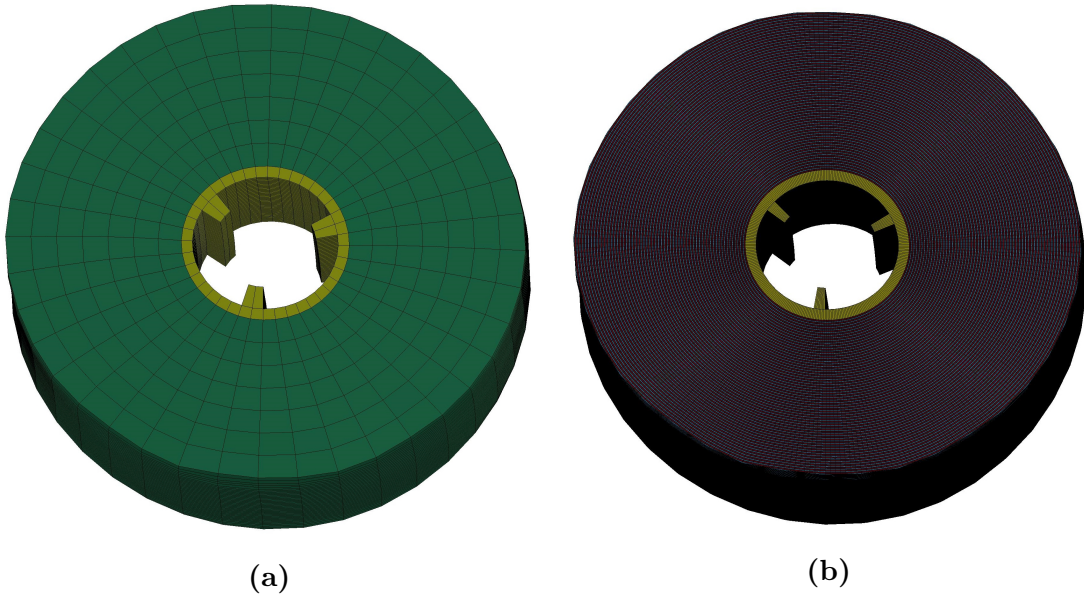


**Figure 5.8:** (a) Deformed shape of a homogeneous jellyroll after impact on the module and (b) Deformed shape of the equivalent heterogeneous model.

---

## Chapter 6

### Conclusions

We have carried out experimental and numerical characterization of the mechanical response of cylindrical lithium-ion battery cells used in EV/HEV applications to lateral impact, rod impact and rod indentations. Highly nonlinear mechanical deformations were characterized experimentally using high-speed camera, computed tomography analysis and optical microscopy of the deformed samples. Numerically, we have investigated feasibility of using commercial explicit finite element software LS-DYNA for accurate modeling of impact in one cell as well as in a battery module consisting of 12 cells. The proposed homogenization methodology coupled with the developed explicit finite element model can be applied to modeling live cells and battery packs subject to impact, which can be used as an effective design tool for batteries. It can also give insight into catastrophic failure prevention for EV/HEV battery packs due to impact. The following conclusions can be drawn from the results of this study:

#### 6.1 Jellyroll Characterization/Homogenization

- Two proposed homogenization methods for the jellyroll in a cylindrical lithium-ion battery cell produced similar mechanical response of the homogenized material for relatively small strains. However, for the strains larger than 0.1, the difference between the two material models would gradually increase and was as large as 25% for a strain level of 0.3.
- The virtual work method of homogenization can be accurate for smaller cells, while for larger cells, such as 6P-JCI cells, the direct experimental homogenization using flat



samples is the preferred method of determining the effective material properties of the jellyroll.

- A series of experiments were carried out to find the compressive properties of the jellyroll saturated in DMC solvent. Comparison with previous results for the dry jellyroll showed that DMC solvent does not significantly change the resulting stress-strain relation.
- Individual layers of the jellyroll were also tested under lateral compression to find their constitutive behavior. Based on the resulting stress-strain curves, coated copper layers were twice as stiff as coated aluminum layers and separator layers had a significantly smaller share in the total jellyroll's compressive stiffness.
- Previous jellyroll dry/wet compression tests were repeated using an Instron 5985 testing machine with a 250  $kN$  load cell to achieve higher strain levels and the LVDT deflection sensor to obtain more accurate displacement measurements. The new results proved again that existence of DMC solvent has negligible effects on the jellyroll's stress-strain curve. The only difference was that the experiments using LVDT showed a slightly higher stiffness for saturated samples while in previous tests, dry jellyroll samples seemed to have a higher stiffness.
- Effects of DMC electrolyte solvent on individual layers' stress-strain curves were also studied. When DMC solvent is present, all of the three types of jellyroll layers, i.e. anode, cathode and separator, fail at lower stress values compared to dry conditions. Separator layers and coated aluminum layers have an overall higher stiffness when there is no electrolyte solvent. However, for coated copper layers, DMC solvent seems to inversely affect the mechanical properties and there is a higher stiffness for saturated samples before failure.
- Jellyroll compression tests were conducted at different rates to study the strain-rate

dependence of the jellyroll's mechanical properties. Comparing the obtained stress-strain curves showed that the rate of applying the load did not significantly change the jellyroll's stiffness. The jellyroll gets slightly stiffer when the displacement is increased to  $8\text{ mm/min}$  while, for larger strain-rates, the stiffness drops marginally.

- Scanning electron microscopy was used to study pore closure behavior of separator layers under compression. SEM images showed that the number of pores dropped significantly when the compressive load increased. Pore size also linearly declined with higher through-the-thickness load.

## 6.2 Cell Level: Impact and Indentation Experiments

- Battery cells were impact tested using a drop test apparatus where a rigid drop cart was dropped onto a stationary cell. Cells were tested using  $11.34\text{ kg}$  and  $22.68\text{ kg}$  drop weights, each in two orientations where the cell terminals were aligned in vertical or horizontal directions. The experiments showed that cell orientation does not make a significant difference in the overall deformation of the cell and jellyroll.
- A 3-D finite element model of the cell was developed using the crushable foam material model utilizing experimentally obtained effective material properties for the jellyroll. Explicit impact simulations were conducted using LS-DYNA. The deformed shape of the cell found from simulations was in good agreement with the experimental measurements. Impact load and velocity was derived from the finite element analysis and the impact time was estimated to be 3 and 4  $ms$  for  $11.34\text{ kg}$  and  $22.68\text{ kg}$  drop tests, respectively.
- A heterogeneous finite element model of the jellyroll was developed in LS-DYNA to simulate behavior of the cell under lateral impact between two rigid plates. Stress-strain properties found from the experiments were incorporated into the finite element

model.

- Deformed shape, impact velocity and impact load from the heterogeneous simulation were compared to the results found from the homogeneous simulation and CT-scans of previous experiments and validated the finite element model.
- A steel rod of diameter 15.8 *mm* was placed across the center of the cell and a 9.07 *kg* drop-cart released from a height of 0.635 *m* to impact the bar based on UN DOT 38.3 requirements. For the second test, the drop height was increased to 2.76 *m*, the maximum capacity of the drop-test apparatus. The final experiment included a cell experiencing an impact from the maximum height with a drop-mass of 14.15 *kg*. Resistance between the terminals was measured for all three samples using a multimeter. No short circuit was detected in the samples.
- Drop duration and acceleration was measured accurately using two accelerometers/shock sensors attached to the drop cart. The sensor data showed an acceleration of 0.85*g*, 0.76*g* and 0.80*g* for the impact samples A, B and C respectively, which means there were velocity losses due to friction and probably trapped air below the drop cart in the enclosed test section.
- 10 samples (5 horizontal and 5 vertical terminals) were tested under steady compression where the sample was placed on the fixed end of a universal testing machine and the moving end pressed against a 15.8 *mm* steel rod on the center of the cell. Load-displacement curves showed similar results for vertical and horizontal orientations. The results showed that mechanical failure occurs at about 64-68 *kN* and 19-20 *mm* indentation, regardless of terminal orientation.
- The cells were connected to a simple circuit and a power supply to monitor any resistance and voltage changes during the steady compression tests. Measurements showed that a short circuit occurred at an indentation distance of 17.5-19 *mm*. There was

no obvious correlation between the orientation of cell terminals and the short circuit occurrence level.

- The cross section of crushed samples was studied with optical microscopy using magnification factors of  $6.5x$  to  $200x$ . Jellyroll layers were highly distorted on the left and right sides of battery's aluminum core. The layers adjacent to the testing machine compression platens were highly compressed, resulting in thin separator layers. Contact between the anode and cathode was observed in a sample tested under steady indentation. Also, a crack in one of the copper layers near the aluminum core had been developed likely due to high tensile loads.
- Homogeneous and heterogeneous finite element models were developed in LS-DYNA to simulate rod impact and steady indentation experiments. The heterogeneous model could predict an overall load-displacement curve similar to the indentation test results. Deformation found from the heterogeneous model showed the same distortions observed in the layers through microscopy.

### 6.3 Module Level: Multi-Scale Simulation

- The goal of this work was to develop a multi-scale finite element framework to study impact on lithium-ion modules. A PM12 module, consisting of 12 6P cylindrical cells, both manufactured by Johnson Controls Inc., was considered for this simulation.
- A finite element model of PM12 battery module was developed. Assembly of the module and 12 homogenized cell models were analyzed under impact between two rigid plates. Among the deformed cells, the one with highest amount of deformation was chosen as the critical cell.
- For the critical cell, surrounding areas of the jellyroll were considered as the sub-model boundary. The module impact solution was repeated to save displacement and velocity

time histories of the sub-model boundary.

- The recorded displacements and velocities were transferred to a heterogeneous jellyroll model and after solving the model, an overall deformation similar to the one for homogenized jellyroll model was obtained. The results from the heterogeneous model could potentially show deformations, stresses and strains of individual jellyroll layers.

## 6.4 Future Work

The present work can be improved and further extended in various aspects. The following ideas are some pathways for future research in this area:

- In order to better understand thermal runaway phenomenon, thermal analysis can be conducted in the cell and module levels. Effects of impact and deformations on heat generation inside the cell can be studied.
- A multi-physics (structural-thermal-electrochemical) finite element simulation can provide more insight into the behavior of lithium-ion batteries under abnormal conditions.
- The proposed multi-scale simulation approach can be scaled up to battery packs and scaled down to several jellyroll layers.
- When proper safety provisions are considered, the proposed approach can be used to test live battery cells with real-time monitoring of relevant data such as temperature, voltage and etc.
- A generalized set of characterization experiments can be performed on jellyroll layers to find their mechanical properties in all direction. This will help use anisotropic material models which are better suited for jellyroll layers.
- Impact and compression tests and simulations can be conducted in the axial directions to study buckling and wrinkling behaviors of casing and jellyroll layers.

---

## BIBLIOGRAPHY

- [1] Celina Mikolajczak, Michael Kahn, Kevin White, and Richard Thomas Long. Lithium-ion batteries hazard and use assessment. Technical report, The Fire Protection Research Foundation, 2011.
- [2] Mohammad Hasan Balali, Narjes Nouri, Emad Omrani, Adel Nasiri, and Wilkistar Otieno. An overview of the environmental, economic, and material developments of the solar and wind sources coupled with the energy storage systems. *International Journal of Energy Research*, 2017.
- [3] P. G. Balakrishnan, R. Ramesh, and T. Prem Kumar. Safety mechanisms in lithium-ion batteries. *Journal of Power Sources*, 155(2):401–414, 2006.
- [4] David Herron. chevy volt battery pack fire in 2011. <https://greentransportation.info/ev-ownership/safer/chevy-volt-battery-pack-fire-2011.html>. (accessed May 25, 2017).
- [5] B. Smith. Chevrolet volt battery incident summary report. Technical report, National Highway Traffic Safety Administration, 2012.
- [6] Nelson Ireson. Third tesla model s fire: Still not a big deal. [http://www.motorauthority.com/news/1088270\\_third-tesla-model-s-fire-still-not-a-big-deal](http://www.motorauthority.com/news/1088270_third-tesla-model-s-fire-still-not-a-big-deal). (accessed May 24, 2017).
- [7] PETE CAREY. 2013: Tesla battery fires spark federal safety probe. <http://www.mercurynews.com/2013/11/19/2013-tesla-battery-fires-spark-federal-safety-probe>. (accessed May 24, 2017).



- [8] Anna Shedletsky. Aggressive design caused samsung galaxy note 7 battery explosions. <https://www.instrumental.ai/blog/2016/12/1/aggressive-design-caused-samsung-galaxy-note-7-battery-explosions>. (accessed May 25, 2017).
- [9] D. H. Doughty and A. A. Pesaran. Vehicle battery safety roadmap guidance. Technical report, National Renewable Energy Laboratory, 2012.
- [10] Xuan Liu, Stanislav I. Stoliarov, Matthew Denlinger, Alvaro Masias, and Kent Snyder. Comprehensive calorimetry of the thermally-induced failure of a lithium ion battery. *Journal of Power Sources*, 280:516–525, 2015.
- [11] Robert M. Spotnitz, James Weaver, Gowri Yeduvaka, D. H. Doughty, and E. P. Roth. Simulation of abuse tolerance of lithium-ion battery packs. *Journal of Power Sources*, 163:1080–1086, 2007.
- [12] A. Smyshlyaev, M. Krstic, N. Chaturvedi, J. Ahmed, and A. Kojic. PDE model for thermal dynamics of a large Li-ion battery pack. In *Proceedings of the 2011 American Control Conference*, pages 959–964, 2011.
- [13] Joshua Lamb, Christopher J. Orendorff, Leigh Anna M. Steele, and Scott W. Spangler. Failure propagation in multi-cell lithium ion batteries. *Journal of Power Sources*, 283:517–523, 2015.
- [14] Xuning Feng, Jing Sun, Minggao Ouyang, Fang Wang, Xiangming He, Languang Lu, and Huei Peng. Characterization of penetration induced thermal runaway propagation process within a large format lithium ion battery module. *Journal of Power Sources*, 275:261–273, 2015.
- [15] Neil S. Spinner, Christopher R. Field, Mark H. Hammond, Bradley A. Williams, Kristina M. Myers, Adam L. Lubrano, Susan L. Rose-Pehrsson, and Steven G. Tuttle. Physical and chemical analysis of lithium-ion battery cell-to-cell failure events inside custom fire chamber. *Journal of Power Sources*, 279:713–721, 2015.

- [16] Qingsong Wang, Ping Ping, Xuejuan Zhao, Guanquan Chu, Jinhua Sun, and Chunhua Chen. Thermal runaway caused fire and explosion of lithium ion battery. *Journal of Power Sources*, 208:210–224, 2012.
- [17] Languang Lu, Xuebing Han, Jianqiu Li, Jianfeng Hua, and Minggao Ouyang. A review on the key issues for lithium-ion battery management in electric vehicles. *Journal of Power Sources*, 226:272–288, 2013.
- [18] Seyed Mohammad Rezvanizani, Zongchang Liu, Yan Chen, and Jay Lee. Review and recent advances in battery health monitoring and prognostics technologies for electric vehicle (EV) safety and mobility. *Journal of Power Sources*, 256:110–124, 2014.
- [19] Wladislaw Waag, Christian Fleischer, and Dirk Uwe Sauer. Critical review of the methods for monitoring of lithium-ion batteries in electric and hybrid vehicles. *Journal of Power Sources*, 258:321–339, 2014.
- [20] Alexander Farmann, Wladislaw Waag, Andrea Marongiu, and Dirk Uwe Sauer. Critical review of on-board capacity estimation techniques for lithium-ion batteries in electric and hybrid electric vehicles. *Journal of Power Sources*, 281:114–130, 2015.
- [21] J. Nunes-Pereira, C. M. Costa, and S. Lanceros-Mendez. Polymer composites and blends for battery separators: State of the art, challenges and future trends. *Journal of Power Sources*, 281:378–398, 2015.
- [22] Gi-Heon Kim, Ahmad Pesaran, and Robert Spotnitz. A three-dimensional thermal abuse model for lithium-ion cells. *Journal of Power Sources*, 170:476–489, 2007.
- [23] Sun Ung Kim, Paul Albertus, David Cook, Charles W. Monroe, and Jake Christensen. Thermoelectrochemical simulations of performance and abuse in 50-Ah automotive cells. *Journal of Power Sources*, 268:625–633, 2014.

- [24] Gi-Heon Kim, Kandler Smith, John Ireland, and Ahmad Pesaran. Fail-safe design for large capacity lithium-ion battery systems. *Journal of Power Sources*, 210:243–253, 2012.
- [25] Ion C. Halalay, Michael J. Lukitsch, Michael P. Balogh, and Curtis A. Wong. Nanoin-dentation testing of separators for lithium-ion batteries. *Journal of Power Sources*, 238:469–477, 2013.
- [26] Azadeh Sheidaei, Xinran Xiao, Xiaosong Huang, and Jonathon Hitt. Mechanical behavior of a battery separator in electrolyte solutions. *Journal of Power Sources*, 196(20):8728–8734, 2011.
- [27] Ilya Avdeev, Michael Martinsen, and Alex Francis. Rate- and temperature-dependent material behavior of a multilayer polymer battery separator. *Journal of Materials Engineering and Performance*, 23:315–325, 2014.
- [28] Ilya Avdeev and Mehdi Gilaki. Structural analysis and experimental characterization of cylindrical lithium-ion battery cells subject to lateral impact. *Journal of Power Sources*, 271:382–391, 2014.
- [29] Mehdi Gilaki and Ilya Avdeev. Impact modeling of cylindrical lithium-ion battery cells: a heterogeneous approach. *Journal of Power Sources*, 328:443–451, 2016.
- [30] Joshua Lamb and Christopher J. Orendorff. Evaluation of mechanical abuse techniques in lithium ion batteries. *Journal of Power Sources*, 247:189–196, 2014.
- [31] Xiaowei Zhang and Tomasz Wierzbicki. Characterization of plasticity and fracture of shell casing of lithium-ion cylindrical battery. *Journal of Power Sources*, 280:47–56, 2015.
- [32] Long Lam, P. Bauer, and E. Kelder. A practical circuit-based model for Li-ion battery

- cells in electric vehicle applications. In *2011 IEEE 33rd International Telecommunications Energy Conference (INTELEC)*, pages 1–9, 2011.
- [33] John B. Goodenough and Youngsik Kim. Challenges for Rechargeable Li Batteries. *Chemistry of Materials*, 22:587–603, 2010.
- [34] Doron Aurbach, Ella Zinigrad, Yaron Cohen, and Hanan Teller. A short review of failure mechanisms of lithium metal and lithiated graphite anodes in liquid electrolyte solutions. *Solid State Ionics*, 148:405–416, 2002.
- [35] Yufei Chen and James W. Evans. Heat Transfer Phenomena in Lithium/Polymer-Electrolyte Batteries for Electric Vehicle Application. *Journal of The Electrochemical Society*, 140:1833–1838, 1993.
- [36] S. C. Chen, C. C. Wan, and Y. Y. Wang. Thermal analysis of lithium-ion batteries. *Journal of Power Sources*, 140:111–124, 2005.
- [37] Kandler Smith and Chao-Yang Wang. Power and thermal characterization of a lithium-ion battery pack for hybrid-electric vehicles. *Journal of Power Sources*, 160:662–673, 2006.
- [38] Y. Inui, Y. Kobayashi, Y. Watanabe, Y. Watase, and Y. Kitamura. Simulation of temperature distribution in cylindrical and prismatic lithium ion secondary batteries. *Energy Conversion and Management*, 48:2103–2109, 2007.
- [39] Xiongwen Zhang. Thermal analysis of a cylindrical lithium-ion battery. *Electrochimica Acta*, 56:1246–1255, 2011.
- [40] Kazuo Onda, Hisashi Kameyama, Takeshi Hanamoto, and Kohei Ito. Experimental Study on Heat Generation Behavior of Small Lithium-Ion Secondary Batteries. *Journal of The Electrochemical Society*, 150:A285–A291, 2003.

- [41] X. Lin, A. G. Stefanopoulou, H. E. Perez, J. B. Siegel, Y. Li, and R. D. Anderson. Quadruple adaptive observer of the core temperature in cylindrical Li-ion batteries and their health monitoring. In *2012 American Control Conference (ACC)*, pages 578–583, 2012.
- [42] Guangsheng Zhang, Lei Cao, Shanhai Ge, Chao-Yang Wang, Christian E. Shaffer, and Christopher D. Rahn. In Situ Measurement of Radial Temperature Distributions in Cylindrical Li-Ion Cells. *Journal of The Electrochemical Society*, 161:A1499–A1507, 2014.
- [43] S. J. Drake, D. A. Wetz, J. K. Ostanek, S. P. Miller, J. M. Heinzl, and A. Jain. Measurement of anisotropic thermophysical properties of cylindrical Li-ion cells. *Journal of Power Sources*, 252:298–304, 2014.
- [44] Andrew Mills and Said Al-Hallaj. Simulation of passive thermal management system for lithium-ion battery packs. *Journal of Power Sources*, 141:307–315, 2005.
- [45] Karthik Somasundaram, Erik Birgersson, and Arun Sadashiv Mujumdar. Thermal-electrochemical model for passive thermal management of a spiral-wound lithium-ion battery. *Journal of Power Sources*, 203:84–96, 2012.
- [46] K. Shah, S. J. Drake, D. A. Wetz, J. K. Ostanek, S. P. Miller, J. M. Heinzl, and A. Jain. Modeling of steady-state convective cooling of cylindrical Li-ion cells. *Journal of Power Sources*, 258:374–381, 2014.
- [47] Rui Zhao, Sijie Zhang, Jie Liu, and Junjie Gu. A review of thermal performance improving methods of lithium ion battery: Electrode modification and thermal management system. *Journal of Power Sources*, 299:557–577, 2015.
- [48] Dafen Chen, Jiuchun Jiang, Gi-Heon Kim, Chuanbo Yang, and Ahmad Pesaran. Comparison of different cooling methods for lithium ion battery cells. *Applied Thermal Engineering*, 94:846–854, 2016.

- [49] F. Torabi and V. Esfahanian. Study of Thermal-Runaway in Batteries I. Theoretical Study and Formulation. *Journal of The Electrochemical Society*, 158:A850–A858, 2011.
- [50] Donal P. Finegan, Mario Scheel, James B. Robinson, Bernhard Tjaden, Ian Hunt, Thomas J. Mason, Jason Millichamp, Marco Di Michiel, Gregory J. Offer, Gareth Hinds, Dan J. L. Brett, and Paul R. Shearing. In-operando high-speed tomography of lithium-ion batteries during thermal runaway. *Nature Communications*, 6:6924, 2015.
- [51] Johnsee Lee, K. W. Choi, N. P. Yao, and C. C. Christianson. Three-Dimensional Thermal Modeling of Electric Vehicle Batteries. *Journal of The Electrochemical Society*, 133:1286–1291, 1986.
- [52] Yufei Chen and James W. Evans. Three-Dimensional Thermal Modeling of Lithium-Polymer Batteries under Galvanostatic Discharge and Dynamic Power Profile. *Journal of The Electrochemical Society*, 141:2947–2955, 1994.
- [53] Carolyn R. Pals and John Newman. Thermal Modeling of the Lithium/Polymer Battery I . Discharge Behavior of a Single Cell. *Journal of The Electrochemical Society*, 142:3274–3281, 1995.
- [54] Carolyn R. Pals and John Newman. Thermal Modeling of the Lithium/Polymer Battery II . Temperature Profiles in a Cell Stack. *Journal of The Electrochemical Society*, 142:3282–3288, 1995.
- [55] T. D. Hatchard, D. D. MacNeil, A. Basu, and J. R. Dahn. Thermal Model of Cylindrical and Prismatic Lithium-Ion Cells. *Journal of The Electrochemical Society*, 148:A755–A761, 2001.
- [56] Guifang Guo, Bo Long, Bo Cheng, Shiqiong Zhou, Peng Xu, and Binggang Cao. Three-dimensional thermal finite element modeling of lithium-ion battery in thermal abuse application. *Journal of Power Sources*, 195:2393–2398, 2010.



- [57] M. Sievers, U. Sievers, and S. S. Mao. Thermal modelling of new Li-ion cell design modifications. *Forschung im Ingenieurwesen*, 74:215–231, 2010.
- [58] Rachel E. Gerver and Jeremy P. Meyers. Three-Dimensional Modeling of Electrochemical Performance and Heat Generation of Lithium-Ion Batteries in Tabbed Planar Configurations. *Journal of The Electrochemical Society*, 158:A835–A843, 2011.
- [59] Dong Hyup Jeon and Seung Man Baek. Thermal modeling of cylindrical lithium ion battery during discharge cycle. *Energy Conversion and Management*, 52:2973–2981, 2011.
- [60] Meng Guo and Ralph E. White. Thermal Model for Lithium Ion Battery Pack with Mixed Parallel and Series Configuration. *Journal of The Electrochemical Society*, 158:A1166–A1176, 2011.
- [61] Jaeshin Yi, Boram Koo, and Chee Burm Shin. Three-Dimensional Modeling of the Thermal Behavior of a Lithium-Ion Battery Module for Hybrid Electric Vehicle Applications. *Energies*, 7:7586–7601, 2014.
- [62] K. Shah, S. J. Drake, D. A. Wetz, J. K. Ostanek, S. P. Miller, J. M. Heinzl, and A. Jain. An experimentally validated transient thermal model for cylindrical Li-ion cells. *Journal of Power Sources*, 271:262–268, 2014.
- [63] Ying Shi, K. Smith, E. Wood, and A. Pesaran. A multi-node thermal system model for lithium-ion battery packs. In *2015 American Control Conference (ACC)*, pages 723–727, 2015.
- [64] Chao Zhang, Shriram Santhanagopalan, Michael A. Sprague, and Ahmad A. Pesaran. Coupled mechanical-electrical-thermal modeling for short-circuit prediction in a lithium-ion cell under mechanical abuse. *Journal of Power Sources*, 290:102–113, 2015.

- [65] Chao Zhang, Shriram Santhanagopalan, Michael A. Sprague, and Ahmad A. Pesaran. A representative-sandwich model for simultaneously coupled mechanical-electrical-thermal simulation of a lithium-ion cell under quasi-static indentation tests. *Journal of Power Sources*, 298:309–321, 2015.
- [66] Xuning Feng, Caihao Weng, Minggao Ouyang, and Jing Sun. Online internal short circuit detection for a large format lithium ion battery. *Applied Energy*, 161:168–180, 2016.
- [67] Weifeng Fang, Premanand Ramadass, and Zhengming (John) Zhang. Study of internal short in a Li-ion cell-II. Numerical investigation using a 3d electrochemical-thermal model. *Journal of Power Sources*, 248:1090–1098, 2014.
- [68] W. B. Gu and C. Y. Wang. Thermal-Electrochemical Modeling of Battery Systems. *Journal of The Electrochemical Society*, 147:2910–2922, 2000.
- [69] Gi-Heon Kim, Kandler Smith, Kyu-Jin Lee, Shriram Santhanagopalan, and Ahmad Pesaran. Multi-Domain Modeling of Lithium-Ion Batteries Encompassing Multi-Physics in Varied Length Scales. *Journal of The Electrochemical Society*, 158:A955–A969, 2011.
- [70] Weifeng Fang, Ou Jung Kwon, and Chao-Yang Wang. Electrochemical-thermal modeling of automotive Li-ion batteries and experimental validation using a three-electrode cell. *International Journal of Energy Research*, 34:107–115, 2010.
- [71] Songrui Wang, Lili Lu, and Xingjiang Liu. A simulation on safety of LiFePO<sub>4</sub>/C cell using electrochemical-thermal coupling model. *Journal of Power Sources*, 244:101–108, 2013.
- [72] Yonghuang Ye, Yixiang Shi, Lip Huat Saw, and Andrew A. O. Tay. An electro-thermal model and its application on a spiral-wound lithium ion battery with porous current collectors. *Electrochimica Acta*, 121:143–153, 2014.

- [73] L. H. Saw, Yonghuang Ye, and A. A. O. Tay. Electrochemical-thermal analysis of 18650 Lithium Iron Phosphate cell. *Energy Conversion and Management*, 75:162–174, 2013.
- [74] Mehdi Gilaki, Alex Francis, Daniel Bautista, and Ilya Avdeev. Progress Toward Understanding Catastrophic Failure of Electric Vehicle Li-Ion Batteries: Multi-Physics Modeling. page V014T07A009, November 2016.
- [75] E. P. Roth, D. H. Doughty, and D. L. Pile. Effects of separator breakdown on abuse response of 18650 li-ion cells. *Journal of Power Sources*, 174(2):579–583, 2007.
- [76] John Cannarella, Xinyi Liu, Collen Z. Leng, Patrick D. Sinko, Gennady Y. Gor, and Craig B. Arnold. Mechanical Properties of a Battery Separator under Compression and Tension. *Journal of The Electrochemical Society*, 161(11):F3117–F3122, 2014.
- [77] Gennady Y. Gor, John Cannarella, Jean H. Prvost, and Craig B. Arnold. A Model for the Behavior of Battery Separators in Compression at Different Strain/Charge Rates. *Journal of The Electrochemical Society*, 161(11):F3065–F3071, 2014.
- [78] Xiaowei Zhang, Elham Sahraei, and Kai Wang. Li-ion Battery Separators, Mechanical Integrity and Failure Mechanisms Leading to Soft and Hard Internal Shorts. *Scientific Reports*, 6:32578, 2016.
- [79] Xiaowei Zhang, Elham Sahraei, and Kai Wang. Deformation and failure characteristics of four types of lithium-ion battery separators. *Journal of Power Sources*, 327:693–701, 2016.
- [80] Sergiy Kalnaus, Yanli Wang, and John A. Turner. Mechanical behavior and failure mechanisms of Li-ion battery separators. *Journal of Power Sources*, 348:255–263, 2017.
- [81] Chao Zhang, Jun Xu, Lei Cao, Zenan Wu, and Shriram Santhanagopalan. Constitu-

- tive behavior and progressive mechanical failure of electrodes in lithium-ion batteries. *Journal of Power Sources*, 357:126–137, 2017.
- [82] Lars Greve and Clemens Fehrenbach. Mechanical testing and macro-mechanical finite element simulation of the deformation, fracture, and short circuit initiation of cylindrical lithium ion battery cells. *Journal of Power Sources*, 214:377–385, 2012.
- [83] Elham Sahraei, Rich Hill, and Tomasz Wierzbicki. Calibration and finite element simulation of pouch lithium-ion batteries for mechanical integrity. *Journal of Power Sources*, 201:307–321, 2012.
- [84] Richard Lee Hill. Development of a representative volume element of lithium-ion batteries for thermo-mechanical integrity. M.sc. thesis, Massachusetts Institute of Technology, 2011. Thesis (Nav. E. and S.M.)—Massachusetts Institute of Technology, Dept. of Mechanical Engineering, 2011.
- [85] Elham Sahraei, John Campbell, and Tomasz Wierzbicki. Modeling and short circuit detection of 18650 li-ion cells under mechanical abuse conditions. *Journal of Power Sources*, 220:360–372, 2012.
- [86] Ilya V. Avdeev and Mehdi Gilaki. Explicit dynamic simulation of impact in cylindrical lithium-ion batteries. pages 461–467, Houston, Texas, USA, 2012.
- [87] Tomasz Wierzbicki and Elham Sahraei. Homogenized mechanical properties for the jellyroll of cylindrical lithium-ion cells. *Journal of Power Sources*, 241:467–476, 2013.
- [88] WenWei Wang, Sheng Yang, and Cheng Lin. Clay-like mechanical properties for the jellyroll of cylindrical Lithium-ion cells. *Applied Energy*, 196:249–258, 2017.
- [89] Mehdi Gilaki and Ilya Avdeev. Comparing High-Performance Computing Techniques for Modeling Structural Impact on Battery Cells. page V06AT07A035, 2014.

- [90] Madhukar Chatiri, Thomas Gull, and Anton Matzenmiller. An assessment of the new LS-DYNA layered solid element: Basics, patch simulation and its potential for thick composite structure analysis. 2009.
- [91] S. Kim, Y. S. Lee, H. S. Lee, and H. L. Jin. A study on the behavior of a cylindrical type li-ion secondary battery under abnormal conditions. ber das verhalten eines zylindrischen li-ionen akkumulators unter abnormalen bedingungen. *Mat.-wiss. u. Werkstofftech.*, 41(5):378–385, 2010.
- [92] Juner Zhu, Xiaowei Zhang, Elham Sahraei, and Tomasz Wierzbicki. Deformation and failure mechanisms of 18650 battery cells under axial compression. *Journal of Power Sources*, 336:332–340, 2016.
- [93] James Marcicki, Min Zhu, Alexander Bartlett, Xiao Guang Yang, Yijung Chen, Theodore Miller, Pierre L’Eplattenier, and Iaki Caldichoury. A Simulation Framework for Battery Cell Impact Safety Modeling Using LS-DYNA. *Journal of The Electrochemical Society*, 164:A6440–A6448, 2017.
- [94] James Michael Hooper and James Marco. Experimental modal analysis of lithium-ion pouch cells. *Journal of Power Sources*, 285:247–259, 2015.
- [95] James Michael Hooper, James Marco, Gael Henri Chouchelamane, Christopher Lyness, and James Taylor. Vibration Durability Testing of Nickel Cobalt Aluminum Oxide (NCA) Lithium-Ion 18650 Battery Cells. *Energies*, 9:281, 2016.
- [96] Limhi Somerville, James Michael Hooper, James Marco, Andrew McGordon, Chris Lyness, Marc Walker, and Paul Jennings. Impact of Vibration on the Surface Film of Lithium-Ion Cells. *Energies*, 10:741, 2017.
- [97] Hailing Luo, Yong Xia, and Qing Zhou. Mechanical damage in a lithium-ion pouch cell under indentation loads. *Journal of Power Sources*, 357:61–70, 2017.

- [98] Thomas Kisters, Elham Sahraei, and Tomasz Wierzbicki. Dynamic impact tests on lithium-ion cells. *International Journal of Impact Engineering*, 2017.
- [99] W. Tsutsui, T. Siegmund, N. D. Parab, H. Liao, T. N. Nguyen, and W. Chen. State-of-Charge and Deformation-Rate Dependent Mechanical Behavior of Electrochemical Cells. *Experimental Mechanics*, pages 1–6, 2017.
- [100] Yong Xia, Tomasz Wierzbicki, Elham Sahraei, and Xiaowei Zhang. Damage of cells and battery packs due to ground impact. *Journal of Power Sources*, 267:78–97, 2014.
- [101] D. H. Doughty and E. P. Roth. A general discussion of li ion battery safety. *The Electrochemical Society Interface*, pages 37–44, 2012.
- [102] Samuel C. Levy. Safety and reliability considerations for lithium batteries. *Journal of Power Sources*, 68(1):75–77, 1997.
- [103] O. Manuel and R. H. Maurer. Fault tree safety analysis of a large li/SOCl<sub>2</sub> spacecraft battery. *Journal of Power Sources*, 21(3-4):207–225, 1987.
- [104] D. Fouchard and L. Lechner. Analysis of safety and reliability in secondary lithium batteries. *Electrochimica Acta*, 38(9):1193–1198, 1993.
- [105] Seung-Wook Eom, Min-Kyu Kim, Ick-Jun Kim, Seong-In Moon, Yang-Kook Sun, and Hyun-Soo Kim. Life prediction and reliability assessment of lithium secondary batteries. *Journal of Power Sources*, 174(2):954–958, 2007.
- [106] Ping Liu, Elena Sherman, and Alan Jacobsen. Design and fabrication of multifunctional structural batteries. *Journal of Power Sources*, 189(1):646–650, 2009.
- [107] Displacement verification. <http://www.instron.us/en-us/service-and-support/services/calibration-and-verification/learn-more/displacement-verification>. (accessed May 24, 2017).

- [108] Lvdtd deflection sensor, range +/- 15 mm. <http://www.instron.us/en-us/products/testing-accessories/extensometers/deflectometers/deflectometers/2601-043>. (accessed May 24, 2017).
- [109] *UL 1642*. UL Standard for Safety for Lithium Batteries, 4th edition edition, 2007.
- [110] *UN DOT 38.3*. UN Manual of Tests and Criteria, Lithium Battery Testing Requirements, 4th edition edition.
- [111] *LS-DYNA Keyword User's Manual*, volume 1. Livermore Software Technology Corporation, r7.1 edition, 2014.
- [112] J. O. Hallquist. *LS-DYNA Theory Manual*, volume 1. Livermore Software Technology Corporation, r7.1 edition, 2006.



# Mehdi Gilaki | Curriculum Vitae

## Education

---

### University of Wisconsin-Milwaukee

*Ph.D - Mechanical Engineering*  
(GPA 3.96)

**Milwaukee - USA**

2011–2017

### K.N.T. University of Technology

*M.Sc - Mechanical Engineering*  
(GPA 17/20)

**Tehran - Iran**

2006–2009

### Iran University of Science & Technology

*B.Sc - Mechanical Engineering*

**Tehran - Iran**

2000–2005

## Experience

---

### Finite Element Specialist

*Advanced Manufacturing & Design Lab.*

**Project:** Crash safety of Lithium-ion batteries sponsored by **Johnson Controls Inc.**

**UW-Milwaukee**

2012–2017

### Instructor

*Mechanical Engineering Department*

**UW-Milwaukee**

2012–2017

- ME-463 Introduction to Finite Elements. (**340** Students – Evaluation **4.39/5**)
- ME-366 Design of Machine Elements. (**53** Students – Evaluation **3.63/5**)
- ME-479 Control and Design of Mechatronic Systems. (**37** Students – Evaluation **4.64/5**)

### Graduate Research Assistant

*Tribology & Energy Diagnostics Lab.*

**Tehran-Iran**

2011 – 2012

### Pneumatics Engineer

*Erafeat Sanaat Qeshm*

**Tehran-Iran**

2008 – 2010

### Finite Element Specialist

*Iran University of Science & Technology*

**Tehran-Iran**

2005 – 2010

## Skills

---

**Finite element analysis:** LS-DYNA, ANSYS APDL, Multi-Physics Simulation, CFD, Parallel computing.

**Programming:** MATLAB, C++, UNIX shell scripting, APDL.

**CAD:** SolidWorks, CATIA V5.

**Office:** Microsoft Word, Excel, Powerpoint,  $\text{\LaTeX}$ .

**Other:** Reliability and failure mode and effects analysis (FMEA).

## Publications

---

### Journal Articles.....

[J2]: **Mehdi Gilaki**, Ilya Avdeev, *"Impact modeling of cylindrical lithium-ion battery cells: a heterogeneous approach"*, Journal of Power Sources, 328 (2016) 443-451.

[J1]: Ilya Avdeev, **Mehdi Gilaki**, *"Structural analysis and experimental characterization of cylindrical lithium-ion battery cells subject to lateral impact"*, Journal of Power Sources, 271 (2014) 382-391.

### Conference Presentations.....

[C7]: **Mehdi Gilaki**, Alex Francis, Daniel Bautista, Ilya Avdeev, *"Progress toward understanding catastrophic failure of electric vehicle Li-ion batteries: multi-physics modeling"*, ASME/IMECE (2016), Phoenix, Arizona.

[C6]: **Mehdi Gilaki**, Ilya Avdeev, *"Comparing High-Performance Computing Techniques for Modeling Structural Impact on Battery Cells"*, ASME/IMECE (2014), Montreal, Canada.

[C5]: **Mehdi Gilaki**, Ilya Avdeev, *"Structural Homogenization in Energy Storage Systems"*, 11<sup>th</sup> World Congress on Computational Mechanics, (2014), Barcelona, Spain.

[C4]: Ilya Avdeev, **Mehdi Gilaki**, *"Modeling Longitudinal and Transverse Impact in Cylindrical Battery Cells"*, ASME/IMECE (2013), San Diego, California.

[C3]: Ilya Avdeev, **Mehdi Gilaki**, *"Homogenization of Structural Material Properties in Cylindrical Lithium-Ion Battery Cells,"*, USNCCM12, (2013), Raleigh, North Carolina.

[C2]: Ilya Avdeev, **Mehdi Gilaki**, *"Explicit Dynamic Simulation of Impact in Cylindrical Lithium-Ion Cells,"*, ASME/IMECE (2012), Houston, Texas.

[C1]: **Mehdi Gilaki**, Emmanuel Worniyoh *"A Review of Friction-Induced Thermo-mechanical Instability,"*, ASME/IJTC (2011), Los Angeles, California.

## Projects

---

### Design, Finite Element Modeling and Programming.....

#### **Design for safety and impact simulation of lithium-ion battery packs:**

- Sponsored by **Johnson Controls Inc.**
- Explicit impact simulations and various types of experiments.
- Utilized LS-DYNA to perform multi-physics and multi-scale simulations.
- Utilized ANSYS, SolidWorks and MATLAB.
- Utilized high-performance computing techniques.
- Developed UNIX shell scripts for automatic parsing of LS-DYNA results.

#### **Study of wrinkling in foam-cored sandwich beams:**

- Finite element modeling and experimental validations.
- Utilized ANSYS, APDL and MATLAB.

#### **Various Macros and Subroutines for automating FE simulations:**

- Macro for auto-exporting models from ANSYS to LS-DYNA.
- Macro for mass estimation of composite parts in ANSYS.

### Experiments.....

#### **Impact test on cylindrical lithium-ion battery cells:**

- Various tests were conducted in a custom-design drop-test apparatus.
- Cells were CT-scanned to study the effects of high impact loads.

#### **Material characterization of lithium-ion cell's jellyroll:**

- Compression tests on dry and wet jellyroll samples and its individual layers .
- Utilized Instron and TestResources universal machines.

#### **Buckling and wrinkling tests on foam-cored sandwich beams:**

- Used Instron testing machine to perform compressive tests on composite beams.
- Sandwich beams with PVC cores and fiberglass face sheets were tested.
- Effects of various parameters on beam buckling and face sheet wrinkling were studied .

#### **Study of wheel wear in Tehran-Mashad railway in Iran:**

- Field measurements to study wheel wear parameters.
- Utilized Miniprof tool to measure wheel profile after every few train trips.

## Extracurricular Experience

---

**2015-2017:** President of "Persian Culture Association" at UWM.

## Research Interests

---

- **Crashworthiness Simulations**
- **Finite Element Analysis**
- **Lithium-ion Batteries**
- **Computational Mechanics**
- **Multi-physics Modeling**

## Trainings/Certificates

---

**2017: Johnson Controls Tech. Challenge**

Johnson Controls Inc.

**2014: Introduction to Parallel programming**

UW-Milwaukee

**2008: Pneumatics workshop**

Metalwork Pneumatic, Brescia, Italy.

## Awards

---

**2016:** UWM College of Engineering & Applied Science Dean's Scholarship.

**2011-2014:** UWM Chancellor's Graduate Student Award.